Resonance Raman Spectroscopy of Redox-Active Metal Clusters in Proteins and Model Compounds

Jonathan D. Cohen
B.A., University of California at Santa Barbara, 1989

A dissertation submitted to the faculty of the
Oregon Graduate Institute of Science and Technology
in partial fulfillment of the
requirements for the degree
Doctor of Philosophy
in
Chemistry

February, 1997

The dissertation "Resonance Raman Spectroscopy of Redox-Active Metal Clusters as Models for Metalloproteins" by Jonathan D. Cohen has been examined and approved by the following Examination Committee:

Thomas M. Loehr
Professor and Dissertation Advisor

Joann Sanders-Loehr
Professor and Dissertation Advisor

Ninian J. Blackburn
Professor and Department Head

James K. Hurst
Professor and External Examiner
Washington State University, Pullman, WA

Acknowledgments

First and foremost, I want to express my deepest thanks to Profs. Thomas Loehr and Joann-Sanders Loehr for taking a chance on an unknown chemist and giving me the opportunity to study under their expert tutelage. I also wish to thank my other Ph.D. committee members, Profs. Ninian Blackburn and Jim Hurst, who have served as expert teachers both in the classroom and in research seminars, and for taking the time to carefully review my dissertation. I am also grateful to Prof. V. Renganathan, Dr. Wenjun Bao, and Sai Subramaniam for their purification of the cellobiose dehydrogenase samples; Prof. Mike Fryzuk and Dr. Murugesapillai Mylvaganam for providing the zirconium dinitrogen compounds; Prof. Karl Hagen and Sonha Payne for providing the mixed-valence diiron compounds; and Prof. Liz Theil, Dana Danger, and Dr. John Fetter for providing the ferritin samples. I also want to express my thanks to Dr. Jie Sun for the countless discussions and insights he provided. I also wish to thank, in no particular order, Prof. Mike Khalow, Prof. Shankar Rananavare, Mary Vatne, Dr. Kevin Maloney, Ciro DiMeglio, Dr. Pierre Möenne-Loccoz, Dr. Nobumasa Nakamura, Julie Wilson, and Steve Dodge for helping me in ways they may not even know. Finally I wish to dedicate this thesis to Laura Cohen, my wife and best friend for tolerating my thoughtless, irrational and sometimes juvenile delinquent behavior during my Ph.D. studies; my parents for providing me with love, a home, and an education; and to the Flat Earth Society in the hopes that they may one day learn that two half-truths do not make a whole truth.

Table of Contents

List of Tables

List of Figures

Abstract

Resonance Raman Spectroscopy of Redox Active Metal Clusters in Proteins and Model Compounds

Jonathan D. Cohen

Oregon Graduate Institute of Science and Technology
Supervising Professors: Thomas M. Loehr and Joann Sanders-Loehr

Four different redox-active metal clusters with unusual properties were studied by resonance Raman (RR) spectroscopy.

Two dizirconium compounds, $\{[(Pr^{i}_2PCH_2SiMe_2)_2N]Zr(\eta^5\text{-}C_5H_5)\}_2(\mu\text{-}\eta^1\text{:}\eta^1\text{-}N_2)$ and $\{[(Pr^{i}_2PCH_2SiMe_2)_2N]ZrCl\}_2(\mu\text{-}\eta^2\text{:}\eta^2\text{-}N_2)$ serve as spectroscopic models for nitrogen activation. Resonance Raman spectra of these compounds reveal ν(N-N) modes at 1211 and 731 cm^{-1}, respectively. These frequencies imply N-N bond orders of ~1 and less than 1, respectively. The high degree of N_2 activation in these compounds suggests that N_2 activation by nitrogenase is possible with N_2 bound with either "end-on" or "side-on" geometry to two or more metal atoms.

Resonance Raman spectra of $[Fe_2O(Ph_3CCOO)_2(Me_3tacn)_2]X$ (X = $CF_3SO_3^-$ or BPh_4^-) show that the intensity of ν_{as}(Fe-O-Fe) at ~702 cm^{-1} is unusually high. This is ascribed to structural asymmetry, thereby providing evidence for a trapped-valence (Fe^{2+}/Fe^{3+}) species. Retention of the μ-^{18}O ligand during the oxidation of $[Fe_2(^{18}OH)(Ph_3CCOO)_2(Me_3tacn)_2]X$ by O_2, H_2O_2, or R_3NO, proves that electron transfer

proceeds via an outer-sphere mechanism. This is in contrast to the inner-sphere mechanism proposed for ribonucleotide reductase and $Fe_2(O_2CH)_4(BIPhMe)_2$.

Cellobiose dehydrogenase from *Phanerochaete chrysosporium* contains a flavin adenine dinucleotide and a *b*-type heme on separate domains of the monomeric protein. Raman excitation of the oxidized holoprotein at 413.1 nm results in photoreduction of the heme, displaying ν_4 at ~1362 cm^{-1}. However, excitation of deflavoCDH or the isolated heme domain under identical conditions did not cause photoreduction. These observations suggest that electron transfer proceeds from the flavin to the heme, as in flavocytochrome b_2 from *Saccharomyces cerevisiae*.

A transient iron-tyrosinate intermediate forms upon addition of Fe^{2+} and O_2 to wild type and mutant frog H-chain apoferritin. The half-life of decay of this intermediate recorded by electronic or RR spectroscopy is very similar, indicating that the two analytes are the same. Studies on H-, M- and L-chain mutants imply that a specific tyrosine (probably Tyr136 or Tyr147) is responsible for color formation in frog FTN-H but a different residue (probably Tyr30) is responsible for rapid ferroxidation in human FTN-H and frog FTN-M. Ferroxidase activity could be due to a stable diiron cluster that catalyzes electron transfer or to a mobile cluster that is autocatalytic.

Chapter 1

Redox-Active Clusters in Proteins and Model Compounds

Multinuclear Metal Clusters in Enzymes. Many of the most important biochemical reactions, including respiration[1,2] and photosynthesis,[3,4] would not be possible without the participation of metal atoms in proteins and enzymes. Transition metals are especially useful because they are stable in more than one oxidation state, allowing reversible redox reactions to occur under favorable thermodynamic conditions.[5] Some metal cofactors contain a single metal ion bound to a set of ligands donated by the protein or an organic cofactor such as a porphyrin. These sites will be referred to as simple metal sites because they contain only a single metal atom with at most a single organic cofactor. Although transition metal-containing cofactors are the product of complex biosynthetic mechanisms,[6-9] transition metal atoms are small, self-contained redox centers present in the environment ready to use. While there can be no argument that simple metal sites within proteins and enzymes are ubiquitous biochemical features, multinuclear metal clusters, and simple metal sites acting in concert with additional cofactors, are also commonplace in enzymology.

There are important features that distinguish multinuclear metal clusters from simple metal sites. Simple metal clusters often show considerable metal-ligand bond changes after oxidation or reduction, such as in bacterial [1Fe-4S] clusters where the redox change from the ferrous to the ferric state results in a 2-3% change in Fe-S bond distances.[10] However, multinuclear metal clusters as redox sites divide the ligand reorganization energy over the entire cluster resulting in smaller individual changes in metal-ligand bond lengths, such as in bacterial [4Fe-4S] clusters where oxidation of the cluster results in only an ~1.3 % change in Fe-S bond lengths for each metal atom in the

cluster.[10] Multinuclear clusters also provide more metal-substrate bonds, often by increasing the degree of hapticity by inducing μ-η^1:η^1, μ-η^2:η^2 or higher hapticity. Furthermore, multinuclear metal clusters involved in catalysis increase the potential supply of electrons available for redox reactions by performing redox reactions at more than one metal atom. Consequently, the qualities that promote catalysis in simple metal clusters are often enhanced in multinuclear clusters.

In addition, simple metal sites acting in concert with additional organic cofactors allow substrate reduction and sequential electron transfer to occur on a monomeric protein, where one cofactor acts as the substrate binding site while other cofactors function as intraprotein redox sites. For example, the flavocytochrome b_2 of *Saccharomyces cerevisiae* uses a flavin mononucleotide cofactor to oxidize lactate to pyruvate, transferring electrons one at a time to the heme cofactor on a separate domain of the protein.[11] These non-metal-containing cofactors allow electrons to be shuttled in and out of the active site in carefully regulated steps just as capacitors are used in electronic devices to accumulate charge for later release. Two or more multinuclear clusters can also be used as separate substrate binding sites and redox sites, such as the P-clusters and the FeMo cofactor of nitrogenase, where the first cofactor serves as an electron transfer nexus and the second cofactor is believed to be the site of substrate reduction.[12] Redox reactions at non-substrate-binding cofactors are often accompanied by ATP hydrolysis, changes in protonation, or small but necessary changes in the conformation of the protein.[13-16]

Efforts to explain why some enzymes use multinuclear clusters while others use simple metal sites or no metals at all remains a significant challenge of biochemistry. To complicate matters, an enzyme that catalyzes the same reaction in different organisms may use very different metal clusters, such as the four classes of ribonucleotide reductase that each use different metal cofactors.[17] Furthermore, an enzyme designed to perform a particular task in simple organisms may have its abilities altered due to evolutionary pressure, such as when two genes coding for separate products fuse to form a bifunctional protein (e.g. flavocytochrome b_2).[18] Occasionally, scientists even discover an enzyme whose holo- and apoprotein forms serve completely separate biochemical functions, such

as the aconitase/iron response protein (IRP) that serves entirely different biochemical functions in response to intracellular iron levels.[19] The selection of metals by enzymes may be related to the distribution of a given element (both in the surroundings and over evolutionary time), the physical properties of a particular metal (e.g. size, electron configuration, available oxidation states, etc.), the redox potential of the medium, and the presence of inhibitors. Consequently, rather than propose all-encompassing roles for a particular metal in biology, individual metalloenzymes are studied as unique biochemical entities containing specialized metal clusters to perform specific tasks that can evolve with their host organisms.

Characterization of metal clusters by spectroscopy. Although metalloenzymes have been studied for decades, it is only with the rise of modern spectroscopic methods that the structure and function of metal clusters have been documented in detail. Metal clusters possess unique qualities especially suited to studies by these techniques. For example, many metal atoms possess non-zero nuclear spin, which makes them amenable to study by magnetic resonance techniques such as NMR spectroscopy.[20] If the metalloenzyme also possesses unpaired electrons at or near the metal site, EPR spectroscopy can also be quite useful.[21] The electronic transitions of metal-containing chromophores make electronic absorption spectroscopy a simple yet powerful tool for identifying the metal-ligand coordination geometry and the presence of organic cofactors.[22] Information regarding the strength of metal-ligand bonds and the metal-ligand coordination geometry can also be deduced by vibrational methods such as infrared and resonance Raman spectroscopy.[23,24] If the protein or enzyme contains iron, Mössbauer spectroscopy can be used to determine the oxidation state and the presence of inequivalent iron atoms.[25] Finally, the high atomic mass of metal atoms make them amenable to X-ray absorption and EXAFS spectroscopy used for determining metal-ligand and metal-metal distances.[26] Each technique is based on the interaction between the metal cluster and electromagnetic radiation of a specific energy range to yield information regarding the physical and chemical properties of the cluster and its immediate surroundings, and many of these techniques can be applied to study both static and dynamic properties of enzymes.

Model compounds as learning tools. Advances in the field of inorganic and organometallic synthesis have produced model compounds that mimic the structure and sometimes the function of metal clusters in proteins. If the architecture of a metalloprotein has not been determined to high resolution by X-ray crystallography but its spectra are available, simplified models can be synthesized, their structures determined, and their spectra compared with those of the protein for similarities. As the models are modified, the most probable atomic structure of the metal site in the protein can be deduced. Although models do not always reproduce biological architecture with complete accuracy, they often give an excellent indication of the first coordination sphere of the metal atoms. If the overall goal is not just to mimic enzyme structure but to simulate activity, the essential structural elements of the metalloenzyme can be reproduced in a chemically active model and experimentally adjusted via ligand substitutions to determine how these changes affect the resulting chemistry. As an analytical tool, model compounds are used for examining structure-function relationships and for developing new strategies for catalysis.

In the next few pages, some instructive examples will be discussed that reveal how spectroscopy and model chemistry have been used to extract new insights and information regarding both the structure and reactivity of enzymes containing metal clusters. These examples will serve as brief introductions to the areas of research which will be covered in greater detail in the subsequent chapters.

Nitrogenase. Nitrogenase is a multiprotein system present in nitrogen fixing microorganisms that catalyzes the reduction of nitrogen to ammonia.[27] Although nitrogenase has been studied for over thirty years,[28] only in the last decade has real progress been made in solving the structure of the nitrogenase proteins and its cofactors. These discoveries have propelled the synthesis of new structural and functional model compounds that attempt to duplicate nitrogen reduction under mild conditions.

The nitrogenase system is composed of 2 proteins, the Fe-protein and the MoFe-protein, acting in concert to reduce one molecule of N_2 to two molecules of NH_3 and one molecule of H_2.[29] The overall reaction requires 8 electrons and at least 16 ATP molecules per turnover.[29] To navigate electrons through this complex process, each protein in the

nitrogenase system uses different metal clusters to perform inter- and intraprotein electron transfer.

Spectroscopy has been very useful for characterizing the metal clusters used by nitrogenase. EPR and Mössbauer spectroscopy were used to identify three types of iron-sulfur clusters in the *C. pasteurianum* nitrogenase system; the [4Fe-4S] cluster of the Fe-protein, and the P-clusters and iron-molybdenum cofactors (FeMoco) of the MoFe-protein.[30] Although the EPR spectra of the [4Fe-4S] cluster of the Fe-protein proved to be very similar to the spectra of other iron-sulfur proteins,[31] the cofactors of the MoFe-protein proved to be unique to nitrogenase. To further complicate matters, an alternative nitrogenase has been isolated from *A. vinelandii* that contains vanadium rather than molybdenum as well as a variant that contains neither V nor Mo, each of these variants displays slightly different kinetic and substrate specificities.[32,33]

The recently reported high-resolution crystal structures of nitrogenase from *C. pasteurianum* and *A. vinelandii* have proven invaluable in elucidating the atomic structure of the metal clusters in the Fe-protein and the MoFe-protein.[12,34-36] As deduced from spectroscopy, the Fe-protein was shown to contain a single [4Fe-4S] cluster at the interface to the two protein subunits. The MoFe-protein, on the other hand, contains one P-cluster on each of the two α subunits and one iron-molybdenum cofactor at each of the two α/β subunit interfaces. The P-clusters were shown to be composed of two [4Fe-4S] clusters bridged by two cysteine thiolates through opposite pairs of iron atoms and perhaps by an additional disulfide bond (Fig. 1-1). These cofactors receive electrons from the Fe-protein for transfer to the FeMo cofactors. The iron-molybdenum cofactors are more complex arrangements of iron sulfur clusters, with six 3-coordinate Fe atoms, one 4-coordinate Fe atom, nine acid-labile sulfides, one a molecule of homocitrate, and one 6-coordinate molybdenum atom (Fig. 1-2). Biochemical and mutagenesis studies have shown that the iron-molybdenum cofactors are the most probable sites of nitrogen activation.[37,38] Although the structure of FeMoco is known to high-resolution, the crystal structure of a substrate-bound form of the enzyme has not been reported and the isolated FeMoco is not catalytically active. Semi-empirical models have been used to propose several modes of substrate binding involving one or more metal atoms with terminal or

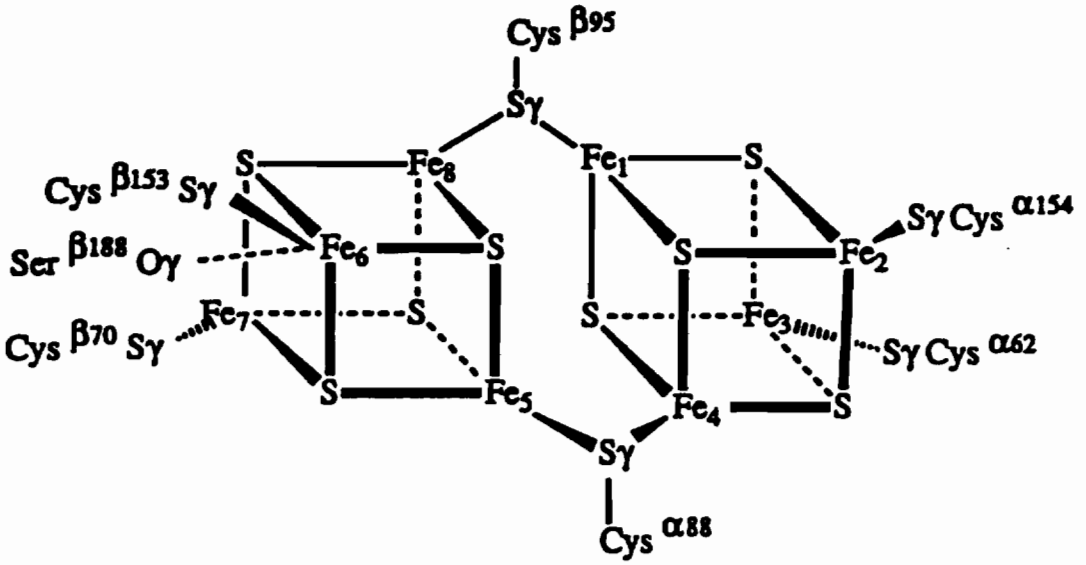

Figure 1-1. Schematic diagram of the P-cluster of the MoFe-protein of nitrogenase, adapted from reference 34.

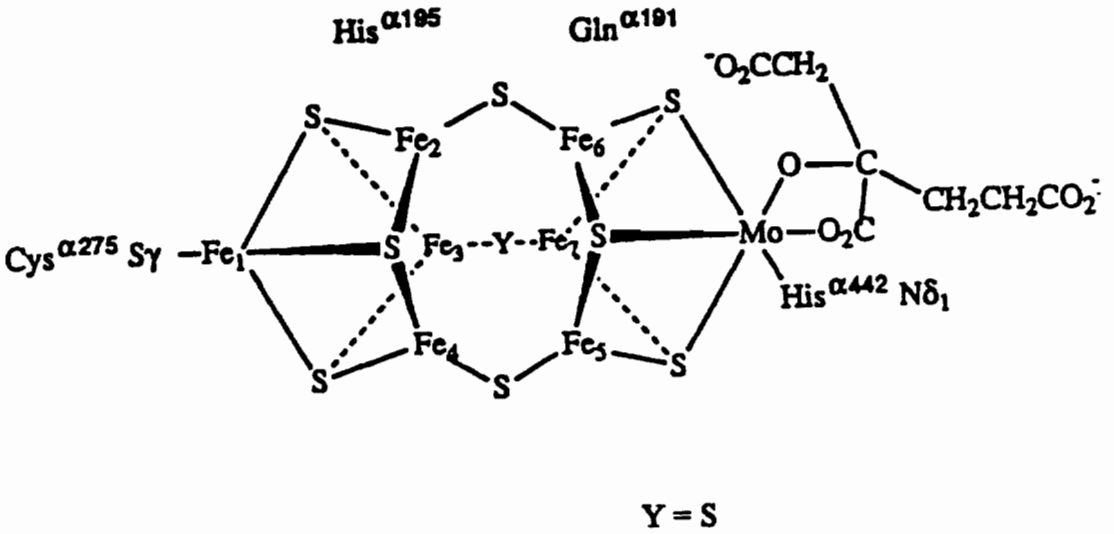

Figure 1-2. Schematic diagram of the FeMo cofactor of the MoFe-protein of nitrogenase, adapted from reference 34.

bridging N_2 ligands[39,40] and these theoretical constructs have served as starting points for model building studies.

Recently, the cleavage of N_2 by $Mo(NRAr)_3$ where R is $C(CD_3)_2CH_3$ and Ar is 3,5-$C_6H_3(CH_3)_2$ has been reported by Laplaza and coworkers.[41] The authors propose that two molybdenum clusters associate per equivalent of N_2 to catalyze N-N bond cleavage by forming a transient, purple intermediate. EXAFS and resonance Raman spectroscopy have shown that the purple intermediate contains a linear Mo-N-N-Mo bridging unit.[42] Even though the product of N_2 cleavage is $N{\equiv}Mo(NRAr)_3$ instead of ammonia, the facile cleavage of N_2 by these models suggests that a similar binding geometry (μ–η^1:η^1 or μ–η^2:η^2) could be used by nitrogenase for nitrogen activation. In nitrogenase, the metal sites most available for this type of bridging are the 3-coordinate iron atoms of FeMoco.

As described in chapter 2, resonance Raman spectroscopy was used to study N_2 ligands bound to two different dinuclear zirconium compounds.[43,44] One compound binds N_2 with μ–η^1:η^1 geometry similar to that observed for the Laplaza complex, the other with μ–η^2:η^2 geometry where the N_2 ligand is bound with its dinitrogen bond axis perpendicular to the dizirconium axis. Each complex demonstrated a decrease in the ν(N-N) stretching frequency from 2331 cm^{-1} for N_2(g) to 1211 and 731 cm^{-1}, respectively, concomitant with an increase in the N_2 bond length from 1.0975 Å for N_2(g) to 1.301 and 1.548 Å, respectively, implying a high degree of N-N bond activation in both complexes. Furthermore, the coordination geometry of the bound N_2 ligand had a significant and predictable effect on the number of fundamental, combination, and overtone bands observed in the RR spectrum. Thus, RR spectroscopy can be used to determine the ligand geometry and N-N bond order in model compounds with a dinuclear metal cluster and a bridging N_2 ligand.

Ribonucleotide Reductase. Ribonucleotide reductase (RibRed) reduces ribonucleotides to their corresponding 2′-deoxyribonucleotides for use in the biosynthesis of DNA.[45] Tremendous strides have been made in elucidating the mechanism of both mammalian and bacterial RibRed through the use of rapid freeze-quench spectroscopy. This technique is used to examine short-lived reaction intermediates by freezing them at low temperature. At the same time, new structural model compounds have come very

close to duplicating the spectroscopy of some key intermediates of RibRed and other enzymes.

Four different classes of RibRed have been isolated, each using a different type of metal cluster for catalysis.[17,45] The mammalian holoenzyme is composed of two pairs of equivalent subunits ($R1_2R2_2$). The X-ray crystal structure of the mammalian subunits expressed in *E. coli* have been solved to atomic resolution.[46,47] The two R1 subunits contain the catalytic and substrate binding sites. The R2 subunits, on the other hand, contain a diiron cluster that activates oxygen for the production of a tyrosyl radical (Tyr122·) required for catalysis (Fig. 1-3). The diiron cofactor of RibRed has received considerable attention because similar diiron cofactors are present in several other oxygen activating enzymes.[48,49]

Significant progress has been made in elucidating the mechanism of oxygen activation and concomitant tyrosyl radical formation by RibRed (Fig. 1-4).[50-54] Starting with fully-reduced enzyme, the R2 subunit binds O_2 at a di-μ-carboxylato diferrous site to form a putative diferric peroxo adduct (the existence of a peroxo adduct in RibRed is based on the observation of a peroxo adduct in the reaction cycle of methane monooxygenase, an evolutionarily related enzyme with a very similar diiron cluster that also activates oxygen).[55,56] Peroxo adduct formation is followed by O_2 bond cleavage to form a proposed bis-μ-oxo diferryl cluster. Subsequently, the diferryl intermediate is reduced by one electron to form a mixed-valence bis-μ-oxo or possibly hydroxo species denoted compound X, with an antiferromagnetically coupled $S = ½$ ground state. Compound X is competent to catalyze radical formation at Tyr122, which reduces the metal center to a μ-oxo diferric cluster.[57] Except for the crystal structures of the diferric and diferrous states of the enzyme, the structures of all the other intermediates are proposed on the basis of rapid freeze-quench spectroscopy and comparison to recently synthesized model compounds of known structure.[58] Nevertheless, the search for alternative structures that are consistent with the current data continues.

As described in chapter 3, RR and electronic absorption spectroscopy were used to study a novel synthetic diiron cluster isolated in a $S = ½$ mixed-valence state, similar to that proposed for compound X in RibRed and mixed-valence states in other diiron

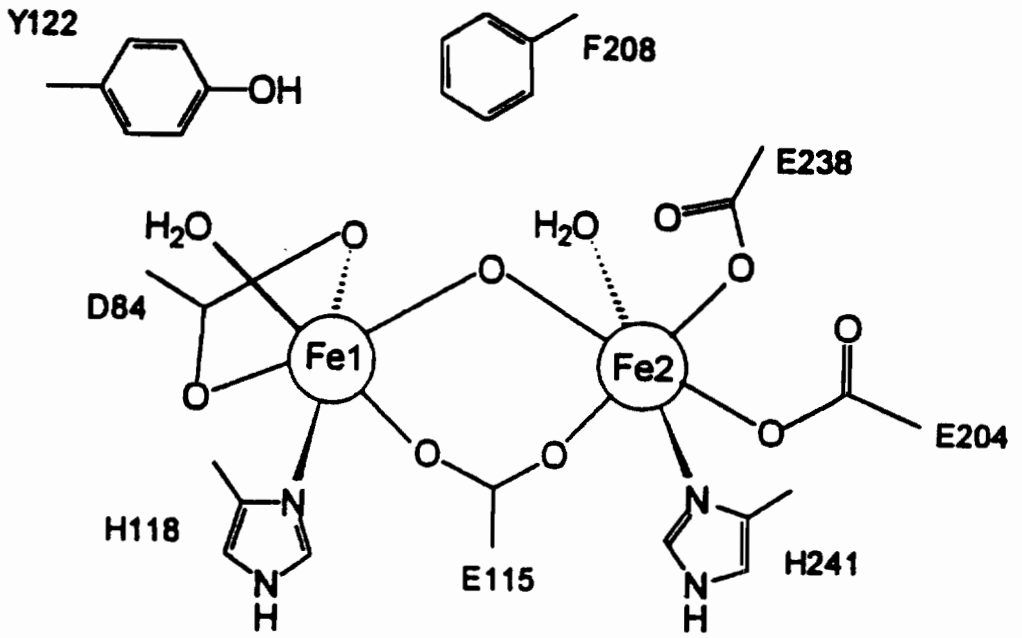

Figure 1-3. Schematic diagram of the diiron cofactor of mammalian ribonucleotide reductase, adapted from reference 57.

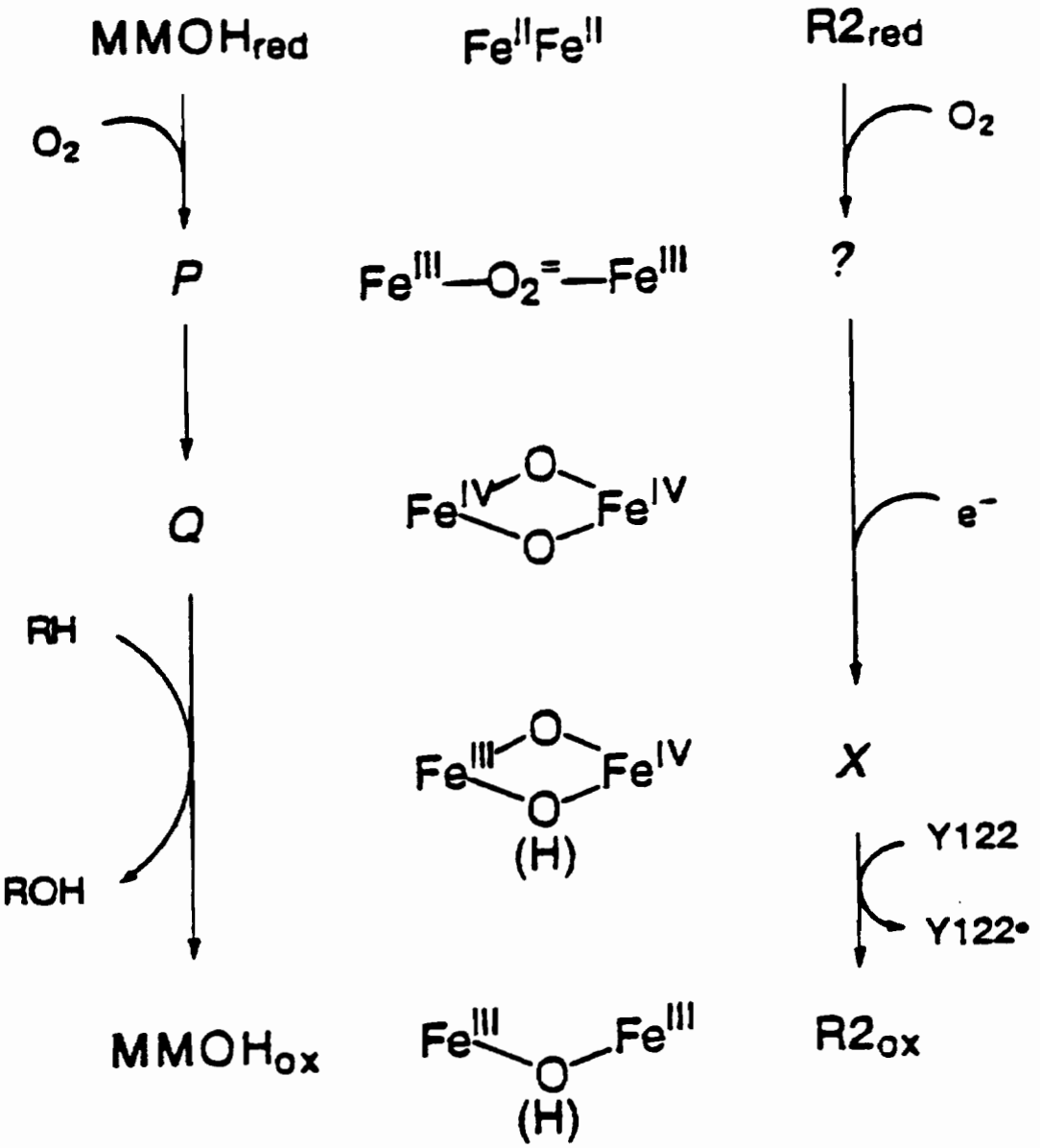

Figure 1-4. Proposed mechanism of activity for mammalian ribonucleotide reductase and methane monooxygenase, adapted from reference 75.

enzymes.[59-61] The X-ray crystal structure of this compound reveals two distinct Fe-oxo bond lengths that differ by 0.047 Å, suggesting that the extra electron is localized on one of the iron atoms. The RR spectrum of this compound revealed an intense asymmetric Fe-O-Fe stretching mode but no detectable symmetric stretching mode. These and other data are used to prove that this complex is stable in a trapped-valence Fe^{2+}/Fe^{3+} state. It is further shown that RR and electronic absorption spectroscopy can be used to measure the degree of asymmetry and delocalization in mixed-valence complexes.

Flavocytochrome b_2. Flavocytochrome b_2 (lactate:cytochrome *c* oxidoreductase) of *Saccharomyces cerevisiae* catalyzes the 2-electron oxidation of lactate to pyruvate while transferring electrons one at a time to cytochrome *c* for use in respiration.[62] Unlike the enzymes described previously, flavocytochrome b_2 (flavocyt b_2) uses only a single Fe atom bound to a *b*-type heme. However, the enzyme also possesses a molecule of flavin mononucleotide (FMN), a heterocyclic organic cofactor capable of 1- and 2-electron redox reactions. This enzyme provides an excellent example of how proteins can use a flavin cofactor to couple two-electron substrate oxidation to another metal site for one-electron transfer. This system can also be used as a starting point for the study of other hemoflavoenzymes that, although not evolutionarily related, use similar cofactors to catalyze similar reactions.

The two cofactors of flavocyt b_2 are on separate domains of the protein that can be cleaved proteolytically (Fig. 1-5).[11,63] It is possible that these two domains were once independent proteins whose genes were fused over the course of evolution, permanently coupling lactate oxidation with cytochrome *c* reduction. The crystal structure of flavocyt b_2 has been solved to low resolution.[62,64] However, many of the details regarding its structure and mechanism comes from comparison to other hemoproteins, flavoproteins, and isolated cofactors of known structure.[65]

In chapter 4 is described the first extensive RR analysis performed on cellobiose dehydrogenase (CDH) from *Phanaerochaete chrysosporium*. This enzyme is similar to flavocyt b_2, containing a *b*-type heme and in this case a flavin adenine dinucleotide (FAD) cofactor on different domains of a monomeric protein (Fig. 1-6). Samples of CDH were examined spectroscopically in both the reduced and oxidized states as the intact monomer

Figure 1-5. X-ray crystal structure of flavocytochrome b_2 showing the two domains and the heme and flavin cofactors, adapted from reference 62.

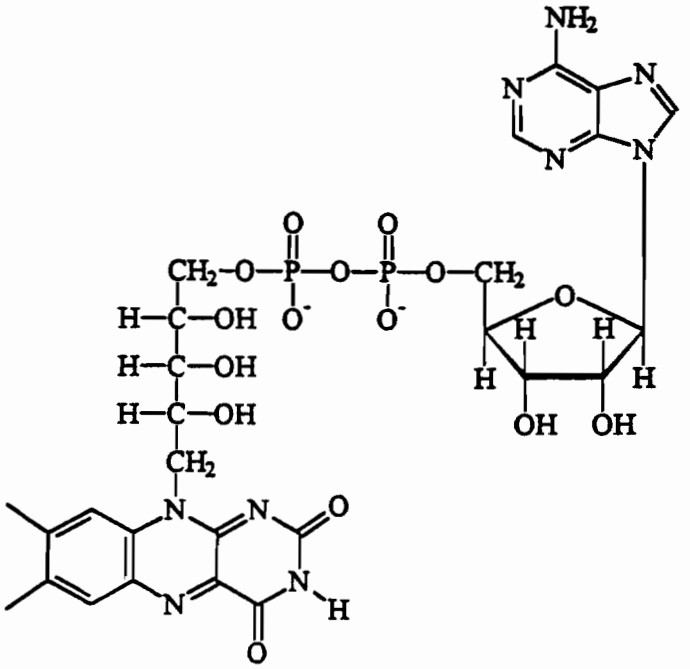

Oxidized Flavin Adenine Dinucleotide (FAD)

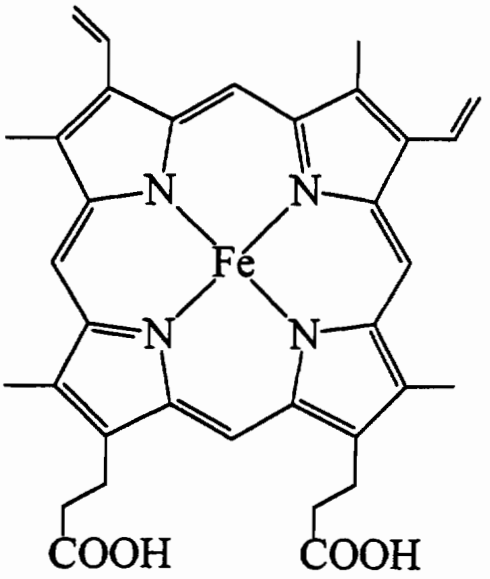

b-Type Heme (Protoporphyrin IX)

Figure 1-6. Schematic diagram of the *b*-type heme and FAD cofactors of cellobiose dehydrogenase, adapted from reference 75.

and as separate domains that were cleaved by papain.[66] By taking advantage of the different absorption maxima of the heme and flavin cofactors, the physical properties of each of the cofactors, such as oxidation and spin state, were extracted using RR spectroscopy. Furthermore, it was shown that visible excitation of the FAD resulted in photoreduction of the heme in the intact holoprotein. However, under the same conditions, the isolated heme domain could not be photoreduced, suggesting that electronic interactions between the domains are critical for efficient electron transfer. Such interactions between a hemes and a flavins have been seen previously in flavocytochrome b_2[63] and flavocytochrome c_{552}.[67]

Ferritin. Ferritin (FTN) is a 24 subunit protein that sequesters iron as Fe^{2+} and stores it as a polymerized mineral aggregate for later use by the organism.[68,69] Ferritin subunits isolated from frogs can be classified as either H, M, or L based on their relative electrophoretic mobilities in SDS gels[70] and display a remarkably high degree of structural similarity to each other, containing a 4-α-helix bundle similar to the iron-oxo enzymes such as ribonucleotide reductase (see Fig. 5-2).[49] Furthermore, there is strong evidence that eukaryotic H-chain ferritins contain diiron clusters similar to those observed in other diiron proteins (as in Fig. 1-3).[61] Recently, spectroscopic experiments have begun to reveal the early stages of iron uptake by recombinant frog and human ferritins composed of only a single subunit type. These experiments on FTN homopolymers have been extended to other wild-type and mutant homopolymers in order to determine the exact sites of initial iron binding.

EPR and Mössbauer spectroscopy have been used to propose a mechanism of activity described by uptake of cytosolic Fe^{2+}, oxidation of Fe^{2+} to Fe^{3+} in an O_2-dependent reaction, and mineralized core formation in the hollow cavity of the 24-subunit holoprotein.[71,72] Recent research has shown that the addition of 1 atom of Fe^{2+} per subunit of frog apoFTN-H results in a transient 550-nm absorbance in the electronic absorption spectrum attributed to an iron-tyrosinate species.[73] This interpretation was verified by collecting the resonance Raman spectrum of this intermediate and identifying 7 bands in the 550-1650-cm^{-1} range that can be assigned to various iron-tyrosinate ligand vibrations.[74] A 650-nm visible absorbance has been observed with human apoFTN-H

homopolymers incubated with 1 Fe^{2+}/subunit, suggesting that ferritin from this organism uses a different iron-protein intermediate.[72]

As described in chapter 5, time-resolved spectroscopy was used to show that the 550-nm species observed in the electronic absorption spectrum and the [Fe^{3+}-Tyr] signals in the RR spectrum were due to the same analyte. Identical experiments were performed on samples of wild-type and mutant frog FTN-H, -M, and -L homopolymers, each with a different number of conserved tyrosine residues. These experiments revealed that a specific tyrosine residue, Tyr36, Tyr133, or Tyr 147 is responsible for the rapid color formation in frog FTN-H but a different Tyr residue, probably Tyr30, is responsible for color formation by FTN-M.

Focus of present research. Two of the most important tools used by metallobiochemists today are spectroscopy and the study of model compounds. In fact, the study of short-lived intermediates in reaction mechanisms could not be possible without these methods. In this thesis, RR spectroscopy, electronic absorption spectroscopy, and inorganic model compounds have been used extensively to study the physical and chemical properties of redox-active metal clusters to identify unusual and interesting physical properties. Through these methods, the following chapters will showcase important new information in the fields of nitrogen activation, oxygen activation, intramolecular electron transfer, and iron biomineralization. These studies were undertaken in the spirit of basic research with the goal of using this information to solve practical problems in the future.

References

(1) Cramer, W. A.; Knaff, D. *Energy Transduction in Biological Membranes*; Springer-Verlag: Berlin, 1990.

(2) Tsukihara, T.; Aoyama, H.; Yamashita, E.; Tmizaki, T.; Yamaguchi, H.; Shinzawa-Itoh, K.; Nakashima, R.; Yaono, R.; Yoshikawa, S. "The Whole Structure of the 13-Subunit Oxidized Cytochrome *c* Oxidase at 2.8 Å." *Science* **1996**, *272*, 1136-1145.

(3) Danks, S. M.; Evans, E. H.; Whittaker, P. A. *Photosynthetic Systems*; Wiley & Sons: New York, 1983.

(4) Deisenhofer, J.; Epp, O.; Miki, K.; Huber, R.; Michel, H. "Structure of the Photosynthetic Reaction Centre." *Nature* **1985**, *318*, 618-624.

(5) Fausto daSilva, J. J.; Williams, R. J. P. *The Biological Chemistry of the Elements*; Clarendon Press: Oxford, 1991.

(6) Battersby, A. "How Nature Builds the Pigments of Life: The Conquest of Vitamin B12." *Science* **1994**, *264*, 1551-1557.

(7) Leeper, F. J. "The Biosynthesis of Porphyrins, Chlorophylls, and Vitamin B12." *Nat. Prod. Rep.* **1989**, *6*, 171-199.

(8) Nichol, C. A.; Smity, G. K.; Duch, D. S. "Biosynthesis and Metabolism of Tetrahydrobiopterin and Molybdopterin." *Annu. Rev. Biochem.* **1985**, *54*, 729-764.

(9) Fujita, H. *Regulation of Heme Protein Synthesis*; AlphaMed Press: Dayton, 1994.

(10) Lippard, S. J.; Berg, J. M. *Principles of Bioinorganic Chemistry*; University Science Books: Mill Valley, 1994.

(11) Sharp, R. E.; White, P.; Chapman, S. K.; Reid, G. A. "Role of the Interdomain Hinge of Flavocytochrome b_2 in Intra- and Inter-Protein Electron Transfer." *Biochemistry* **1994**, *33*, 5115-5120.

(12) Chan, M. K.; Kim, J.; Rees, D. C. "The Nitrogenase FeMo-Cofactor and P-Cluster Pair: 2.2-Å Resolution Structures." *Science* **1993**, *260*, 792-794.

(13) Hageman, R. V.; Burris, R. H. "Nitrogenase and Nitrogenase Reductase Associate and Dissociate with Each Catalytic Cycle." *Proc. Natl. Acad. Sci. U.S.A.* **1978**, *75*, 2699-2702.

(14) Cai, D.; Klinman, J. P. "Mechanism of Copper Amine Oxidase." *Biochemistry* **1994**, *33*, 7647-7653.

(15) Snyder, S. H.; Bredt, D. S. "Nitric Oxide Synthase." *Sci. Am.* **1992**, *226*, 28-36.

(16) Butler, A. R.; Williams, L. "Role of Nitric Oxide Synthase." *Chem. Soc. Rev.* **1993**, *22*, 233-251.

(17) Licht, S.; Gerfen, G. J.; Stubbe, J. "Thiyl Radicals In Ribonucleotide Reductase." *Science* **1996**, *271*, 477-481.

(18) Demetrius, L. "Evolutionary Dynamics of Enzymes." *Prot. Eng.* **1995**, *8*, 791-800.

(19) Theil, E. C. "Iron Regulatory Elements (IREs): A Family of mRNA Non-Coding Sequences." *Biochem. J.* **1994**, *304*, 1-11.

(20) Wüthrich, K. "The Development of Nuclear Magnetic Resonance Spectroscopy as a Technique for Protein Structure Determination." *Acc. Chem. Res.* **1989**, *22*, 36-44.

(21) Palmer, G. "Electron Paramagnetic Resonance." *Adv. Inorg. Biochem.* **1980**, *2*, 153-182.

(22) Gray, H. B. "Electronic Absorption Spectroscopy." *Adv. Inorg. Biochem.* **1980**, *2*, 1-26.

(23) Caughey, W. S. "Infrared Spectroscopy." *Adv. Inorg. Biochem.* **1980**, *2*, 95-115.

(24) Spiro, T. G. *Biological Applications of Raman Spectroscopy*; John Wiley & Sons: New York, 1987; Vol. 1-3.

(25) Cohen, R. L. *Applications of Mössbauer Spectroscopy*; Academic Press: New York, 1980.

(26) Scott, R. A. "X-Ray Absorption Spectroscopy of Metalloenzymes." *Meth. Enzymol.* **1985**, *117*, 414-459.

(27) Burris, R. H. "Nitrogenases." *J. Biol. Chem.* **1991**, *266*, 9339-9342.

(28) Mortenson, L. E. "Nitrogenase from *C. pasteurianum*." *Biochim. Biophys. Acta* **1964**, *81*, 473-478.

(29) Winter, H. C.; Burris, R. H. "Electron Transfer per Turnover in Nitrogenase." *J. Biol. Chem.* **1968**, *243*, 940-944.

(30) Surerus, K. K.; Hendrich, M. P.; Christie, P. D.; Rottgardt, D.; Orme-Johnson, W. H.; Münck, E. "Mössbauer and Integer-Spin EPR of the Oxidized P-Clusters of Nitrogenase." *J. Am. Chem. Soc.* **1992**, *114*, 8579-8590.

(31) Emptage, M. H.; Kent, T. A.; Kennedy, M. C.; Beinert, H.; Münck, E. "Mössbauer and EPR Studies of Activated Aconitase." *Proc. Natl. Acad. Sci. U.S.A.* **1983**, *80*, 4674-4678.

(32) Chisnell, J. R.; Premakumar, R.; Bishop, P. E. "Purification of a Second Alternative Nitrogenase" *J. Bacteriol.* **1988**, *170*, 27-33.

(33) Bishop, P. E.; Jarlenski, D. M.; Hetherington, D. R. "Alternative Nitrogenases." *Proc. Natl. Acad. Sci. U.S.A.* **1980**, *77*, 7342-7346.

(34) Georgiadis, M. M.; Komiya, H.; Chakrabarti, P.; Woo, D.; Kornuc, J. J.; Rees, D. C. "Crystallographic Structure of the Nitrogenase Iron Protein from *Azotobacter vinelandii*." *Science* **1992**, *257*, 1653-1659.

(35) Kim, J.; Rees, D. C. "Crystallographic Structure and Functional Implications of the Nitrogenase Molybdenum-Iron Protein from *Azotobacter vinelandii*." *Nature* **1992**, *360*, 553-560.

(36) Kim, J.; Woo, D.; Rees, D. C. "X-ray Crystal Structure of the Nitrogenase Molybdenum-Iron Protein from *Clostridium pasteurianum* at 3.0-Å Resolution." *Biochemistry* **1993**, *32*, 7104-7115.

(37) Shah, V. K.; Brill, W. J. "Isolation of an Iron-Molybdenum Cofactor from Nitrogenase." *Proc. Natl. Acad. Sci. U.S.A.* **1977**, *74*, 3249-3253.

(38) Burgess, B. K. "The Iron-Molybdnum Cofactor of Nitrogenase." *Chem. Rev.* **1990**, *90*, 1377-1406.

(39) Deng, H.; Hoffmann, R. "How N_2 Might Be Activated by the FeMo-Cofactor in Nitrogenase." *Angew. Chem. Int. Ed. Engl.* **1993**, *32*, 1062-1065.

(40) Orme-Johnson, W. H. "Nitrogenase Structure: Where to Now?" *Science* **1992**, *257*, 1639-1640.

(41) Laplaza, C. E.; Cummins, C. C. "Dinitrogen Cleavage by a Three-Coordinate Molybdenum(III) Complex." *Science* **1995**, *268*, 861-863.

(42) Laplaza, C. E.; Johnson, M. J.; Peters, J. C.; Odom, A. L.; Kim, E.; Cummins, C. C.; George, G. N.; Pickering, I. J. "Dinitrogen Cleavage by Three-Coordinate Molybdenum(III) Complexes: Mechanistic and Structural Data." *J. Am. Chem. Soc.* **1996**, *118*, 8623-8638.

(43) Fryzuk, M. D.; Haddad, T. S.; Rettig, S. J. "Reduction of Dinitrogen by a Zirconium Phosphine Complex to Form a Side-On-Bridging N_2 Ligand" *J. Am. Chem. Soc.* **1990**, *112*, 8185-8186.

(44) Fryzuk, M. D.; Haddad, T. S.; Mylvaganam, M.; McConville, D. H.; Rettig, S. "End-on versus Side-On Bonding of Dinitrogen to Dinuclear Early Transition-Metal Complexes." *J. Am. Chem. Soc.* **1993**, *115*, 2782-2792.

(45) Stubbe, J. "Ribonucleotide Reductases." *Adv. Enzymol.* **1989**, *63*, 349-419.

(46) Nordlund, P.; Sjöberg, B.-M.; Eklund, H. "Three-Dimensional Structure of the Free Radical Protein of Ribonucletode Reductase." *Nature* **1990**, *345*, 593-598.

(47) Nordlund, P.; Eklund, H. "Crystal Structure of the R2 Subunit of Mammalian Ribonucleotide Reductase Expressed in *E. coli*." *J. Mol. Biol.* **1993**, *232*, 123-164.

(48) Fox, B. G.; Shanklin, J.; Ai, J.; Loehr, T. M.; Sanders-Loehr, J. "Resonance Raman Evidence for an Fe-O-Fe Center in Stearoyl-ACP Desaturase. Primary Sequence Identity with Other Diiron-Oxo Proteins." *Biochemistry* **1994**, *33*, 12776-12786.

(49) Nordlund, P.; Eklund, H. "Di-Iron-Carboxylate Proteins." *Curr. Op. Struct. Biol.* **1995**, *5*, 758-766.

(50) Sturgeon, B. E.; Burdi, D.; Chen, S.; Huynh, B.-H.; Edmondson, D. E.; Stubbe, J.; Hoffman, B. M. "Reconsideration of X, the Diiron Intermediate Formed During Cofactor Assembly in *E. coli* Ribonucleotide Reductase." *J. Am. Chem. Soc.* **1996**, *118*, 7551-7557.

(51) Bollinger, J. M.; Edmondson, D. E.; Huynh, B. H.; Filley, J.; Norton, J.; Stubbe, J. "Mechanism of Assembly of the Tyrosyl Radical-Dinuclear Iron Cluster Cofactor of Ribonucleotide Reductase." *Science* **1991**, *253*, 292-298.

(52) Bollinger, J. M.; Tong, W. H.; Ravi, N.; Huynh, B. H.; Ednondson, D. E.; Stubbe, J. "Mechanism of Assembly of the Tyrosyl-Radical Diiron(III) Cofactor of E. coli

Ribonucleotide Reductase. 3. Kinetics of the Limiting Fe^{2+} Reaction by Optical, EPR, and Mössbauer Spectroscopies." *J. Am. Chem. Soc.* **1994**, *116*, 8024-8032.

(53) Bollinger, J. M.; Tong, W. H.; Ravi, N.; Huynh, B. H.; Edmondson, D. E.; Stubbe, J. "Mechanism of Assembly of the Tyrosyl-Radical Diiron(III) Cofactor of *E. coli* Ribonucleotide Reductase. 2. Kinetics of the Excess Fe^{2+} Reaction by Optical, EPR, and Mösbauer Spectroscopies." *J. Am. Chem. Soc.* **1994**, *116*, 8015-8023.

(54) Ravi, N.; Bollinger, J. M.; Tong, W. H.; Huynh, B. H.; Edmondson, D. E.; Stubbe, J. "Mechanism of Assembly of the Tyrosyl-Radical Diiron(III) Cofactor of *E. coli* Ribonucleotide Reductase. 1. Mössbauer Characterization of the Diferric Radical Precursor." *J. Am. Chem. Soc.* **1994**, *116*, 8007-8014.

(55) Liu, K. E.; Wang, D.; Huynh, B. H.; Edmondson, D. E.; Salifoglou, A.; Lippard, S. J. "Kinetic and Spectroscopic Characterization of Intermediates and Component Interactions in Reactions of Methane Monooxygenase from *Methylococcus capsulatus* (Bath)." *J. Am. Chem. Soc.* **1995**, *117*, 10174-10185.

(56) Lee, S.-K.; Nesheim, J. C.; Lipscomb, J. D. "Transient Intermediates of the Methane Monooxygenase Catalytic Cycle." *J. Biol. Chem.* **1993**, *268*, 21569-21577.

(57) Ling, J.; Sahlin, M.; Sjöberg, B.-M.; Loehr, T. M.; Sanders-Loehr, J. "Dioxygen is the Source of the μ-Oxo Bridge in Ribonucleotide Reductase." *J. Biol. Chem.* **1994**, *269*, 5595-5601.

(58) Dong, Y.; Fujii, H.; Hendrich, M. P.; Leising, R. A.; Pan, G.; Randall, C. R.; Wilkinson, E. C.; Zang, Y.; Que Jr., L.; Fox, B. G.; Kauffmann, K.; Münck, E. "A High-Valent Nonheme Intermediate. Structure and Properties of $[Fe_2(\mu\text{-}O)2(5\text{-}Me\text{-}TPA)_2](ClO_4)_3$." *J. Am. Chem. Soc.* **1995**, *117*, 2778-2792.

(59) Debrunner, P. G.; Hendrich, M. P.; de Jersey, J.; Keough, D. T.; Sage, J. T.; Zerner, B. "Mössbauer and EPR Study of the Binuclear Iron Center of Purple Acid Phosphatase." *Biochim. Biophys. Acta* **1983**, *745*, 103-106.

(60) De Vocht, M. L.; Kooter, I. M.; Bulsink, Y. B.; Hagen, W. R.; Johnson, M. K. "Resonance Raman Evidence for Non-Heme Fe-O Species in the [6Fe-6S]-Containing Iron-Sulfur Proteins from Sulfate-Reducing Bacteria." *J. Am. Chem. Soc.* **1996**, *118*, 2766-2767.

(61) Chasteen, N. D.; Theil, E. C. "Fe Binding by Horse Spleen Apoferritin." *J. Biol. Chem.* **1982**, *257*, 7672-7677.

(62) Xia, Z.-X.; Shamala, N.; Bethge, P. H.; Lim, L. W.; Bellamy, H. D.; Xuong, N. H.; Lederer, F.; Mathews, F. S. "Three-Dimensional Structure of Flavocytochrome b_2 from Baker's Yeast at 3.0-Å Resolution." *Proc. Natl. Acad. Sci. U.S.A.* **1987**, *84*, 2629-2633.

(63) Sharp, R. E.; Chapman, S. K.; Reid, G. A. "Deletions in the Interdomain Hinge Region of Flavocytochrome b_2: Effects on Intraprotein Electron Transfer." *Biochemsitry* **1996**, *35*, 891-899.

(64) Tegoni, M.; Begotti, S.; Cambillau, C. "X-ray Structure of Two Complexes of the Y143F Flavocytochrome b_2 Mutant Crystallized in the Presence of Lactate or Phenyl Lactate." *Biochemistry* **1995**, *34*, 9840-9850.

(65) Desbois, A.; Tegoni, M.; Gervais, M.; Lutz, M. "Flavin and Heme Structures in Lactate:Cytochrome *c* Oxidoreductase: A Resonance Raman Study." *Biochemsitry* **1989**, *28*, 8011-8022.

(66) Henriksson, G. P., G.; Johansson, G.; Ruiz, A.; Uzcategui, E. "Cellobiose Oxidase from *Phanerochaete chrysosporium* can be Cleaved by Papain into Two Domains." *Eur. J. Biochem.* **1991**, *196*, 101-106.

(67) Kitagawa, T.; Fukumori, Y.; Yamanaka, T. "Resonance Raman Evidence for Intrameolecular Electron Tansport from Flavin to Heme in Flavocytchrome *c*-552 and the Nature of Chromophoric Interactions." *Biochemsitry* **1980**, *19*, 5721-5729.

(68) Harrison, P. M.; Arosio, P. "The Ferritins: Molecular Properties, Iron Storage Function and Cellular Regulation." *Biochim. Biophys. Acta* **1996**, *1275*, 161-203.

(69) Waldo, G. S.; Theil, E. C. "Ferritin and Iron Biomineralization." *Comp. Supra. Struct.* **1996**, *5*.

(70) Dickey, L. F.; Sreedharan, S.; Theil, E. C.; Didsbury, J. R.; Wang, Y.-H.; Kaufman, R. E. "Differences in the Regulation of Messenger RNA for Housekeeping and Specialized-cell Ferritin." *J. Biol. Chem.* **1987**, *262*, 7901-7907.

(71) Harrison, P. M.; Bauminger, E. R.; Hechel, D.; Hodson, N. W.; Nowik, I.; Treffry, A.; Yewdall, S. J. "Mechanism of Fe(II) Oxidation and Core Formation in Ferritin;" in *Progress in Iron Research*; Hershko, C., Ed.; Clarendon Press: Oxford; 1994, pp. 1-12.

(72) Treffry, A.; Hirzmann, J.; Yewdall, S. J.; Harrison, P. M. "Mechanism of Catalysis of Fe(II) Oxidation by Ferritin H Chains." *FEBS Lett.* **1992**, *302*, 108-112.

(73) Waldo, G. S.; Theil, E. C. "Formation of Iron (III)-Tyrosinate is the Fastest Reaction Observed in Ferritin." *Biochemistry* **1993**, *32*, 13262-13269.

(74) Waldo, G. S.; Ling, J.; Sanders-Loehr, J.; Theil, E. C. "Formation of an Fe(III)-Tyrosinate Complex During Biomineralization of H-Subunit Ferritin." *Science* **1993**, *259*, 796-798.

(75) Dong, Y.; Que Jr., L. "Modeling the Oxygen Activation Chemistry of Methane Monooxygenase and Ribonucleotide Reductase." *Acc. Chem. Res.* **1996**, *29*, 190-196.

(76) Bao, W.; Usha, S. N., Renganathan, V. "Purification and Characterization of Cellobiose Dehydrogenase from *Phanaerochaete chrysosporium*." *Arch. Biochem. Biophys.* 1993, 300, 705-713.

Chapter 2

N_2 Bound to Zr_2 Clusters as Models of Nitrogenase. Distinguishing the μ–η^1:η^1 and μ–η^2:η^2 States by RR Spectroscopy

Jonathan D. Cohen,[1] Murugesapillai Mylvaganam,[2] Michael D. Fryzuk,*[,2] and Thomas M. Loehr*[,1]

(Manuscript originally published as, "Resonance Raman Studies of Dinuclear Zirconium Complexes with a Bridging Dinitrogen Ligand. Possible N_2-Coordination Models for Nitrogenase" *J. Am. Chem. Soc.* **1994**, *116*, 9529-9534.)

Abstract

Resonance Raman spectroscopy was used to investigate the vibrational properties of the bridging dinitrogen ligand in two different dinuclear zirconium complexes known to contain unusually long N-N bonds. $\{[(Pr^i_2PCH_2SiMe_2)_2N]Zr(\eta^5\text{-}C_5H_5)\}_2(\mu\text{-}\eta^1\text{:}\eta^1\text{-}N_2)$ (**1**) has an "end-on" bridging dinitrogen ligand and $\{[(Pr^i_2PCH_2SiMe_2)_2N]ZrCl\}_2(\mu\text{-}\eta^2\text{:}\eta^2\text{-}N_2)$ (**2**) has a "side-on" bridging dinitrogen ligand. The ν(N-N) stretching frequency for the μ-η^1:η^1-N_2 complex is observed at 1211 cm^{-1} in the solid state, and confirmed by an ~40-cm^{-1} isotope shift in the $^{15}N_2$-substituted isotopomer. A similar frequency and isotope shift are observed for **1** in toluene, indicating that the μ-η^1:η^1-N_2 structure is preserved in solution. Vibrational assignments for the μ-η^2:η^2-N_2 complex **2** are complicated by the presence of many isotope-sensitive peaks in the

solid state. Nevertheless, we propose that the intense peak at ~731 cm^{-1} corresponds to one of the totally symmetric A_g modes of the Zr_2N_2 moiety that is predominantly ν(N-N) in character based on its ~22-cm^{-1} isotope shift and its strong polarization in THF solution. The majority of the remaining peaks in the resonance Raman spectrum of **2** can be assigned as overtone and combination bands of fundamental modes at 258, 317, 393 cm^{-1} and the ν(N-N) mode at 731 cm^{-1} (709 cm^{-1} in the ^{15}N isotopomer). Comparison of solid and solution state data for **2** suggests that the structure of the side-on-bonded N_2 ligand is largely maintained in THF solution. Finally, the vibrational spectroscopic properties of **2** as the dibromo and the mixed bromochloro complex are reported. These complexes all maintain the strong ν(N-N) mode at 709 cm^{-1} (^{15}N isotopomers), but exhibit changes in the fundamental modes at ~300 cm^{-1}, and hence, also for the resulting overtone and combination bands. This work has shown that resonance Raman spectra reveal very marked differences and, hence, can be used to distinguish the two modes of bonding in side-on versus end-on coordinated N_2 complexes of dinuclear transition metals. Furthermore, the high degree of nitrogen activation by these compounds suggests that N2 activation by nitrogenase is possible with N_2 bound with either "end-on" or "side-on" geometry.

Introduction

Nitrogen fixation is the process by which N_2 is reduced to NH_3. Industrially, the reduction of N_2 to NH_3 is accomplished at ~150 atm and ~550 °C in the presence of H_2 using an iron-based catalyst in the well-known Haber-Bosch process. Biological nitrogen fixation occurs at ambient temperature and pressure when catalyzed by nitrogenase, a multiprotein complex found in nitrogen-fixing microorganisms.[3,4] The crystal structures of the MoFe proteins of the nitrogenases of *Azotobacter vinelandii* and *Clostridium pasteurianum* were recently reported.[5,6] These proteins contain a unique cofactor containing iron and

molybdenum that is believed to be the site of N_2 reduction.[7] Unfortunately, the crystal structures of these proteins do not provide information regarding either the location or the geometry of substrate binding. Nonetheless, several molecular-orbital simulations of N_2 binding as simplified variants of the FeMo cofactor have been investigated (*vide infra*).[8] The synthesis of iron-molybdenum clusters has been pursued vigorously in several laboratories in attempts to prepare functional models of the nitrogenase chemistry.[9-11] However, other transition-metal complexes of N_2 may also serve as model compounds to provide useful insights into N_2 bonding and activation through metal complexation.

In 1965, Allen and Senoff reported the synthesis of $[Ru(NH_3)_5N_2]^{2+}$, the first compound known to have a dinitrogen ligand terminally bound to a transition metal.[12] Since then, the catalog of complexes containing terminal and/or bridging N_2 ligands has grown immensely.[13-19] However, most of these complexes show little extension of the N-N bond from its gas-phase equilibrium value of 1.0975 Å.[20] Nevertheless, there are a few metal-dinitrogen complexes with N-N bond lengths significantly greater than ~1.1 Å.[21-28] Although lengthening of the N_2 bond upon metal complexation does not, by itself, denote a particular compound's ability to fix nitrogen,[18b] one must logically conclude that elongation (accompanied by protonation) and eventual N-N bond dissociation are necessary for the reduction of 1 mol N_2 to 2 mol NH_3 in the biological reaction sequence.

Recently, two dinuclear zirconium-dinitrogen complexes with unusually long N-N bonds have been synthesized (Figures 2-1 and 2-2).[21] Complex **1**, $\{[(Pr^i_2PCH_2SiMe_2)_2N]Zr(\eta^5\text{-}C_5H_5)\}_2(\mu\text{-}\eta^1\text{:}\eta^1\text{-}N_2)$, has an N_2 ligand bridging the two Zr atoms with a nearly linear "end-on" geometry (Fig. 2-1). Its N-N bond length of 1.30 Å determined from X-ray crystallography represents a very significant increase from that of the $N_2(g)$ equilibrium value.[21] Complex **2**, $\{[(Pr^i_2PCH_2SiMe_2)_2N]ZrCl\}_2(\mu\text{-}\eta^2\text{:}\eta^2\text{-}N_2)$, contains a rare example of an N_2 ligand bridging both metal atoms with "side-on" geometry and exhibits an N-N bond length of 1.548 Å in the crystal structure[21,29] (Fig. 2-2). In fact, complex **2** has the longest reported N-N bond length for any metal-dinitrogen complex.[29] Deng

Zr–N 1.92 Å

N–N 1.30 Å

Zr–N–N 170°

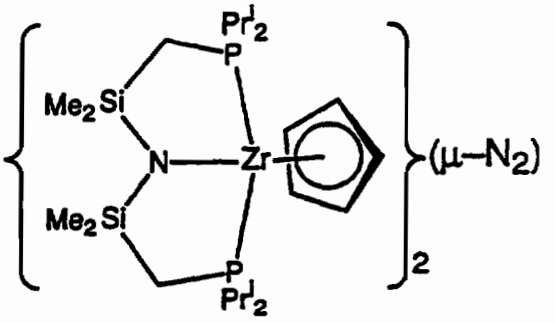

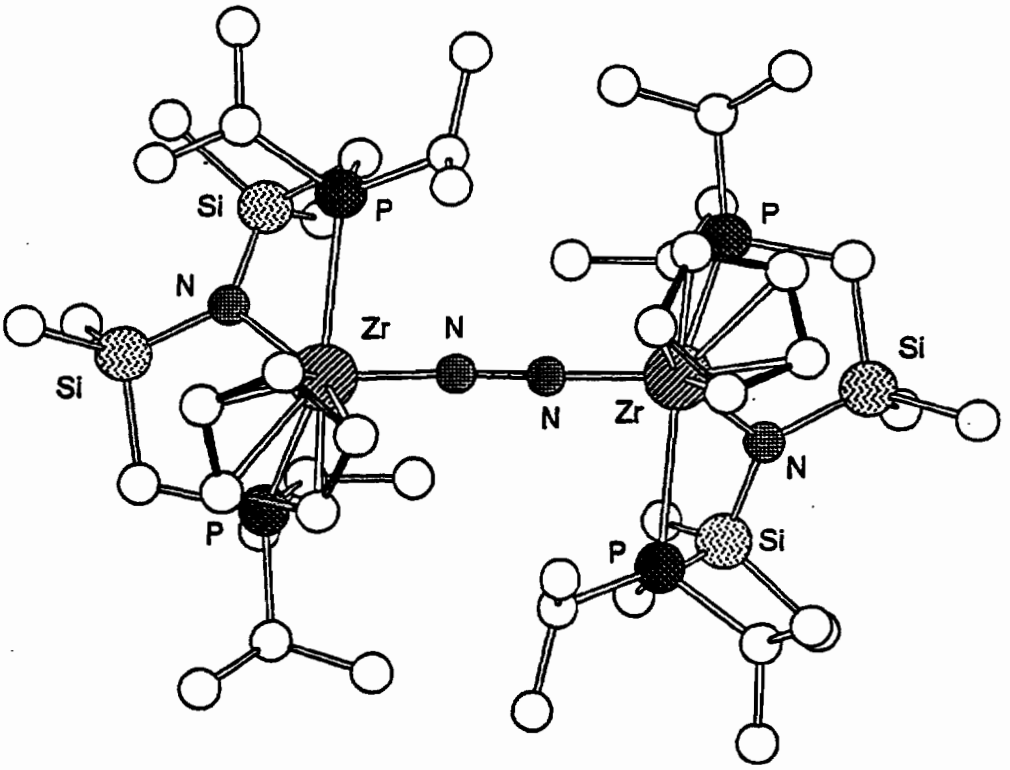

Figure 2-1. Molecular structure of complex **1** shown as a ball-and-stick model and several important (μ-η^1:η^1 -N_2)Zr_2N' bonding parameters; adapted from Ref. 21.

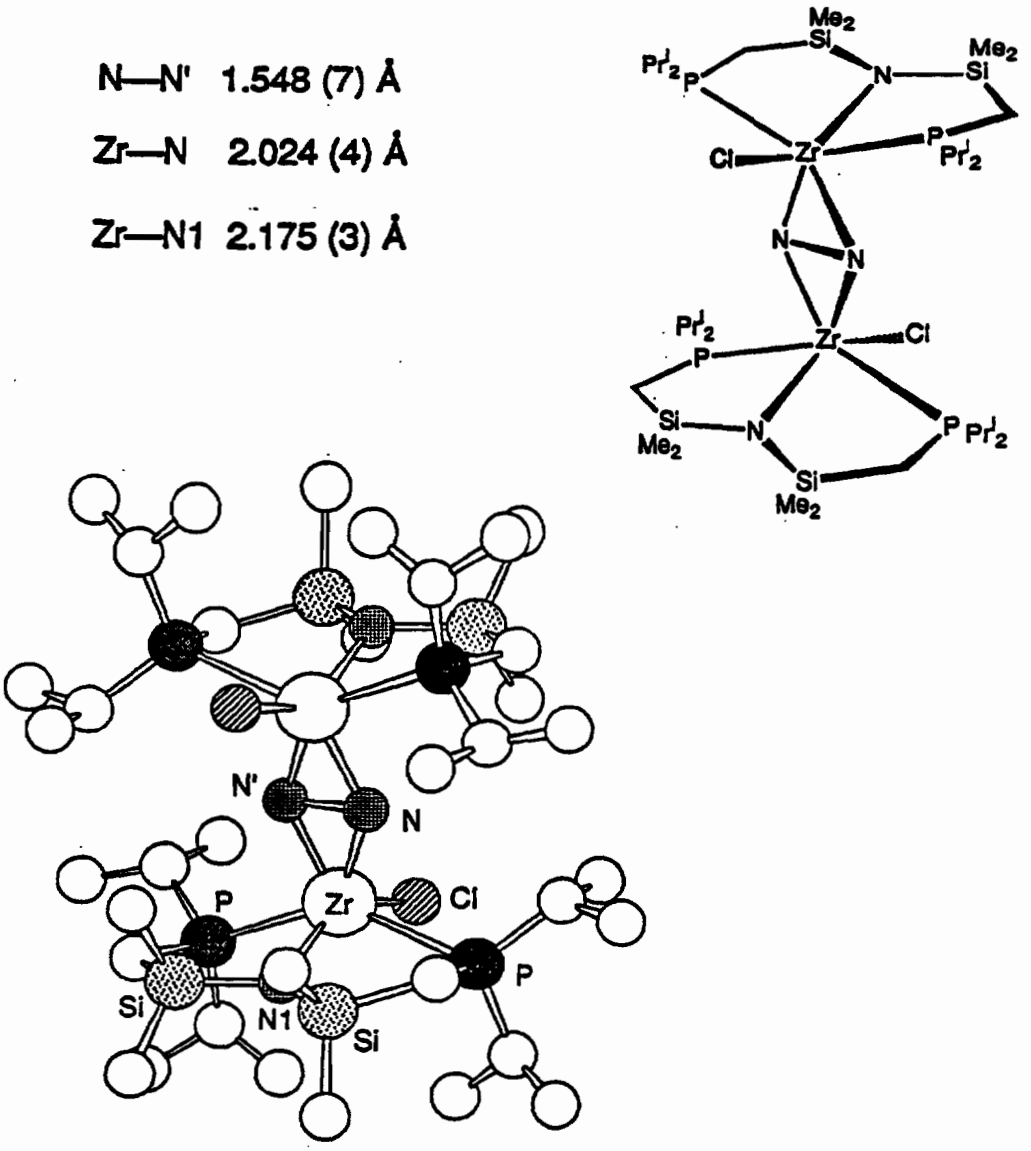

Figure 2-2. Molecular structure of complex **2** shown as a ball-and-stick model and several important $(\mu\text{-}\eta^2\text{:}\eta^2\text{-}N_2)Zr_2N'$ bonding parameters; adapted from Ref. 21.

and Hoffmann propose that this side-on geometry is one of the preferred coordination models of N_2 binding to the FeMo cofactor of nitrogenase based on the low calculated N-N overlap population, which facilitates bond dissociation, and the increased net negative charge on each of the nitrogen atoms necessary for protonation (see below).[8]

For the two dinuclear Zr complexes **1** and **2**, semi-empirical MO calculations have shown that the preference for end-on versus side-on binding of the dinitrogen ligand can be accounted for by suitable choices of the ancillary ligands.[21] However, attempts to extend the range of complexes that contain the rare side-on binding mode have been hampered by the fact that distinguishing between side-on and end-on modes of ligation is non-trivial. Infrared spectroscopy as well as solid- and solution-state ^{15}N-NMR spectroscopy have been decidedly ambiguous. Up to the present, only single-crystal X-ray crystallography has been unequivocal. In this paper, we report a resonance Raman (RR) study of these compounds to characterize the vibrational frequencies of end-on and side-on dinitrogen ligands in transition-metal complexes. In addition, we are interested in establishing the structural identity of these complexes in solution and determining if there is any structural isomerism of the dinitrogen ligand. Owing to the high local symmetry of the dinitrogen stretching mode, Raman and/or resonance Raman (RR) spectroscopy are the only analytical methods available to directly observe the N-N stretching frequency, and this technique has been previously used in the study of bridging N_2 complexes.[25,30] For the end-on complex **1**, we have identified ν(N-N) in the RR spectrum at 1211 cm^{-1} on the basis of its single isotope-sensitive frequency. In contrast, RR spectra of the side-on complex **2** show many isotope-sensitive bands; however, the predominant ν(N-N) is observed at 731 cm^{-1}. The remaining bands in the spectra of **2** are assigned to a few fundamental modes and to many overtone and combination bands of the Zr_2N_2 moiety. Moreover, in complex **2**, the position and intensity of the RR spectral features are sensitive to the nature of the ancillary ligands as well as to whether the sample is in the solid phase or in solution.

Experimental

Preparation of Compounds. Crystals and solutions of $\{[(Pr^{i}_2PCH_2SiMe_2)_2N]Zr(\eta^5\text{-}C_5H_5)\}_2(\mu\text{-}\eta^1\text{:}\eta^1\text{-}N_2)$ (**1**, reddish-brown, λ_{max} ~490 nm) and $\{[(Pr^{i}_2PCH_2SiMe_2)_2N]ZrCl\}_2(\mu\text{-}\eta^2\text{:}\eta^2\text{-}N_2)$ (**2**, deep blue, λ_{max} ~580 nm), were prepared by methods described elsewhere.[21] Isotopic substitution with $^{15}N_2$ was carried out by degassing the starting materials and introducing $^{15}N_2$ into the reaction mixture. Typical sample concentrations were between 100 and 300 mg/L. All samples were anaerobically sealed under nitrogen in 1.5-1.8 × 90 mm Kimax glass capillary tubes and stored at room temperature until studied.[31]

Synthesis of $[(Pr^{i}_2PCH_2SiMe_2)_2N]ZrBr_3$. To a suspension of $ZrBr_4$ (2.03 g, 4.94 mmol) in toluene (50 mL) was added a solution of $[(Pr^{i}_2PCH_2SiMe_2)_2N]Li$ (1.00 g, 2.50 mmol) in toluene (10 mL) at room temperature (RT). The reaction mixture was stirred for 16 h, and then the LiCl salt was removed by filtering through Celite. The filtrate was concentrated to 15 mL and hexanes were added until the solution turned turbid; cooling at -30 °C yielded a colorless crystalline product (1.12 g, 73%). ^{1}H NMR (δ, 200.123 MHz, C_6D_6): 0.41 (s, 12H, $Si(CH_3)_2$); 1.11 (m, 28H, $P[CH(CH_3)_2]_2$, $SiCH_2P$); 2.07 (sept of triplets, 4H, $P[CH(CH_3)_2]_2$, $^2J_{H\text{-}P}$ = 2.7 Hz, $^3J_{H\text{-}H}$ = 7.2 Hz). $^{31}P\{^1H\}$ NMR (δ, 81.015 MHz, C_6D_6): 16.52 (s). $^{13}C\{^1H\}$ NMR (δ, 50.323 MHz, C_6D_6): 4.50 (s, $Si(CH_3)_2$); 11.93 (s, $SiCH_2P$); 18.85 (s, $P[CH(CH_3)_2]_2$); 19.12 (s, $P[CH(CH_3)_2]_2$); 25.14 (t, $P[CH(CH_3)_2]_2$, $^2J_{C\text{-}P}$ = 6.8 Hz). Anal. Calcd for $C_{18}H_{44}Br_3NP_2Si_2Zr$: C, 29.88; H, 6.13; N, 1.94. Found: C, 30.00; H, 6.30; N, 1.99.

Synthesis of $\{[(Pr^{i}_2PCH_2SiMe_2)_2N]ZrBr\}_2(\mu\text{-}\eta^2\text{:}\eta^2\text{-}N_2)$. A solution of $ZrBr_3[N(SiMe_2CH_2PPr^{i}_2)_2]$ (0.628 g, 0.943 mmol) in toluene (80 mL) was transferred into a thick-walled reaction flask (300 mL), equipped with a 10-mm Teflon needle valve, and containing 0.35% Na/Hg (24 g, 3.59 mmol). The flask was then cooled to -196 °C, filled with N_2, sealed, and allowed to warm slowly to

RT with stirring. The colorless solution slowly takes on the deep blue color of the product. The reaction mixture was stirred for 7 d, and then filtered through a layer of Celite. The amalgam-containing residue was extracted with several 80-mL portions (~1 L) of toluene until the extracts showed no blue color. Upon removal of the toluene under vacuum, the product separates out as crystalline material (0.23 g, 42%). ^{1}H NMR (δ, 300 MHz, C_7D_8): 0.30 (s, 12H, Si(CH_3)$_2$); 0.34 (s, 12H, Si(CH_3)$_2$); 1.02 (m, 8H, SiCH_2P); 1.44 (d of d, 12H, P[CH(CH_3)$_2$]$_2$, $^3J_{H\text{-}H}$ = 7.3 Hz, $^2J_{H\text{-}P}$ = 13.7 Hz); 1.24 (m, 36H, P[CH(CH_3)$_2$]$_2$); 2.18 (d of sept, 4H, P[CH(CH_3)$_2$]$_2$, $^3J_{H\text{-}H}$ = 7.5 Hz, $^2J_{H\text{-}P}$ = 4.2 Hz); 2.42 (d of sept, 4H, P[CH(CH_3)$_2$]$_2$, $^3J_{H\text{-}H}$ = 7.6 Hz, $^2J_{H\text{-}P}$ = 3.9 Hz). ^{31}P{^{1}H} NMR (δ, 121.4 MHz, C_7D_8): 9.96 (s). Anal. Calcd for $C_{18}H_{44}BrN_2P_2Si_2Zr$: C, 37.42; H, 7.68; N, 4.85. Found: C, 37.84; H, 7.84; N, 3.89. The lower nitrogen content found is probably due to the formation of nitrides during combustion.

Synthesis of {[(Pr$^i_2$PCH$_2$SiMe$_2$)$_2$N]ZrBr}$_2$(μ-η^2:η^2-^{15}N$_2$). The $^{15}N_2$ analogue was prepared by a procedure similar to the synthesis of the unlabeled compound by introducing $^{15}N_2$ gas into the flask containing the degassed reaction mixture at RT. Workup was carried out under unlabelled N_2. ^{15}N{^{1}H} NMR (δ, 30.406 MHz, THF/ C_6D_6): 345.75 (s). MS: Calcd for M^+: 1158. Found (EI) *m/z*: 1158, 1113, 1025, 941, 895, 350, 262.

Synthesis of {[(Pr$^i_2$PCH$_2$SiMe$_2$)$_2$N]Zr}$_2$ClBr (μ-η^2:η^2-N$_2$). A solution containing a mixture of ZrBr$_3$[N(SiMe$_2$CH$_2$PPr$^i_2$)$_2$] (0.160 g, 0.221 mmol) and ZrCl$_3$[N(SiMe$_2$CH$_2$PPr$^i_2$)$_2$] (0.131 g, 0.222 mmol) was treated with 0.34% Na/Hg (12.2 g, 1.79 mmol) as described in the synthesis of {[(Pr$^i_2$PCH$_2$SiMe$_2$)$_2$N]ZrBr}$_2$(μ-η^2:η^2-N$_2$). ^{1}H {^{31}P} NMR (δ, 500 MHz, C_7D_8): 0.28 (s, Si(CH_3)$_2$); 0.29 (s, Si(CH_3)$_2$); 0.31 (s, Si(CH_3)$_2$); 0.32 (s, Si(CH_3)$_2$); 0.33 (s, Si(CH_3)$_2$); 0.34 (s, Si(CH_3)$_2$); 0.65 (m, SiCH_2P); 1.00 (m, SiCH_2P); 1.28 (m, P[CH(CH_3)$_2$]$_2$); 1.41 (m, P[CH(CH_3)$_2$]$_2$); 2.40 (m, P[CH(CH_3)$_2$]$_2$). ^{31}P{^{1}H} NMR (δ, 121.4 MHz, C_7D_8): 10.30 (s); 10.06 (s); 9.96 (s); 9.89 (s). MS: Calcd for M^+: 1111. Found (EI) *m/z*: 1111, 1067, 1023, 979, 262.

Synthesis of $\{[(Pr^i_2PCH_2SiMe_2)_2N]Zr\}_2ClBr$ (μ-η^2:η^2-$^{15}N_2$). The $^{15}N_2$ analogue was prepared by a procedure similar to the synthesis of the unlabeled compound by introducing $^{15}N_2$ gas into the flask containing the degassed reaction mixture. Workup was carried out under unlabeled N_2. $^{15}N\{^1H\}$ NMR (δ, 30.406 MHz, C_4H_8O/C_6D_6): 352.50 (s, ~1N); 349.26 (s, ~2N); 345.75 (s, ~1N). MS: Calcd for M^+: 1113. Found (EI) *m/z*: 1113, 1069, 1025, 981, 895, 849, 350, 262.

Resonance Raman Spectroscopy.[32] Spectra were recorded at ~90 K by placing the capillaries containing the microcrystalline or the solution samples in a copper cold finger within a Dewar filled with liquid N_2. Raman spectra were obtained on a modified Jarrell-Ash model 25-300 Raman spectrophotometer equipped with an RCA C31034 photomultiplier tube and controlled by an Intel 310 computer. Excitation radiation was supplied by Spectra Physics Ar^+ and Kr^+ lasers operating at 514.5 and 647.1 nm, respectively, and by a Coherent CR-599 dye (rhodamine 6G) laser tuned to 580 nm and pumped by a Coherent INNOVA 90-6 Ar^+ laser. Plasma emissions from the lasers were removed with an Applied Photophysics prism filter monochromator. Scattered radiation was collected in a backscattering geometry. Multiple scans were collected and calibrated against toluene, CCl_4, and/or THF. The reported frequency positions of all strong, sharp peaks are estimated to be accurate to ± 2 cm^{-1}. Spectra for polarization studies of solution samples were collected in a 90°-scattering geometry at ~278 K on a DILOR Z-24 Raman spectrophotometer interfaced to an IBM PC/AT computer. Typical slit-width settings were between 5 and 10 cm^{-1}. All spectral data were analyzed and processed with *GRAMS/386*®or *LabCalc*® (Galactic Industries, Salem, NH) or with *Origin* (MicroCal Software, Northampton, MA).

Results and Discussion

Vibrational Spectra of $Zr_2(\mu$-η^1:η^1-$N_2)$ Complexes. The RR spectra of complex **1** in the solid state and its $^{15}N_2$-enriched isotopomer are shown in Figure

2-3. For these experiments, only the nitrogen atoms of the bridging ligand are isotopically labeled. Clearly, the most prominent feature in Figure 2-3A is the strong peak at 1211 cm^{-1}. In addition, weaker peaks are apparent at 1126, 1012, 997, 763, 325, 295, 277, and 226 cm^{-1}. The 1211-cm^{-1} peak shifts to 1172 cm^{-1} in the μ-η^1:η^1-$^{15}N_2$-isotopomer (Fig. 2-3B) and is the *only* feature to exhibit a significant isotope shift. The magnitude of this isotope shift is nearly equal to that predicted for a simple diatomic oscillator (calcd, 41 cm^{-1}, obsd, 39 cm^{-1}) and, thus, indicates that the observed mode is essentially a pure ν(N-N) stretching mode. Frequencies and the proposed assignment of ν(N-N) for complex **1** are given in Table 2-1.

The difference between the diatomic stretching frequency of N_2 (g) reported[33] at 2331 cm^{-1} and the same vibration observed at 1211 cm^{-1} in complex **1** implies a significant elongation of the dinitrogen bond with a concomitant decrease in the N-N bond order from 3 in N_2(g) to a value between 1 and 2 in complex **1**. In Figure 2-4, the N-N frequencies for a number of dinitrogen-containing compounds of different bond orders are plotted versus the 3/2-power of their N-N bond lengths.[34] The correlation is highlighted by a linear-least-squares fit (R = 0.95), and is interesting in view of the relative positions of complexes **1** and **2**. The former lies approximately midway, in both frequency and bond length, between representative N-N single and double bond values. The point for complex **2** is quite remarkable, and shows the excellent correlation between its very long bond length and its low ν(N-N) (see discussion in following section).

The RR spectrum of complex **1** in toluene solution is nearly identical to that in the solid state (Fig. 2-5A). The intense peak found in the solid at 1211 cm^{-1} now appears at 1202 cm^{-1}, and it shifts to 1165 cm^{-1} in the $^{15}N_2$-isotopomer (Fig. 2-5B). This isotope shift is within 4 cm^{-1} of that predicted for a pure ν(N-N) vibrational mode. The presence of solvent also causes some spectral changes in the low-frequency region (Table 2-1). Nearly all other minor peaks in the spectra of **1** in solution are assignable as toluene bands,[36] as indicated in Figure 2-5. In

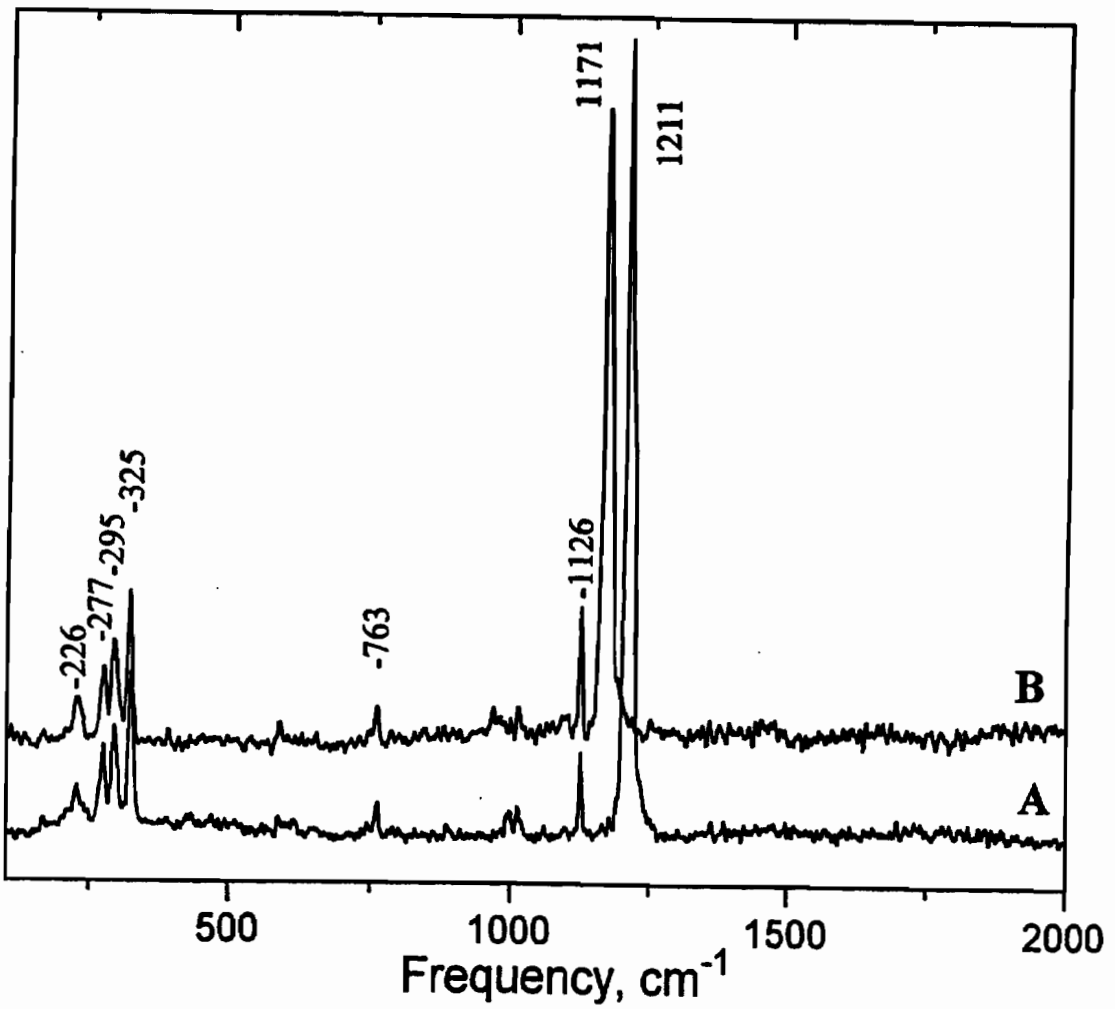

Figure 2-3. Resonance Raman spectra of complex 1 in the solid state at ~90 K. (A) μ-η^1:η^1-N_2, (B) μ-η^1:η^1-$^{15}N_2$ isotopomer. Each trace is a sum of 5 consecutive scans each recorded at 2 cm^{-1}/s using 40 mW of 514.5-nm laser excitation.

Table 2-1: Resonance Raman Frequencies and Proposed Assignments for the dinuclear Zr_2N_2 complexes **1** and **2**.

1[b] (solid)		1[c] (sol'n)		assgnmt	2[d], dichloro (solid)		2[e], dichloro (solution)		assgnmt	2[f], dibromo	assgnmt
					132					179	
226	(+2)	225			258		262 *p*	(-2)	A	295	A
277					317	(-1)?	321/331 *p*	(-3/-4)	B		
295		289			394				C		
					448						
325		320	(-2)		515				2A		
					578		585		A + B	589	2A
					633				2B		
					710				B + C		
763					731	(-22)	733/745 *p*	(-23/-26)	D; ν(N-N)	710	B; ν(N-N)
					892				A + 2B		
997					991	(-23)	1002		A + D	880	3A
1012					1046	(-22)			B + D	1009	A + B
1126		1125	(-1)		1124	(-21)	1074		C + D	1167	4A
1211	(-40)	1202	(-37)	ν(N-N)	~1200					1293	2A + B
					1245	(-23)			2A + D		
					1306	(-22)			A + B + D		
					1361	(-22)			2B + D		
					1457	(-45)			2D		

[a]Frequencies in cm^{-1}; (observed ^{15}N isotope shifts). [b]$\{[(Pr^i_2PCH_2SiMe_2)_2N]Zr(\eta^5\text{-}C_5H_5)\}_2(\mu\text{-}\eta^1\text{:}\eta^1\text{-}N_2)$, (complex **1**). [c]**1** in toluene solution. [d]$\{[(Pr^i_2PCH_2SiMe_2)_2N]ZrCl\}_2(\mu\text{-}\eta^2\text{:}\eta^2\text{-}N_2)$, (complex **2**). [e]**2** in THF solution. [f]$\{[(Pr^i_2PCH_2SiMe_2)_2N]ZrBr\}_2(\mu\text{-}\eta^2\text{:}\eta^2\text{-}^{15}N_2)$; natural abundance ^{14}N data for the dibromo complex of **2** not shown.

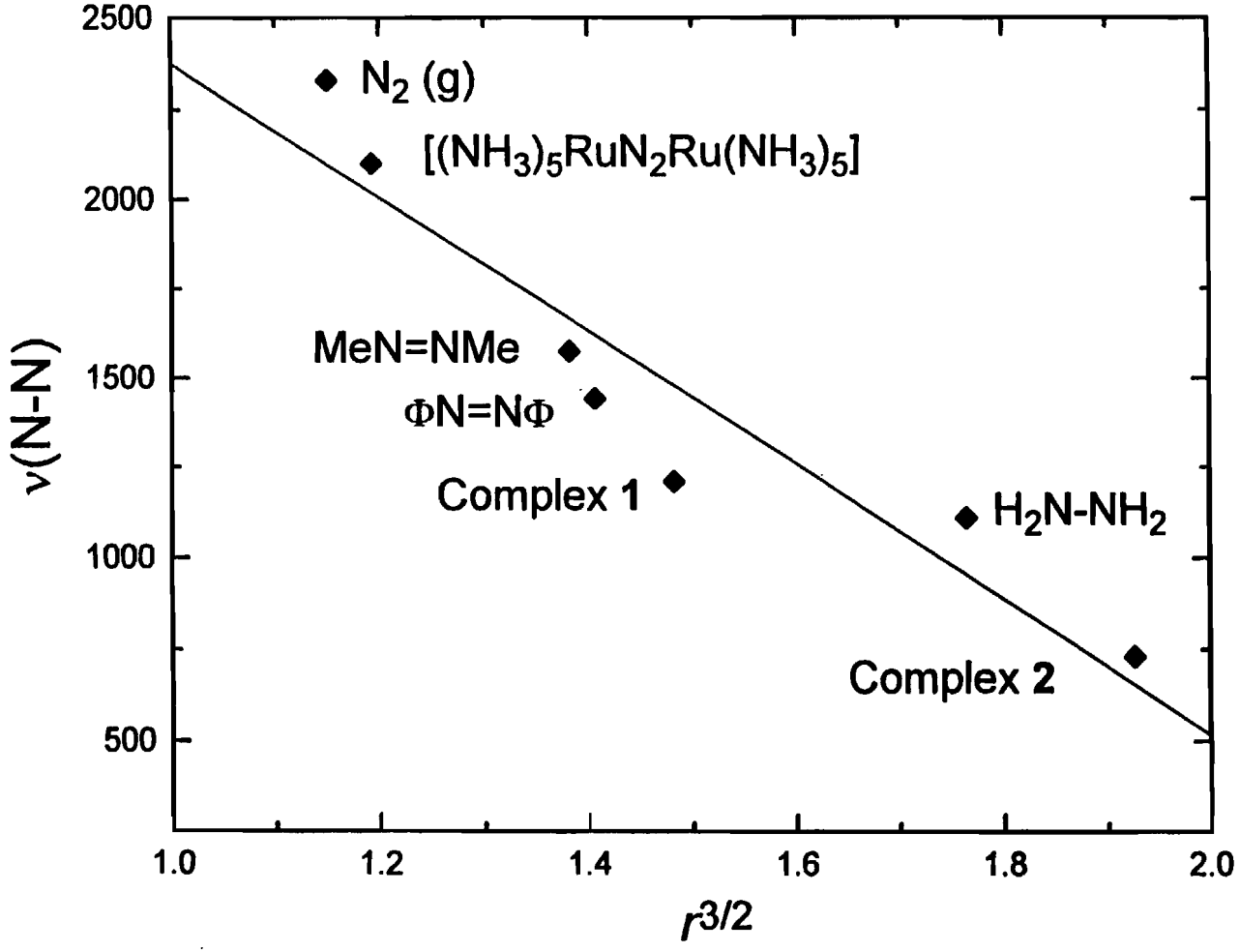

Figure 2-4. N-N stretching frequencies of selected dinitrogen compounds of different bond orders as a power function of their N-N bond lengths.[34]

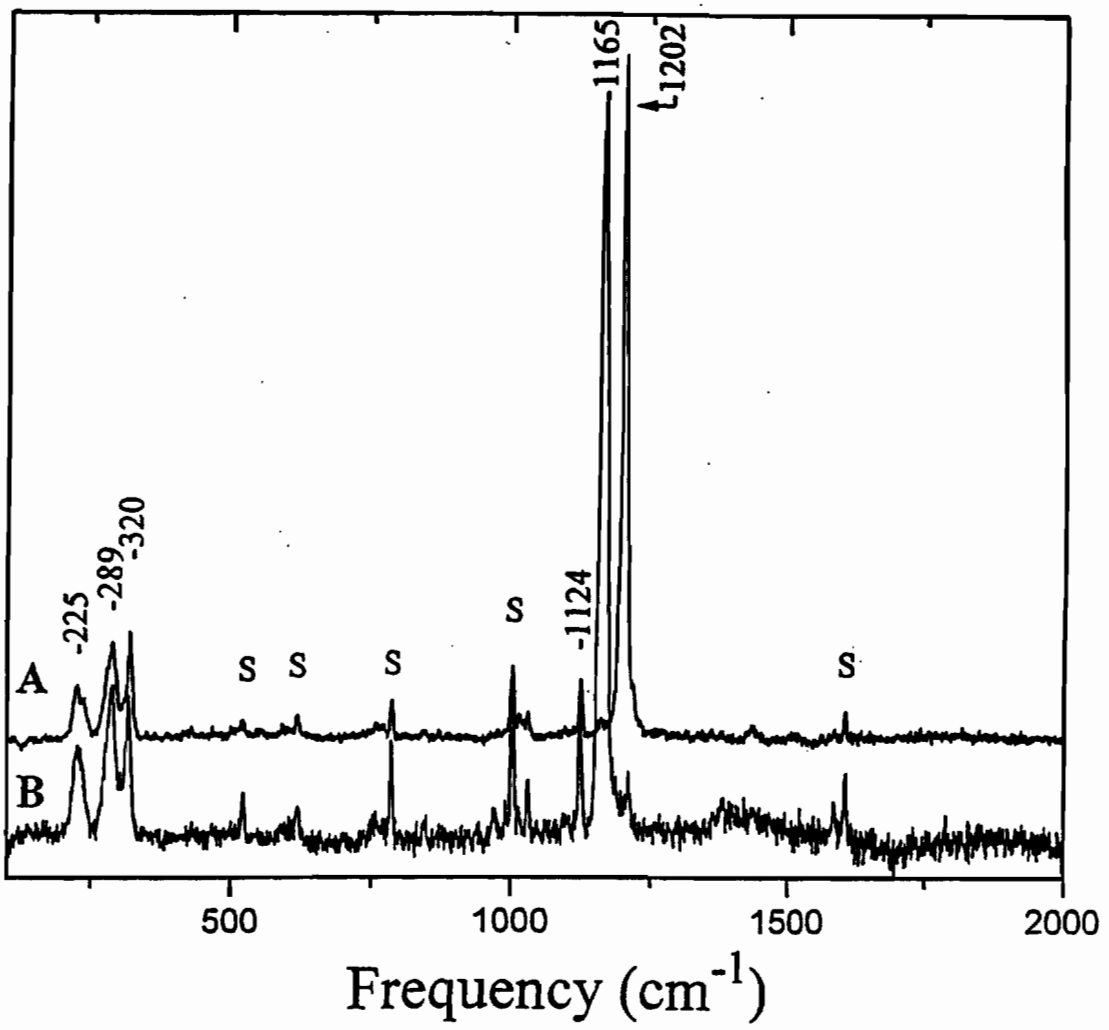

Figure 2-5. Resonance Raman spectra of complex **1** in toluene solution at ~90 K. (A) μ-η^1:η^1-N_2, (B) μ-η^1:η^1-$^{15}N_2$ isotopomer; conditions as in Figure 2-3.

both the solid and solution samples of **1**, the ~1200-cm^{-1} feature is the only band in the RR spectrum with a large ^{15}N-isotope shift. Given that the overall spectral pattern remains the same, these data strongly suggest that complex **1** in solution retains the μ-η^1:η^1-N_2 structure of the crystalline solid.

Vibrational Spectra of $Zr_2(\mu-\eta^2:\eta^2)N_2$ Complexes. The RR spectra of both isotopomers of complex **2** in the solid state and in THF solution are shown in Figures 2-6 and 2-7, respectively. Complex **2** has very different RR spectra from those of complex **1**, and reveal many isotope-sensitive features, unlike those of complex **1**, where only the ~1210-cm^{-1} band shifts with ^{15}N substitution. The RR spectra of complex **2** are dominated by many overtone and combination bands of only a few fundamentals. These spectral properties are undoubtedly related to the side-on coordination of the N_2 ligand, examples of which are still rare.[17]

The two most intense peaks found in the solid-state spectra of complex **2** are found at 317 and 731 cm^{-1} (Fig. 2-6A). In addition, many peaks of lower intensity are observed between 100 and 1500 cm^{-1}. Frequencies and proposed assignments are given in Table 2-1. The peaks at 731, 991, and 1045 cm^{-1} shift to 709, 968, and 1023 cm^{-1}, respectively, upon $^{15}N_2$ substitution (Fig. 2-6B). The 22-cm^{-1} isotope shift observed for the 731-cm^{-1} peak is within 2 cm^{-1} of that expected for a pure ν(N-N) mode at this frequency, suggesting that this feature is one of the totally symmetric A_g modes of the Zr_2N_2 moiety. One may compare this value with ν(N-N) of liquid hydrazine at 1111 cm^{-1}.[37] If vibrational frequencies are used to estimate the bond order (and the N-N bond length, as in Fig. 2-4), and, further, if the 731-cm^{-1} peak represents the principal ν(N-N) stretching mode, then the N-N bond order of complex **2** is *significantly lower* than that in hydrazine, which is assumed to have an N-N bond order of 1. This surprisingly low bond order is consistent with the very long and unique N-N bond of 1.548 Å observed in the crystal structure.[21,29]

The other isotope-sensitive peaks of **2** (Fig. 2-6 and Table 2-1) are assigned as follows: The 991-cm^{-1} peak, which has an isotope shift of 23 cm^{-1} in the $^{15}N_2$-enriched sample, is a combination of the 258- and 731-cm^{-1} bands. This

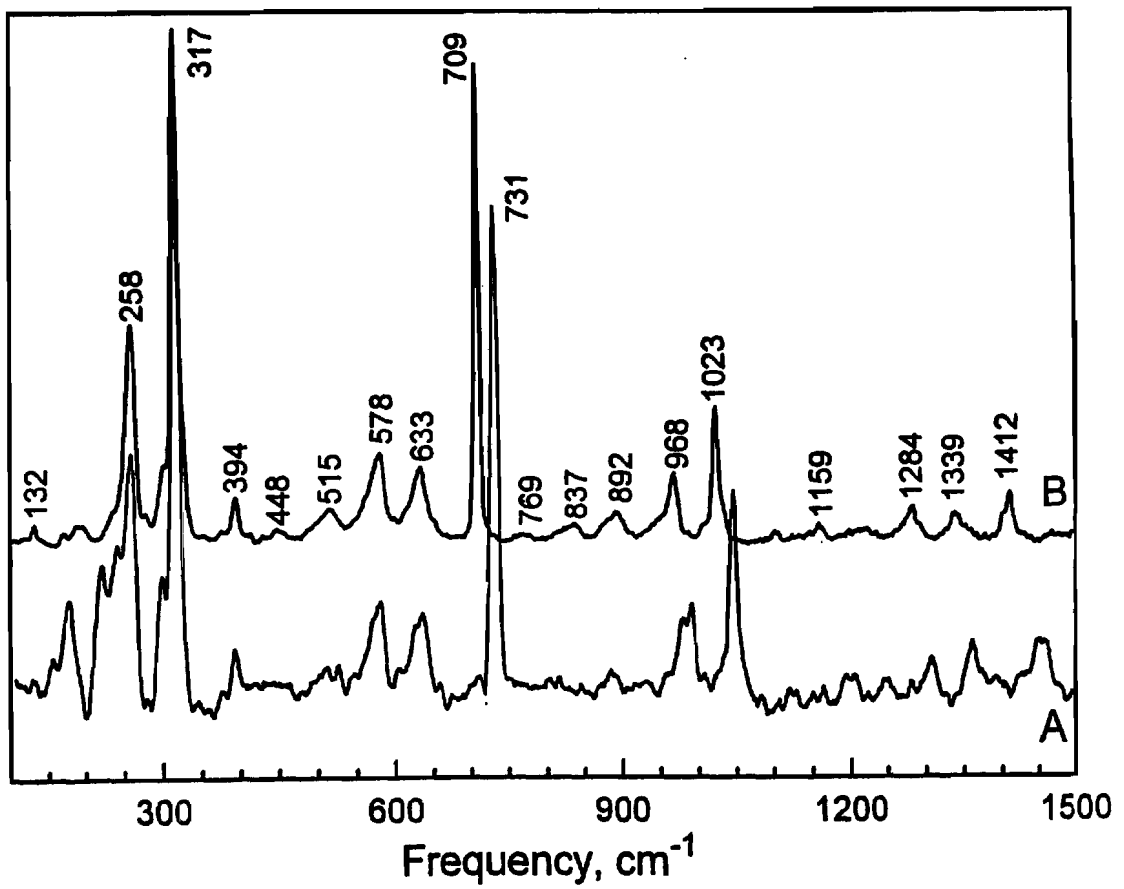

Figure 2-6. Resonance Raman spectra of complex **2** in the solid state at ~90 K. (A) μ-η^2:η^2-N_2, (B), μ-η^2:η^2-$^{15}N_2$ isotopomer. Each trace is a sum of 9 consecutive scans each recorded at 1 cm^{-1}/s using 20 mW of 647.1-nm laser excitation. [The group of three bands at ~170, 220, and 240 cm^{-1} (trace A) appeared with variable intensities in repeat experiments, although no changes were noted in the remaining spectral peaks; these features are, therefore, attributed to decomposition products].

assignment is supported by the fact that the 731-cm^{-1} band shifts 22 cm^{-1} in the $^{15}N_2$-enriched sample but the 258-cm^{-1} band is isotope insensitive. Similarly, the peak at 1045 cm^{-1} is assigned as the combination of the 317- and 731-cm^{-1} peaks based on its observed 23-cm^{-1} shift. In addition, two other isotope-sensitive bands at 1306 and 1361 cm^{-1} that shift by -22 cm^{-1} to 1284 and 1339 cm^{-1}, respectively, are assigned as further combinations of the frequencies at 317 + 991 cm^{-1} and 317 + 1045 cm^{-1}, respectively. The band at 1457 cm^{-1} is assigned as the first overtone of the 731-cm^{-1} ν(N-N) mode. This identification is supported by its large (~45 cm^{-1}) isotope shift that is twice that observed for the 731- cm^{-1} fundamental. Many of the remaining peaks are also simple combination and overtone bands. For instance, the 579-cm^{-1} band is a combination of the 258- and 317-cm^{-1} modes and the 633-cm^{-1} band is the first overtone of the 317-cm^{-1} signal. Also, the 515-cm^{-1} peak is assigned as the first overtone of the 258-cm^{-1} band based on its isotope insensitivity. A nearly complete set of assignments for the frequencies of the solid of complex **2** in the 150-1500-cm^{-1} range that is consistent with the observed isotope shifts is given in Table 2-1.

Complex 2 in Solution. At first glance, the RR spectra of complex **2** in solution appear quite different from those in the solid state; however, these dilute solution spectra are dominated by the strong THF band at ~914 cm^{-1}.[36] The 731-cm^{-1} peak of complex **2** in the solid is split into a pair of signals at 745 and 733 cm^{-1} in THF solution (Fig. 2-7A). These shift to 719 and 709 cm^{-1}, respectively, in the $^{15}N_2$ isotopomer (Fig. 2-7B). Both isotope shifts are within 1 cm^{-1} of the predicted value for a pure ν(N-N) vibrational mode at this frequency and are identical in magnitude to that observed for the 731-cm^{-1} peak of complex **2** in the solid state. Similarly, the 317-cm^{-1} feature in the spectrum of the solid of **2** is also split into a pair of peaks at 331 and 321 cm^{-1}, respectively, in the RR spectrum of the solution sample. These are seen to shift -4 and -3 cm^{-1}, respectively, in the ^{15}N isotopomer, unlike the relatively insensitive low-frequency bands of the solid sample. Two poorly resolved, weak peaks are also apparent at 1002 and 1074 cm^{-1} (Fig. 2-7A). The intense peak at 262 cm^{-1} in the solution sample shifts -2

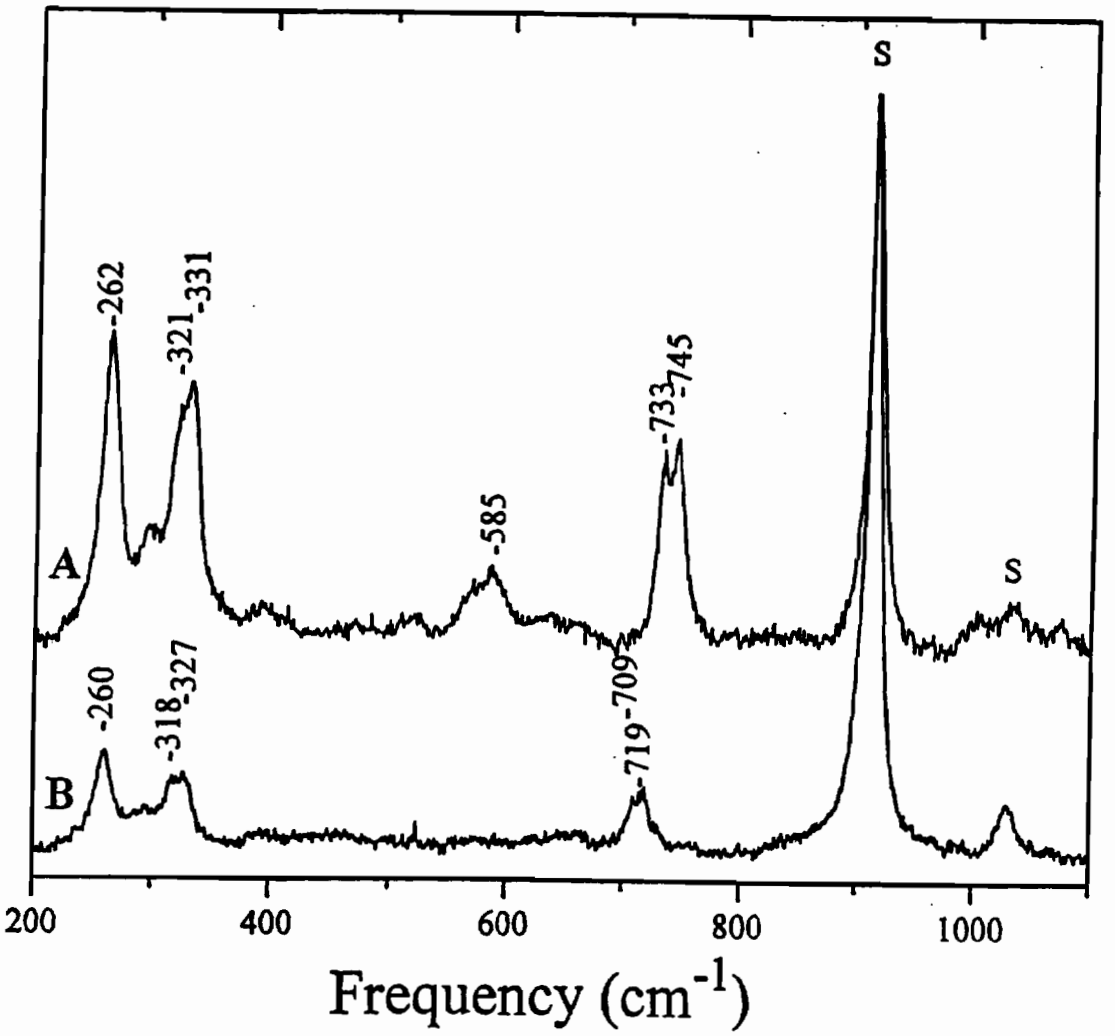

Figure 2-7. Resonance Raman spectra of complex **2** in THF solution at ~90 K. (A) μ-η^2:η^2-N_2, (B), μ-η^2:η^2-$^{15}N_2$ isotopomer. Each trace is a sum of 5 consecutive scans each recorded at 1 cm^{-1}/s using 40 mW of 647.1-nm laser excitation.

cm^{-1} in the isotopomer, however, the apparent combination band of weak-to-medium intensity at ~585 cm^{-1} is absent in the spectrum of the $^{15}N_2$ isotopomer, and may be attributed to the low concentration in the isotopically enriched sample.

Polarization studies of the $^{15}N_2$ isotopomer in solution show that the 719/709-cm^{-1} pair is polarized ($\rho = 0.32$), further supporting the suggestion that this is one of the totally symmetric A_g modes. The 260-cm^{-1} peak and the 318/327-cm^{-1} pair also appear to be polarized ($\rho = 0.35$ and 0.40, respectively). The lower depolarization ratio of the 260-cm^{-1} peak suggests that this may be the second A_g mode of the Zr_2N_2 cluster; however, we cannot rule out the possibility that the 318/327-cm^{-1} pair may also share some A_g character. Even without complete assignments of these bands at this time, the two strong peaks in the low-frequency region, together with a strong isotope-sensitive peak in the ~735-cm^{-1} region, are very similar to corresponding peaks in the solid-state spectrum (Fig. 2-6) indicating that the side-on geometry of the bridging N_2 ligand is preserved in THF solution.

Vibrational Spectra of $Zr_2(\mu\text{-}\eta^2\text{:}\eta^2\text{-}^{15}N_2)$ Complexes with Mixed Halogen Ligands. The crystal structure of complex **2** indicates that the molecule possesses a center of symmetry.[21] For centrosymmetric molecules, only vibrational modes of *g* symmetry are spectroscopically allowed in the Raman effect.[38] Therefore, RR experiments were conducted on samples of complex **2** containing both Cl^- and Br^- ligands to determine if the loss of the center of symmetry would cause any new fundamental modes to appear in the spectra.

The resonance Raman spectra of the dichloro complex, $\{[(Pr^i_2PCH_2SiMe_2)_2N]ZrCl\}_2(\mu\text{-}\eta^2\text{:}\eta^2\text{-}^{15}N_2)$, the mixed bromochloro complex, $\{[(Pr^i_2PCH_2SiMe_2)_2N]Zr\}_2ClBr(\mu\text{-}\eta^2\text{:}\eta^2\text{-}^{15}N_2)$, and the dibromo complex, $\{[(Pr^i_2PCH_2SiMe_2)_2N]ZrBr\}_2(\mu\text{-}\eta^2\text{:}\eta^2\text{-}^{15}N_2)$, are shown in Figure 2-8. NMR spectra of the bromochloro sample indicate that it is a 1:2:1 mixture of the dichloro, the bromochloro, and the dibromo species, respectively. Comparison of the RR spectra of the three halogenated forms of complex **2** shows that the peaks

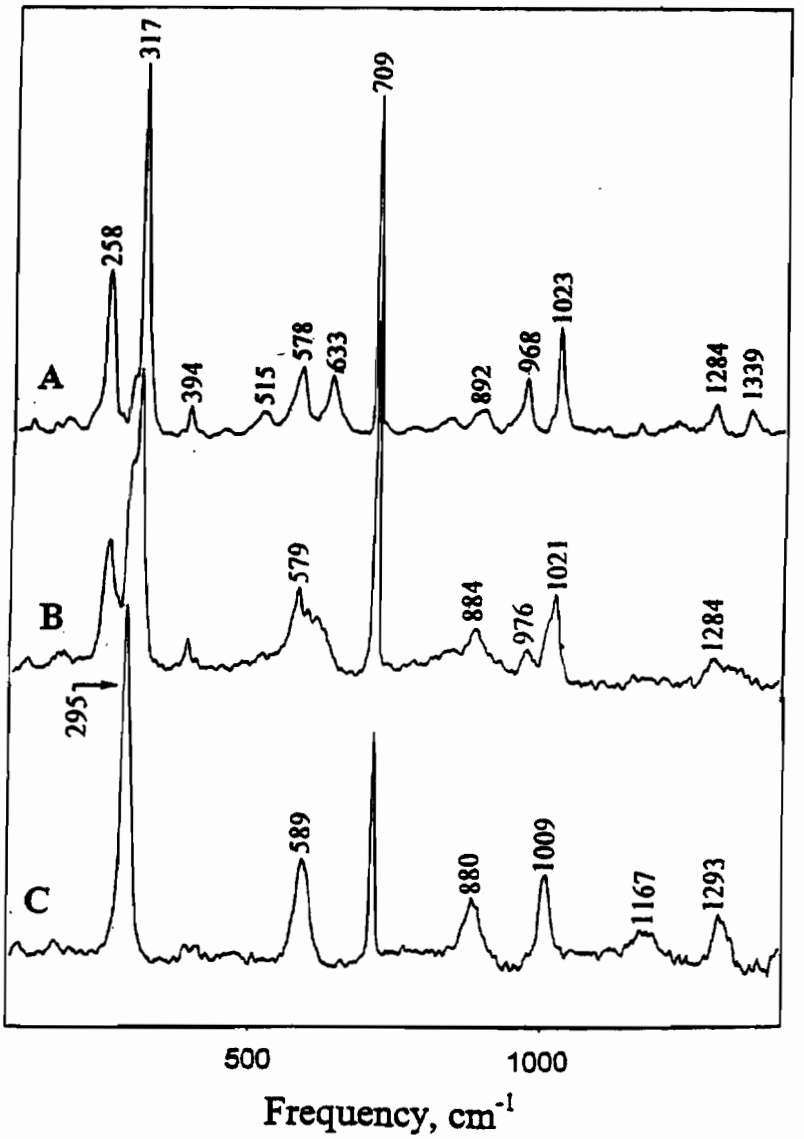

Figure 2-8. Resonance Raman spectra of derivatives of complex **2** with different halogen ligands in the solid state at ~90 K; in each case, only the spectra of the $^{15}N_2$ isotopomers are shown. (A) the parent compound, $\{[(Pr^i_2PCH_2SiMe_2)_2N]ZrCl\}_2(\mu\text{-}\eta^2\text{:}\eta^2\text{-}^{15}N_2)$, as in Fig. 2-6B. (B) $\{[(Pr^i_2PCH_2SiMe_2)_2N]Zr\}_2BrCl(\mu\text{-}\eta^2\text{:}\eta^2\text{-}^{15}N_2)$, a 1:2:1 mixture of the dichloro-, the bromochloro-, and the dibromo- complexes, respectively; and (C) $\{[(Pr^i_2PCH_2SiMe_2)_2N]ZrBr\}_2(\mu\text{-}\eta^2\text{:}\eta^2\text{-}^{15}N_2)$; spectral conditions as in Figure 2-6.

at 258 and 316 cm^{-1} (Fig. 2-8A) begin to merge in the mixed halogenated sample (Fig. 2-8B) and, in the fully brominated sample, only a single peak remains at 295 cm^{-1} (Fig. 2-8C). We had expected that replacement of Cl^- by Br^- would cause a new peak to develop at <200 cm^{-1} corresponding to ν(Zr-Br); however, no new peaks could be observed between 50 and 200 cm^{-1} in the RR spectrum of the dibromo complex of **2** (data not shown). Similarly, the 512-, 580-, and 635-cm^{-1} peaks in Figure 2-8A converged to a single peak at 589 cm^{-1} in Figure 2-8C. In addition, new peaks were found at 880, 1009, 1167, and 1293 cm^{-1} (Fig. 2-8C).

Clearly, the peaks observed at 589, 880, and 1167 cm^{-1} for the dibromo complex (Fig. 2-8C) represent the first, second, and third overtone, respectively, of the fundamental mode at 295 cm^{-1}. Furthermore, the 1293-cm^{-1} peak is a combination band representing the sum of the fundamental mode at 709 cm^{-1} and the first overtone band at 589 cm^{-1}. The 1009-cm^{-1} peak is assigned as the combination of fundamentals at 710 and 295 cm^{-1}.

In short, replacement of the Cl^- ligand with Br^- causes some of the overtone and combination bands to disappear in the low and medium frequency region while inducing new bands to appear in the high frequency region. Nevertheless, no new fundamental modes of the Zr_2N_2 moiety become visible upon replacement of Cl^- ligands for Br^- or by reduction of symmetry. Moreover, ignoring the combination and overtone bands, the overall spectral pattern is quite similar among Figures 2-8A, -8B and -8C suggesting that the side-on geometry of the N_2 ligand is preserved in each case.

Conclusions

This work has shown that resonance Raman spectroscopy can be used to clearly identify and distinguish the two modes of bonding for a dinitrogen ligand in dinuclear metal complexes both in the solid and solution states. Zirconium compounds with a bridging N_2 ligand give radically different RR spectra

depending on the geometry of N_2 binding. For complex **1**, a single intense peak is found in the RR spectrum at 1211 cm^{-1} corresponding to the ν(N-N) symmetric stretch that shifts to 1172 cm^{-1} in the $^{15}N_2$-enriched isotopomer. This value corresponds to an N-N bond order between 1 and 2, consistent with the 1.30-Å N-N bond length observed in the crystal structure. Comparison of solution and solid state spectra show excellent correlation of features indicating that the structure of complex **1** as a solid and in toluene solution are nearly identical.

For complex **2**, there is more than one isotope sensitive feature in the RR spectra, complicating the assignment. Nevertheless, there is strong evidence to support the conclusion that the 731-cm^{-1} peak is a totally symmetric mode composed primarily of ν(N-N) character. The other isotope sensitive bands are assigned as the combination of the peaks found at 731, 317 and 258 cm^{-1}. The vibrational assignment of complex **2** in THF solution is further complicated by the splitting of peaks. Nevertheless, the presence of isotope sensitive features below 1111 cm^{-1} imply an N-N bond order of less than 1; a deduction supported by the 1.548 Å N-N bond length observed in the crystal structure. More importantly, the position of the fundamental modes in the solution state spectra are quite similar to the fundamentals in the solid state, providing further evidence that the overall geometry of the Zr_2N_2 moiety is preserved when complex **2** is in solution.

Finally, the effect of replacing Cl^- with Br^- as ligands is to reduce the number of observed combination and overtone bands in the low and medium frequency region while introducing new bands in the high frequency regions of the RR spectrum. However, neither replacing one halogen ligand with another halogen nor elimination of the center of symmetry was sufficient to cause any new normal modes to appear in the RR spectra. The exact site of nitrogen coordination in nitrogenase and the mechanism of the subsequent reduction are still open questions.[7] The unique molybdenum atom of the FeMo cofactor, long suspected to be important in nitrogen binding and activation, appears to be coordinatively saturated, being bound to three sulfur atoms, a histidyl nitrogen, and chelated to two oxygen atoms of homocitrate.[5,6] A recent selenium-EXAFS study shows that

selenols are competent to bind to iron, but not molybdenum.[39] Thus, it is possible that iron atoms provide the site of initial coordination and reduction of N_2.[40] The Zr_2N_2 compounds of the present study show that N_2 bridging between metals may be accompanied by extreme elongation of the N-N bond. In the case of the μ-η^2:η^2 structure, the resulting N-N bond is considerably longer than that in hydrazine.

Addendum

Recently, Laplaza and coworkers synthesized $Mo^{III}(NRAr)_3$, a 3-coordinate molybdenum compound of trigonal planar geometry where R = $C(CD_3)_2CH_3$ and Ar = 3,5-$C_6H_3(CH_3)_2$.[41] When two equivalents of the molybdenum compound react with N_2 in hydrocarbon solvents at -35 °C, a purple intermediate (λ_{max} = 547 nm) forms that is proposed to be an N_2-bridged dimolybdenum complex. Upon warming, the purple complex disappears, resulting in two equivalents of the terminal nitrido complex, $NMo^{VI}(NRAr)_3$, where the bridging N_2 ligand has been reductively cleaved.

Details of the reaction mechanism are of great interest because of their relevance to nitrogen fixation. To learn more about the structure of the purple intermediate and its role in the mechanism of N_2 cleavage, Laplaza and coworkers used RR spectroscopy to determine the properties of the bridging N_2 ligand in a manner analogous to the dizirconium studies presented here.

Resonance Raman spectra of the purple intermediate prepared from $^{14}N_2$ and $^{15}N_2$ were collected in toluene using visible excitation.[42] After digital subtraction of the toluene bands, a single intense peak at 1630 cm^{-1} in the $^{14}N_2$ complex was observed to shift -53 cm^{-1} in the spectrum of the $^{15}N_2$ isotopomer. This peak was assigned to ν(N-N) of the N_2-bridging ligand. Using our linear relationship between ν(N-N) and $r^{3/2}$ reported here, Laplaza and coworkers estimated that the bridging N-N bond distance in the purple complex is 1.23 Å, corresponding to an N-N bond order of ~2 (Fig. 2-4). No overtone or combination bands were reported in the 1300-1700 cm^{-1} range. Given the single

sharp band observed in the RR spectrum and its calculated bond order from ν(N-N), the authors proposed that the purple complex contains a linear Mo-N=N-Mo moiety. This conclusion was confirmed by Mo K-edge EXAFS revealing a very strong band in the Fourier-transformed spectrum at 4.94 Å arising from the linear MoNNMo core.[42] This intermediate is proposed to isomerize to a zig-zag conformation with C_{2h} symmetry in the transition state, which more closely resembles the symmetry of the two terminal nitrido products. Thus, the utility of RR spectroscopy to determine the N_2 binding geometry, bond distance, and bond order in transition metal compounds has been extended to complexes that actually achieve N_2 cleavage.

Although there are now several synthetic N_2-bridged transition metal clusters of known structure that activate dinitrogen, the N_2 binding geometry of the substrate-bound form of nitrogenase has not been reported. The FeMo cofactor of nitrogenase can bind N_2 in several possible orientations to one or more of the metal atoms. The orientation of N_2 when bound to FeMoco will have an important effect on how electron density is distributed between the atoms of the substrate.

Recently, Hoffmann and coworkers, using the atomic coordinates of FeMoco from the *A. vinelandii* nitrogenase crystal structure, performed molecular orbital calculations to determine the N_2-binding orientations that are most amenable to dinitrogen reduction.[8] The authors examined nine different N_2 binding modes, including end-on to Fe4 and Fe5 as well as side-on to Fe3 and Fe7 (displacing sulfide Y, see Fig. 1-2). The results of these studies were that side-on bonding to Fe3 and Fe7 resulted in the largest decrease in N-N overlap populations (1.47 versus 1.73 for free N_2), which facilitate N_2 cleavage, coupled with the largest net increase in negative charge (-0.12 *e*) on each of the N atoms, which promotes protonation. The end-on mode was less favorable due to the significant positive electrical charge that accumulates on each N atom (0.11 and 0.09) despite its decrease in N-N overlap population to 1.61.

However, the discovery of end-on N_2-bridged transition metal clusters that activate N_2 indicate that the end-on geometry deserves reconsideration at least as an early intermediate step in nitrogen fixation. Furthermore, end-on binding does not require the displacement of any of the bridging ligands of FeMoco (to date, no one has reported any evidence of H_2S or disulfide bond formation during nitrogen fixation, which would be required for the side-on bonding mode proposed by Hoffmann and coworkers). One must also acknowledge the possibility of isomerization of the N_2 ligand during reduction, as proposed for the mechanism of N_2 cleavage by the Laplaza compound.[42] Therefore, during the reaction, the orientation of the bound N_2 ligand may change from end-on to side-on or some other binding mode. Thus, the results presented here demonstrate that the binding of N_2 to two transition metal atoms results in significant nitrogen activation in the end-on geometry.

Acknowledgments

This work was supported by a grants from NSERC to M.D.F. and the National Institutes of Health (GM34468 to T.M.L.). Purchase of instrumentation in the Raman spectroscopy laboratory at OGI was made possible, in part, by a Shared Instrumentation Grant from the National Institutes of Health (S10 RR02676). We thank Dr. Jie Sun for helpful comments and insights.

References and Notes

(1) Oregon Graduate Institute of Science & Technology.

(2) University of British Columbia.

(3) Burris, R. H. "Nitrogenases." *J. Biol. Chem.* **1991**, 266, 9339-9342.

(4) (a) Dilworth, M. J.; Glenn, A. R., Eds. *Biology and Biochemistry of Nitrogen Fixation*; Elsevier: New York, NY, 1991. (b) Orme-Johnson, W. H. "Molecular Basis of Biological Nitrogen Fixation." *Annu. Rev. Biophys. Biophys. Chem.* **1985**, *14*, 419-549.(5) (a) Kim, J.; Rees, D. C. "Structural Models for the Metal Centers in the Nitrogenase Molybdenum-Iron Protein." *Science* **1992**, *257*, 1677-1681. (b) Chan, M. K.; Kim, J.; Rees, D. C. "The Nitrogenase FeMo-Cofactor and P-Cluster Pair: 2.2-Å Resolution Structures." *Science* **1993**, *260*, 792-794.

(6) (a) Kim, J.; Woo, D.; Rees, D. C. "X-ray Crystal Structure of the Nitrogenase Molybdenum-Iron Protein from *Clostridium pasteurianum* at 3.0-Å Resolution." *Biochemistry* **1993**, *32*, 7104-7115. (b) Bolin, J. T.; Ronco, A. E.; Morgan, T. V.; Mortensen, L. E.; Xuong, N.-H. "The Unusual Metal Clusters of Nitrogenase: Structural Features Revealed by X-ray Anomalous Diffraction Studies of the MoFe Protein from *Clostridium pasteurianum*." *Proc. Natl. Acad. Sci. U.S.A.* **1993**, *90*, 1078-1082.

(7) Orme-Johnson, W. H. "Nitrogenase Structure: Where to Now?" *Science* **1992**, *257*, 1639-1640.

(8) Deng, H.; Hoffmann, R. "How N_2 Might Be Activated by the FeMo-Cofactor in Nitrogenase." *Angew. Chem. Intl. Ed. Engl.* **1993**, *32*, 1062-1065.

(9) Coucouvanis, D. "Use of Preassembled Fe/S and Fe/Mo/S Clusters in the Stepwise Synthesis of Potential Analogues for the Fe/Mo/S Site in Nitrogenase." *Acc. Chem. Res.* **1991**, *24*, 1-8.

(10) Bose, K. S.; Chmielewski, S. A.; Eldredge, P. A.; Sinn, E.; Averill, B. A. "New Mo-Fe-S Clusters via Oxidative Decarbonylation Reactions: The$[MoFe_3S_6(CO)_6L_3]^{n-}$ (L = PEt_3, n = 0; L= I, n = 2) Capped Cubanes." *J. Am. Chem. Soc.* **1989**, *111*, 8953-8954.

(11) Holm, R. H.; Simon, E. D. "Molybdenum/Tungsten-Iron-Sulfur Chemistry: Current Status and Relevance to the Native Cluster of Nitrogenase;" in *Molybdenum Enzymes*; Spiro, T. G., Ed.; Wiley-Interscience: New York, 1985, Chapter 1.

(12) Allen, A. D.; Senoff, C. V. "Nitrogenpentammineruthenium(II) Complexes." *J. Chem. Soc. Chem. Commun.* **1965**, 621-622.

(13) (a) Sanner, R. D.; Duggan, M.; McKenzie, T. C.; Marsh, R. E.; Bercaw, J. E. "Structure and Magnetism of μ-Dinitrogen-bis(bis(pentamethylcyclopentadienyl)-titanium(II)), $\{(\eta^5\text{-}C_5(CH_3)_5)_2Ti\}_2N_2$." *J. Am. Chem. Soc.* **1976**, *98*, 8358-8365.

(b) Sanner, R. D.; Manriquez, J. M.; Marsh, R. E.; Bercaw, J. E. "Structure of μ-Dinitrogen-Bis(Bis(pentamethylcyclopentadienyl)-dinitrogenzirconium(II)), $\{(\eta^5\text{-}C_5(CH_3)_5)_2ZrN_2\}_2N_2$." *J. Am. Chem. Soc.* **1976**, *98*, 8351-8357.

(14) Dilworth, J. R.; Richards, R. L. "Electronation and Protonation of Coordinated Dinitrogen;" in *Comprehensive Organometallic Chemistry*; Wilkinson, G., Stone, F. G. A., Abel, E. W., Eds.; Pergamon Press: Oxford, 1982, Vol. 8, p. 1073.

(15) Henderson, R. A.; Leigh, G. J.; Pickett, C. J. "Mechanism of the Base-Catalyzed Substitution of Halide for Methoxide in the Reactions of *trans*$([W(NH)X(Ph_2PCH_2CH_2PPh_2)_2]^+$ (X = Cl, Br, or I)." *Adv. Inorg. Chem. Radiochem.* **1983**, *27*, 197.

(16) Pelikán, P.; Boca, R. "Geometric and Electronic Factors of Dinitrogen Activation on Transition Metal Complexes." *Coord. Chem. Rev.* **1984**, *55*, 55-112.

(17) Evans, W. J.; Ulibarri, T. A.; Ziller. J. W. "Isolation and X-ray Crystal Structure of the First Dinitrogen Complex of an *f*-Element Metal, $[(C_5Me_5)_2Sm]_2N_2$." *J. Am. Chem. Soc.* **1988**, *110*, 6877-6879. This paper reports the first example of a $\mu\text{-}\eta^2\text{:}\eta^2\text{-}N_2$ structure in a dinuclear metal (samarium) complex. The N-N bond length was reported as 1.088 (12) Å, a value similar to that of N_2 (g).

(18) (a) Leigh, G. J. "Chemical Nitrogen Fixation and Transition Metal Dinitrogen Complexes." *Sci. Prog. (Oxford)* **1989**, *291*, 389-412. (b) Leigh, G. J. "Protonation of Coordinated Dinitrogen." *Acc. Chem. Res.* **1992**, 25, 177-181.

(19) Henderson, R. A. "The Chemistry of Niobium and Tantalum Dithiocarbamato-Complexes. 6. The Kinetics and Mechanism of the Hydrazine-Forming Reactions Between $[\{Ta(S_2CNEt_2)_3\}_2(\mu\text{-}N_2)]$ and Hydrogen Bromide: Cleavage of the Binuclear Unit." *Transition Met. Chem.*, **1990**, *15*, 330-337.

(20) Wilkinson, P. G.; Houk, N. B. "Emission Spectra of Nitrogen in the Vacuum Ultraviolet." *J. Chem. Phys.* **1956**, *24*, 528-534.

(21) Fryzuk, M. D.; Haddad, T. S.; Mylvaganam, M.; McConville, D. H.; Rettig, S. J ."End-On Versus Side-On Bonding of Dinitrogen to Dinuclear Early Transition-Metal Complexes." *J. Am. Chem. Soc.* **1993**, *115*, 2782-2792.

(22) Manriquez, J. M.; Sanner, R. D.; Marsh, R. E.; Bercaw, J. E. "Reduction of Molecular Nitrogen to Hydrazine. Structure of a Dinitrogen Complex of Bis(pentamethylcyclopentadienyl)zirconium(II) and a Nitrogen-15 labeling Study of its Reaction with Hydrogen Chloride." *J. Am. Chem. Soc.* **1976**, *98*, 3042-3044.

(23) Schrock, R. R.; Fellmann, J. D. "High-Yield Synthesis and Crystal Structure of 1,5,9,13-Tetraazacyclhexadecane ([16]aneN4)." *J. Am. Chem. Soc.* **1978**, *100*, 3359-3370.

(24) Messerle, L. W.; Jennische, P.; Schrock, R. R.; Stucky, G. D. "Preparation of Monocyclopentadienyl Benzylidene Complexes of Tantalum and the Crystal Structure of $Ta(\eta^5\text{-}C_5Me_5)(CHPh)(CH_2Ph)_2$." *J. Am. Chem. Soc.* **1980**, *102*, 6744-6752.

(25) Campbell, J. R.; Clark, R. J. H.; Stead, M. J. "Structure and Bonding in Linear-bridged Species: Electronic, Raman, and Resonance Raman Spectra of the Trinuclear Dinitrogen-bridged Complex $[\{Cl(PMe_2Ph)_4Re(N_2)\}_2MoCl_4]$." *J. Chem. Soc. Dalton Trans.* **1983**, 2005-2010.

(26) Edema, J. J.; Meetsma, A.; Gambarotta, S. "Divalent Vanadium and Dinitrogen Fixation: the Preparation and X-ray Structure of $(\mu\text{-}N_2)\{[o\text{-}Me_2NCH_2)C_6H_4]_2V(Py)\}_2(THF)_2$." *J. Am. Chem. Soc.* **1989**, *111*, 6878-6880.

(27) (a) O'Regan, M. B.; Liu, A. H.; Finch, W. C.; Schrock, R. R.; Davis, M. W. "A Study of the High Oxidation State Complexes of the Type $[W(\eta^5\text{-}C_5Me_5)Me_2X]_2(\mu\text{-}N_2)$, Including Structures of $[W(\eta^5\text{-}C_5Me_5)Me_2(OC_6F_5)]_2(\mu\text{-}N_2)$ and $[W(\eta^5\text{-}C_5Me_5)Me_2(S\text{-}2,4,6\text{-}C_6H_2Me_3)]_2(\mu\text{-}N_2)$." *J. Am. Chem. Soc.* **1990**, *112*, 4331. (b) Schrock, R. R.; Kolodziej, R. M.; Liu, A. H.; Davis, M. W.; Vale, M. G. "Preparation and Characterization of Two High Oxidation State Molybdenum Dinitrogen Complexes: $[MoCp^*Me_3]_2(\mu\text{-}N_2)$ and $[MoCp^*Me_3](\mu\text{-}N_2)[WCp'Me_3]$." *J. Am. Chem. Soc.* **1990**, *112*, 4338-4345.

(28) Duchateau, R.; Gambarotta, S.; Beydoun, N.; Benison, C. "Side-On versus End-On Coordination of Dinitrogen to Titatnium(II) and Mixed-Valence Titanium(I)/Titanium(II) Amido Complexes." *J. Am. Chem. Soc.* **1991**, *113*, 8986-8988.

(29) Fryzuk, M. D.; Haddad, T. S.; Rettig, S. J. "Reduction of Dinitrogen by a Zirconium Phosphine Complex to Form a Side-On-Bridging N_2 Ligand. Crystal Structure of $\{[(Pr^i_2PCH_2SiMe_2)_2N]ZrCl\}_2(\mu\text{-}\eta^2\text{:}\eta^2\text{-}N_2)$." *J. Am. Chem. Soc.* **1990**, *112*, 8185-8186.

(30) Kachapina, L. M.; Borshch, V. N.; Kichigina, G. A.; Makhaev, V. D.; Borisov, A. P. "Resonance Raman Spectra and Nature of the 2.3-2.5 eV Electronic Transitions in Some Dinuclear Dinitrogen-Bridged Complexes. $Cl(PMe_2Ph)_2ReN_2A$, A = $TiCl_4$ (THF), $MoCl_4$ (OCH_3), $CrCl_3$ $(THF)_2$." *Nouv. J. Chim.* **1982**, *6*, 253-258.

(31) All the samples tested are extremely sensitive to the presence of oxygen and decompose rapidly upon exposure to air.

(32) Loehr, T. M.; Sanders-Loehr, J. "Techniques for Obtaining Resonance Raman Spectra of Metalloproteins." *Methods Enzymol.* **1993**, *226*, 431-470.

(33) Rasetti, F. "Raman Effect of Diatomic Gases." *Proc. Natl. Acad. Sci. U.S.A.* **1929**, *15*, 234-237.

(34) Given that the frequency $\nu = \frac{1}{2\pi}\sqrt{\frac{k}{\mu}}$, where k is the force constant and μ is the reduced mass, and the Badger's rule relationship[35] $r_e \propto k^{-1/3}$, where r_e is the equilibrium bond length, the frequency would then be proportional to $r^{3/2}$.

(35) Herschbach, D. R.; Laurie, V. W. "Anharmonic Potential Constants, and Their Dependence upon Bond Length." *J. Chem. Phys.* **1961**, *35*, 458-463.

(36) Strommen, D. P.; Nakamoto, K. *Laboratory Raman Spectroscopy*; Wiley: New York, 1984.

(37) Durig, J. G.; Bush, S. F.; Mercer, E. E. "Vibrational Spectrum of Hydrazine-d_4 and a Raman Study of Hydrogen Bonding in Hydrazine." *J. Chem. Phys.* **1966**, *44*, 4238-4247.

(38) Harris, D. C.; Bertolucci, M. D. *Symmetry and Spectroscopy*; Oxford: New York, 1978.

(39) Conradson, S. D.; Burgess, B. K.; Newton, W. E.; Di Cicco, A.; Filipponi, A.; Wu, Z. Y.; Natoli, C. R.; Hedman, B.; Hodgson, K. O. "Selenol Binds to Iron in Nitrogenase Iron-Molybdenum Cofactor: An Extended X-ray Absorption Fine Structure Study." *Proc. Natl. Acad. Sci. U.S.A.* **1994**, *91*, 1290-1293.

(40) Leigh, G. J.; Jimenez-Tenorio, M. "Exchange of Dinitrogen between Iron and Molybdenum Centers and the Reduction of Dinitrogen Bound to Iron: Implications for the Chemistry of Nitrogenases." *J. Am. Chem. Soc.* **1991**, *113*, 5862-5863.

(41) Laplaza, C. E.; Cummins, C. C. "Dinitrogen Cleavage by a Three-Coordinate Molybdenum(III) Complex." *Science* **1995**, *268*, 861-863.

(42) Laplaza, C. E.; Johnson, M. J.; Peters, J. C.; Odom, A. L.; Kim, E.; Cummins, C. C.; George, G. N.; Pickering, I. J. "Dinitrogen Cleavage by Three-Coordinate Molybdenum(III) Complexes: Mechanistic and Structural Data." *J. Am. Chem. Soc.* **1996**, *118*, 8623-8638.

Chapter 3

A Mixed Valent Dinuclear Iron Compound with Unusual Asymmetry. RR Evidence for a Trapped Valence State.[1]

Abstract

A novel μ-oxo diiron compound, $[Fe_2O(Ph_3CCOO)_2(Me_3tacn)_2]X$ (Me_3tacn = trimethyltriazacyclononane, X = BPh_4^- or $CF_3SO_3^-$) was synthesized in a mixed valence Fe^{2+}/Fe^{3+} state. The X-ray structure ($CF_3SO_3^-$ salt) reveals two distinct Fe-oxo bond lengths of 1.800 and 1.847 Å. Thus, the unpaired electron appears to be localized on a single iron, resulting in a class II trapped valence complex. This compound displays a ligand-to-metal charge transfer band (λ_{max} = 385 nm, ε = 2100 M^{-1} cm^{-1}) and an intervalence transfer band (λ_{max} = 685 nm, ε = 435 M^{-1} cm^{-1}) in the electronic absorption spectrum. The resonance Raman (RR) spectrum of this compound reveals two peaks at 702 and 1404 cm^{-1} assigned to the asymmetric stretch of the Fe-O-Fe moiety and its first overtone, respectively, that display resonance enhancement that closely tracks the recorded absorption spectrum. These assignments are based on their ^{18}O isotope shifts of -30 and -60 cm^{-1}, respectively, and the excellent correlation of the ν_{as} frequency with the 117.8° Fe-O-Fe bond angle observed in the crystal structure. However, no peak could be found in the RR spectrum that can be assigned to ν_s(Fe-O-Fe). Although oxo bridged diferric proteins and model compounds with symmetric ligand arrangements usually have greater intensity associated with ν_s than ν_{as}, large I_{as}/I_s ratios have been observed for model compounds with asymmetric iron environments. The present compound may serve as a structural model for trapped valence intermediates in diiron enzymes.

Introduction

Oxo- and hydroxo-bridged dinuclear iron clusters have been identified in many enzymes. These cofactors catalyze diverse reactions, such as alkane hydroxylation,[2] fatty acid desaturation,[3] and ribonucleotide reduction.[4] The common feature of these enzymatic reactions is their dependence on O_2 activation, either for the direct insertion of oxygen into the substrate or for the generation of a powerful electron acceptor.

Surprisingly, the amino acid ligands to the Fe-O-Fe cofactor are remarkably similar from one enzyme to another,[3] suggesting that the polypeptide surroundings must regulate the diverse chemistry. Although high resolution crystal structures are available for several diiron enzymes in the diferric and diferrous states,[5] trapping these enzymes in other valence states is not trivial. Consequently, over one hundred diiron model compounds have been synthesized and structurally characterized.[6,7] These models are used to mimic the structure of diiron enzymes in the immediate vicinity of the Fe-O-Fe cofactor. The chemical and spectroscopic properties of the model can be compared to the analogous properties in the enzyme to determine structural and functional similarities. The ligands and oxidation state of the model can also be modified to examine how changes in the structure affect the chemistry and the spectroscopy.

Recently, Karl Hagen and coworkers synthesized two novel diiron model compounds and determined their structure using X-ray crystallography.[8] $[Fe_2OH(Ph_3CCOO)_2(Me_3tacn)_2](X)$ (1) is a μ-hydroxo, di-μ-carboxylato, diferrous compound (Me_3tacn = trimethyltriazacyclononane, $X = CF_3SO_3^-$ or BPh_4^-) with symmetrically arranged capping (Me_3tacn) and bridging (Ph_3CCOO and OH) ligands. The crystal structure of 1 reveals ~2.00 Å Fe-hydroxo bond lengths and a 116.7° Fe-O(H)-Fe bond angle, typical for tribridged diferrous compounds (Fig. 3-1A).[6] Samples of 1 react with O_2 or other oxidants in dry organic solvents, to form $[Fe_2O(Ph_3CCOO)_2(Me_3tacn)_2](X)$ (2) (Fig. 3-1B) containing a μ-oxo rather than a μ-hydroxo ligand (Fig. 3-2). Magnetic susceptibility measurements reveal that compound 2

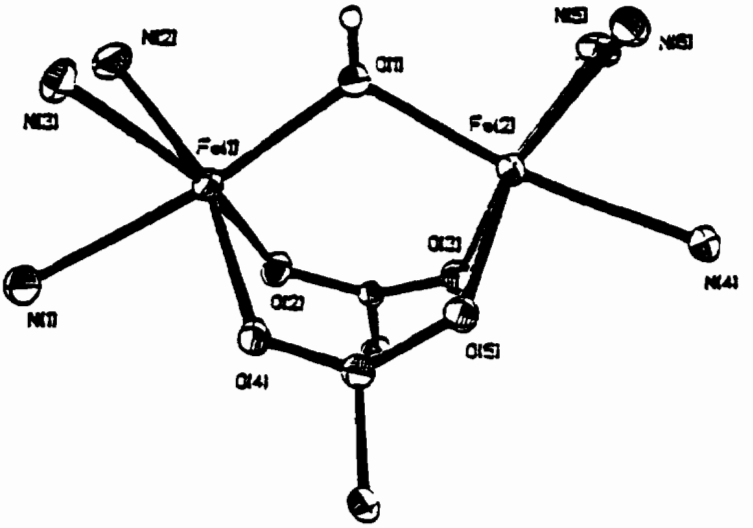

A. Compound 1

Fe(1)-O(1) 2.008 Å

Fe(2)-O(1) 2.002 Å

Fe(1)-O(1)-Fe(2) 116.7°

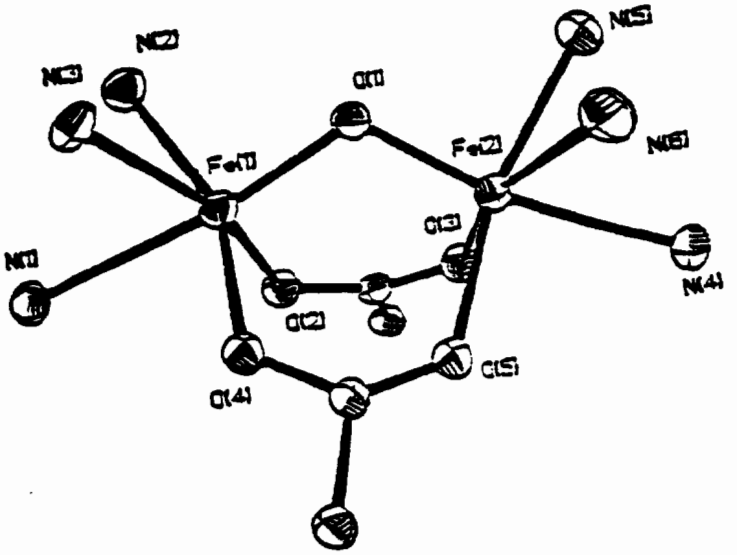

B. Compound 2

Fe(1)-O(1) 1.800 Å

Fe(2)-O(1) 1.847 Å

Fe(1)-O(1)-Fe(2) 117.8°

Figure 3-1. Structure of compound **1** (A) and compound **2** (B) showing the 50% thermal ellipsoids. The carbon atoms on the Me_3tacn ligands and phenyl groups of the O_2CCPh_3 ligands have been omitted for clarity. Selected interatomic distances (Å) and angles (deg) for **1**: Fe1-O1, 2.008; Fe1-O2, 2.110; Fe1-O4, 2.159; Fe1-N1, 2.228; Fe1-N2, 2.274; Fe1-N3, 2.265; Fe2-O1, 2.002; Fe2-O3, 2.160; Fe2-O5, 2.136; Fe2-N4, 2.261; Fe2-N5, 2.256; Fe2-N6, 2.317; Fe1-O1-Fe2, 116.7. Selected interatomic distances (Å) and angles (deg) for **2**: Fe1-O1, 1.800; Fe1-O2, 2.086; Fe1-O4, 2.056; Fe1-N1, 2.311; Fe1-N2, 2.253; Fe1-N3, 2.238; Fe2-O1, 1.847; Fe2-O3, 2.136; Fe2-O5, 2.156; Fe2-N4, 2.315; Fe2-N5, 2.254; Fe2-N6, 2.269; Fe1-O1-Fe2, 117.8.

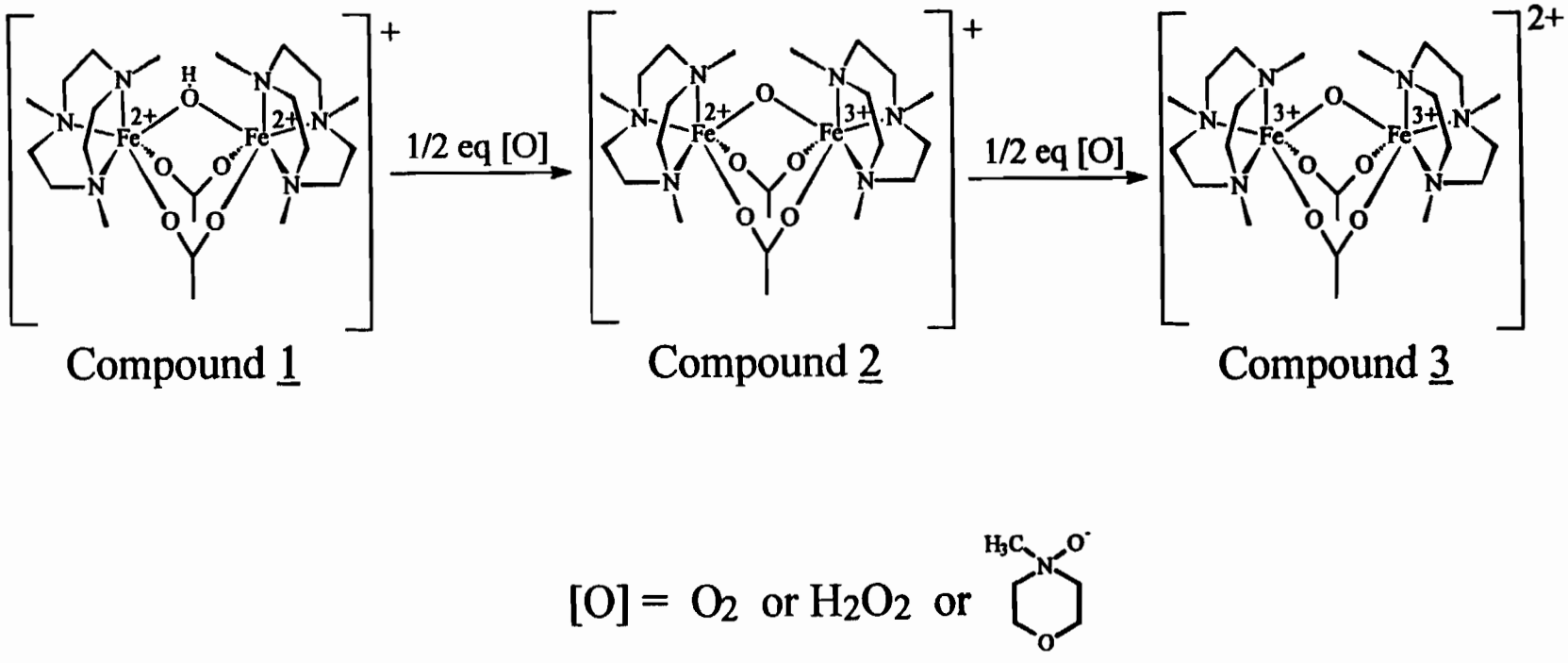

Figure 3-2. Formation of mixed valent **2** and diferric **3** by sequential addition of 0.5 equivalents of 4-methylmorpholine *N*-oxide (forming 4-methylmorpholine + H_2O) or 0.5 equivalents of H_2O_2 (forming $2H_2O$) or 0.5 equivalents of O_2 (forming H_2O_2).

is in an S = ½ ground state, indicative of a mixed valence diiron cluster. More importantly, X-ray crystallography shows that **2** ($CF_3SO_3^-$ salt) displays two distinct Fe-oxo bond lengths of 1.800 and 1.847 Å, indicating that **2** is a class II trapped valence (Fe^{2+}/Fe^{3+}) molecule using the classification scheme of Robin and Day.[9] Although mixed valence hydroxo tribridged and oxo monobridged complexes have been synthesized previously,[10,11] compound **2** is the first example of a stable, *trapped valence, oxo bridged,* diiron compound.

Resonance Raman (RR) spectroscopy has proven particularly useful in the past to characterize μ-oxo bridged diiron sites in proteins, enzymes, and model compounds by its vibrational signature. From group theoretical analysis,[12,13] in the absence of coupling to other vibrational modes, Fe-O-Fe cofactors exhibit 2 non-degenerate vibrational stretching modes: a symmetric stretching mode [ν_s(Fe-O-Fe)] between 360 and 540 cm^{-1}, and an asymmetric stretching mode [ν_{as}(Fe-O-Fe)] between 720 and 870 cm^{-1} (Fig. 3-3). Sanders-Loehr and coworkers have shown that there is an excellent correlation between the observed Fe-O-Fe angle and the frequencies of the symmetric and asymmetric stretching modes.[14] This correlation is in agreement with the predictions of Wing and Callahan.[15] Use of their secular equations in conjunction with vibrational frequencies observed for the ^{16}O and ^{18}O isotopomers provides a means of calculating the Fe-O-Fe angle.

In this work, solid samples of compounds **1** and **2** were prepared with ^{16}O- and ^{18}O-labeled hydroxo and oxo bridging ligands, respectively, and examined using electronic and RR spectroscopy. Specifically, the purpose of these experiments was to compare the RR spectrum of **2** with diferric proteins and synthetic models to look for features that can be used as indicators of the trapped valence state. Although the RR spectra of **1** did not reveal any Fe-O(H)-Fe vibrational modes, the RR spectrum of **2** revealed an intense peak at ~702 and a weaker band at ~1404 cm^{-1} assigned to ν_{as}(Fe-O-Fe) and its first overtone, respectively. However, no peak was observed in the RR spectrum that could be assigned to ν_s(Fe-O-Fe). This is in contrast to most other diiron proteins and models where the symmetric stretch is more intense than the asymmetric stretch. This unusual ratio of I_{as}/I_s for **2** may be unique to the cluster asymmetry generated by the trapped valence state of the

A.

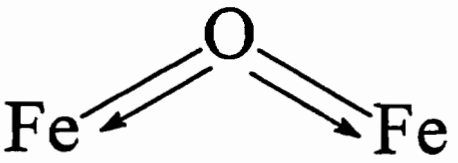

ν_s(Fe-O-Fe)
360-540 cm^{-1} for
180°-120° Fe-O-Fe angle

B.

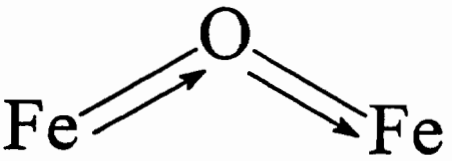

ν_{as}(Fe-O-Fe)
720-870 cm^{-1} for
120°-180° Fe-O-Fe angle

Figure 3-3. Vector diagram of the Fe-O-Fe vibrational stretching modes and their respective frequencies which are a function of the Fe-O-Fe angle and the range observed in proteins and model compounds.[14]

complex, which results in anomalously high resonance enhancement of the asymmetric vibrational modes compared to diferric proteins and model compounds.

Experimental

Solid samples of the μ-hydroxo diferrous (**1**), the μ-oxo trapped valence complexes (**2**), and their μ-oxo diferric analogues (**3**) were prepared by Sonha Payne and Karl Hagen at Emory University by methods described elsewhere.[8] For isotopically labeled samples, compound **1** was prepared in $H_2{}^{16}O$ or $H_2{}^{18}O$, crystallized, dissolved in dry organic solvent (CH_3CN or CH_2Cl_2), reacted with $^{16}O_2$ or $^{18}O_2$ to form **2** or **3** (depending on $[O_2]$), and recrystallized. Alternatively, samples of **2** were prepared from isotopically labeled **1** oxidized by stoichiometric 4-methylmorpholine *N*-oxide in solution and recrystallized. Samples arrived in anaerobically sealed capillaries or ampoules (as powders or crystals, respectively) and were stored in an anaerobic chamber until used. Two sample sets were investigated; one set with $CF_3SO_3^-$, the counteranion used in the determination of the crystal structure, and a second set with BPh_4^-, the counteranion which crystallized more readily. Solution samples of **2** were prepared by adding 30 μl of dry, anaerobic CH_3CN with a syringe to ~5 mg of solid sample in a capillary tube sealed with a rubber septum.

Resonance Raman spectroscopy was performed on a custom-built McPherson 2061/207 Raman spectrophotometer equipped with a 1200 or 600 groove/mm holographic grating, a Princeton Instruments LN1100PB liquid N_2-cooled CCD detector, a Kaiser Optical Systems holographic notch or super-notch filter, and interfaced to Gateway 2000 personal computer; or on a Jarrell-Ash 25-300 Raman spectrophotometer equipped with a Hamamatsu 943-02 photomultiplier tube and interfaced to a Gateway 2000 personal computer. Laser excitation was provided by a Coherent Innova 302 Kr^+ ion laser operating at 413.1, 647.1, or 676.4 nm; a Coherent Innova 90 Ar^+ ion laser operating at 457.9, 488.0 or 514.5 nm; a Liconix 4240NB He/Cd laser operating at 441.7 nm; or by an Ar+ ion pumped Coherent CR-599 dye laser tuned to 574.0 or 618.5 nm. Interfering plasma emissions were removed with an Applied Photophysics prism

monochromator. Spectra were recorded at room temperature using backscattering geometry or, for solution samples of compound **2**, using right-angle scattering at ~278 K with a copper cold finger immersed in a Dewar flask filled with an ice-water mixture. All spectra were calibrated against aspirin or toluene as external standards for peak positions. Typical spectral resolution was 4-6 cm^{-1}. Frequencies of intense features are accurate to ±1 cm^{-1}. All spectra were smoothed and baseline corrected using the GRAMS/386 (Galactic Industries) software package.

Electronic absorption spectra were recorded on a Perkin-Elmer Lambda-9 UV/Vis/NIR spectrophotometer with samples in sealed glass capillaries (1.5-1.8 mm path length) or in a sealed quartz cuvette (4 mm path length).

Results and Discussion

Compound 1. The RR spectra of the μ-^{16}OH- and μ-^{18}OH-labeled isotopomers of compound **1** using 413.1-nm excitation reveal many well-resolved bands (Fig. 3-4). Spectra were also recorded using 457.9- and 514.5-nm excitation on both the $CF_3SO_3^-$ and BPh_4^- salts with very similar results (data not shown). Since this compound is essentially colorless (tan flakes), no excitation wavelength dependence on Raman intensity was expected.

The most intense band in the RR spectra of **1** at ~1002 cm^{-1} is assigned to the aromatic ring breathing mode of the two Ph_3CCOO bridging ligands. This mode is commonly seen in the RR spectra of toluene and other organic compounds containing monosubstituted phenyl groups.[16] The next most intense band at ~1033 cm^{-1} is interpreted as the in-plane C-H deformation mode of the phenyl rings. The intensity of the phenyl modes observed in the spectrum of the $CF_3SO_3^-$ salt are similar to those of the BPh_4^- salt, indicating that these vibrations are from the bridging triphenylacetate groups and not the counteranion. In addition, there are many low intensity peaks throughout the 400-1600 cm^{-1} range. Although these bands have not been assigned with certainty, their lack of significant isotope shifts demonstrates that they are not associated with the Fe-OH-Fe moiety.

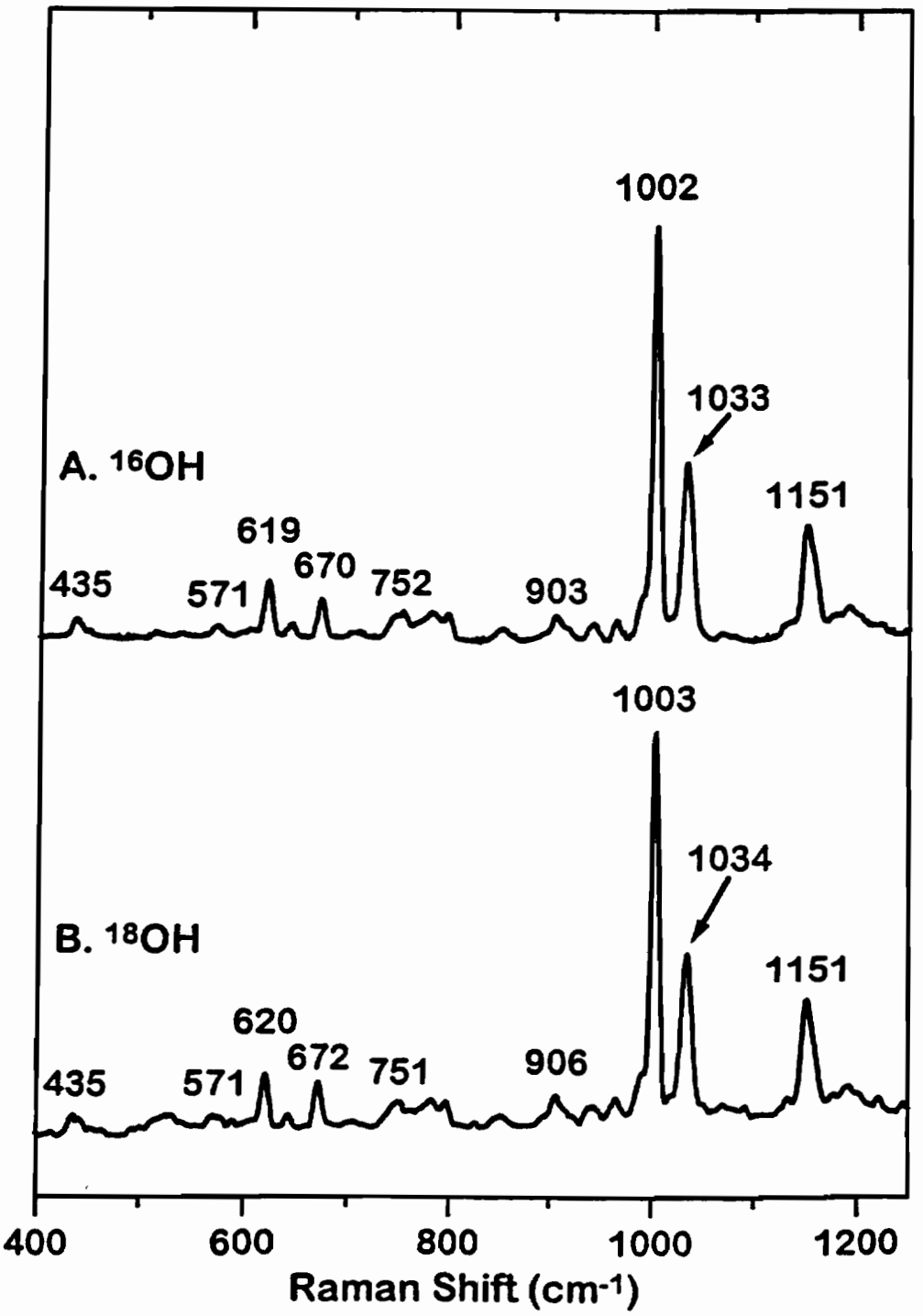

Figure 3-4. Resonance Raman spectra of compound **1** ($CF_3SO_3^-$ salt, crystals) prepared with (A) ^{16}OH and (B) ^{18}OH bridging ligand. The spectra were obtained with excitation at 413.1 nm (25 mW), 298 K, 60 min exposure time, 4 cm^{-1} resolution.

The failure to observe any Fe-OH-Fe vibrational modes is consistent with the small Raman scattering cross-section of ferrous hydroxo bridged clusters.[6,17] However, the spectrum of **1** provides a reference for changes observed in **2** upon oxidation of the diiron cluster. Since the only significant chemical differences between **1** and **2** are the oxidation states of the iron and the protonation of the bridging ligand, identification of the Fe-O-Fe stretching modes should be facile.

Compound 2. **(A)** ***Electronic Absorption Spectrum.*** Unlike the colorless compound **1**, compound **2** is dark green in color. Samples of **2** (BPh_4^- salt) in CH_2Cl_2 demonstrate strong electronic absorption bands at 385 and 685 nm with weaker transitions at 475, 525 and 563 nm (Fig. 3-5). The absorption spectrum of compound **2** is quite similar to those of other mixed valence diiron systems. For instance, hemerythrin (Hr) also forms a trapped valence (Fe^{2+}/Fe^{3+}) state referred to as semi-metHr.[18] Semi-metHr exhibits electronic transitions at 330, 370, 490, and 670 nm (Table 3-1) with the last two being assigned as ligand field bands of the Fe(III) ions.[19]he markedly greater intensity (~5-fold compared to semi-metHr) of the 685-nm absorption band in **2** suggests that this feature may be an intervalence transfer (IT) band. Its full width at half maximum (~3480 cm^{-1}) is similar to that observed for IT bands in other mixed valence diiron compounds.[20,21] Also, Raman excitation into this absorption results in significant resonance enhancement of the Fe-O-Fe moiety (see below), a property observed with other trapped valence compounds.[22]

In contrast to **2**, the visible absorption maxima of compound **3**, are quite different. Compound **3** has two intense bands at 488 and 527 nm that are also observed in other oxo-bridged diferric complexes (Table 3-1). For example, the electronic absorption spectrum of $[Fe_2O(OAc)_2(tacn)_2]^{2+}$, the di-μ-acetato di-tacn analog of **3**, displays peaks at 464 and 543 nm that have been assigned as ligand field and oxo→Fe(III) LMCT bands, respectively.[14,23] Furthermore, the 685-nm absorption of **2** is considerably more intense than the ligand field bands at 600-750 nm in the diferric complexes.[19] Clearly, the trapped valence state of **2** has altered the electronic properties of the cluster resulting in an electronic spectrum remarkably different from its diferric analogue, compound **3**.

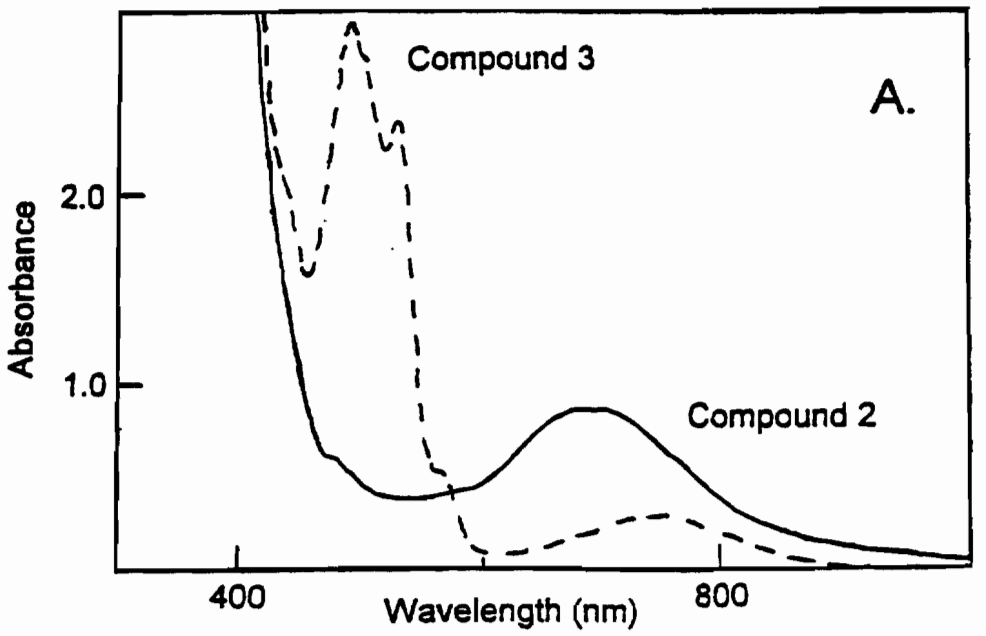

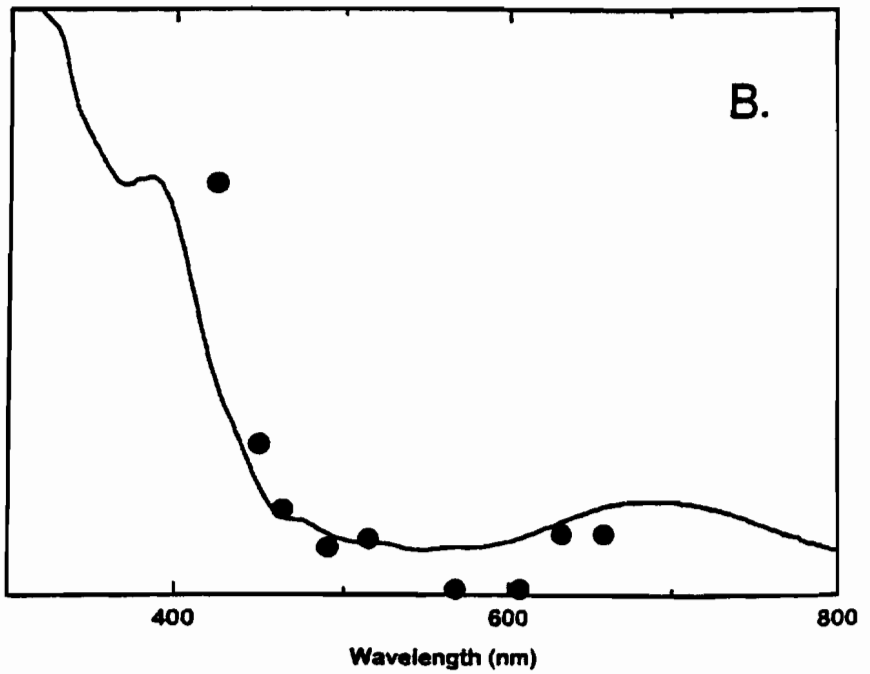

Figure 3-5. (A) Electronic absorption spectra of compounds **2** and **3** (BPh_4^- salts) in CH_2Cl_2. (B) RR enhancement profile for compound **2** (BPh_4^- salt, crystals), RR intensity of I_{708}/I_{1001} for μ-^{16}O-labeled **2** are shown as black dots.

Table 3-1: Electronic absorption maxima of selected diiron proteins and model compounds.[a]

Mixed-Valence Complexes		Diferric Complexes			
Compound 2[b]	semi-metHr[c]	Compound 3[b]	$Fe_2O(Ac)_2(tacn)_2^{2+}$[d,e]	RibRed[f]	$[Fe_2O(N5)Cl_3]^{+}$[d,g]
325 (2650)	330 (4400)		333 (7864)	325 (9400)	327 (11400)
385 (1930)	370 (3000)	385 (2100)	368sh	370 (7200)	360sh (7200)
475 (306)	490 (360)	488 (1477)	464 (1310)		
529 (200)		527 (1211)	508sh	500 (800)	
564 (208)			543sh		540sh (420)
685 (435)	670 (80)	748 (149)	745 (142)	600 (300)	655sh (120)

[a]Units of nanometers (nm), numbers in parentheses are molar extinction coefficients in units of M^{-1} cm^{-1} per 2 Fe. [b]In CH_2Cl_2. [c]Reference 18. [d]In CH_3CN. [e]Reference 24. [f]Reference 14. [g]Reference 25.

(B) ***Resonance Raman Spectra.*** Spectra of **2** were collected on both the $CF_3SO_3^-$ and BPh_4^- salts prepared using either O_2 and 4-methylmorpholine *N*-oxide as the oxidant. The RR spectra of **2** ($CF_3SO_3^-$ salt), containing ^{16}O- or ^{18}O-labeled oxo bridge, exhibit a number of features (Fig. 3-6) that were previously observed in the Raman spectrum of compound **1** (Fig. 3-4). These include the intense phenyl ring modes from the bridging ligands at ~1003 and 1034 cm^{-1}. The broad feature between 300 and 600 cm^{-1} is due to Raman scattering from the glass walls of the capillary tubes holding powdered samples (The Raman spectra of the crystalline samples of **1** and **2**, Figs. 3-4 and 3-8, did not display this artefact because the laser light was focused on the larger crystals in the interior of the tubes instead of on the powder adhered to the glass walls). In addition, there is an intense new peak at 702 cm^{-1} (Fig. 3-6A) that shifts -30 cm^{-1} in the spectrum of the μ-^{18}O isotopomer (Fig. 3-6B). This peak is assigned to ν_{as}(Fe-O-Fe), based on the magnitude of the isotope shift ($\Delta\nu_{theoretical}$ = -31 cm^{-1})[15] and its frequency which is close to the ~720-cm^{-1} value predicted for a diferric complex with a 117.8° Fe-O-Fe bond angle.[14] A weaker band at 1404 cm^{-1} shifts -60 cm^{-1} in the spectrum of the μ-^{18}O isotopomer and is assigned to the first overtone, $2\nu_{as}$(Fe-O-Fe). The frequency and isotope shift of the asymmetric stretching mode of **2** is remarkably similar to the behavior of ν_{as}(Fe-O-Fe) in diferric proteins and model compounds (Table 3-2). Furthermore, the spectrum of the μ-^{18}O isotopomer of **2** prepared by the oxidation of μ-^{18}O-labeled **1** with 4-methylmorpholine *N*-oxide (Fig. 3-6C) is very similar to the spectrum of **2** prepared by the oxidation with $^{16}O_2$ (Fig. 3-6B). It displays the same features within ± 2 cm^{-1} and demonstrates that the two preparations result in chemically equivalent products.

The RR spectrum of the BPh_4^- salt of **2** reveals the same isotope sensitive features as the $CF_3SO_3^-$ salt but at slightly higher Raman shift (Fig. 3-7). The intense peak at 711 cm^{-1} (Fig. 3-7A) shifts -36 cm^{-1} in the μ-^{18}O isotopomer (Fig. 3-7B) and is similarly assigned to ν_{as}(Fe-O-Fe). The overtone peak, $2\nu_{as}$, at 1416 cm^{-1} shifts -71 cm^{-1} in the μ-^{18}O isotopomer. Again, the μ-^{18}O sample of **2** prepared using 4-methylmorpholine *N*-oxide (Fig. 3-7C) is identical to the $^{16}O_2$-oxidized product (Fig. 3-7B).

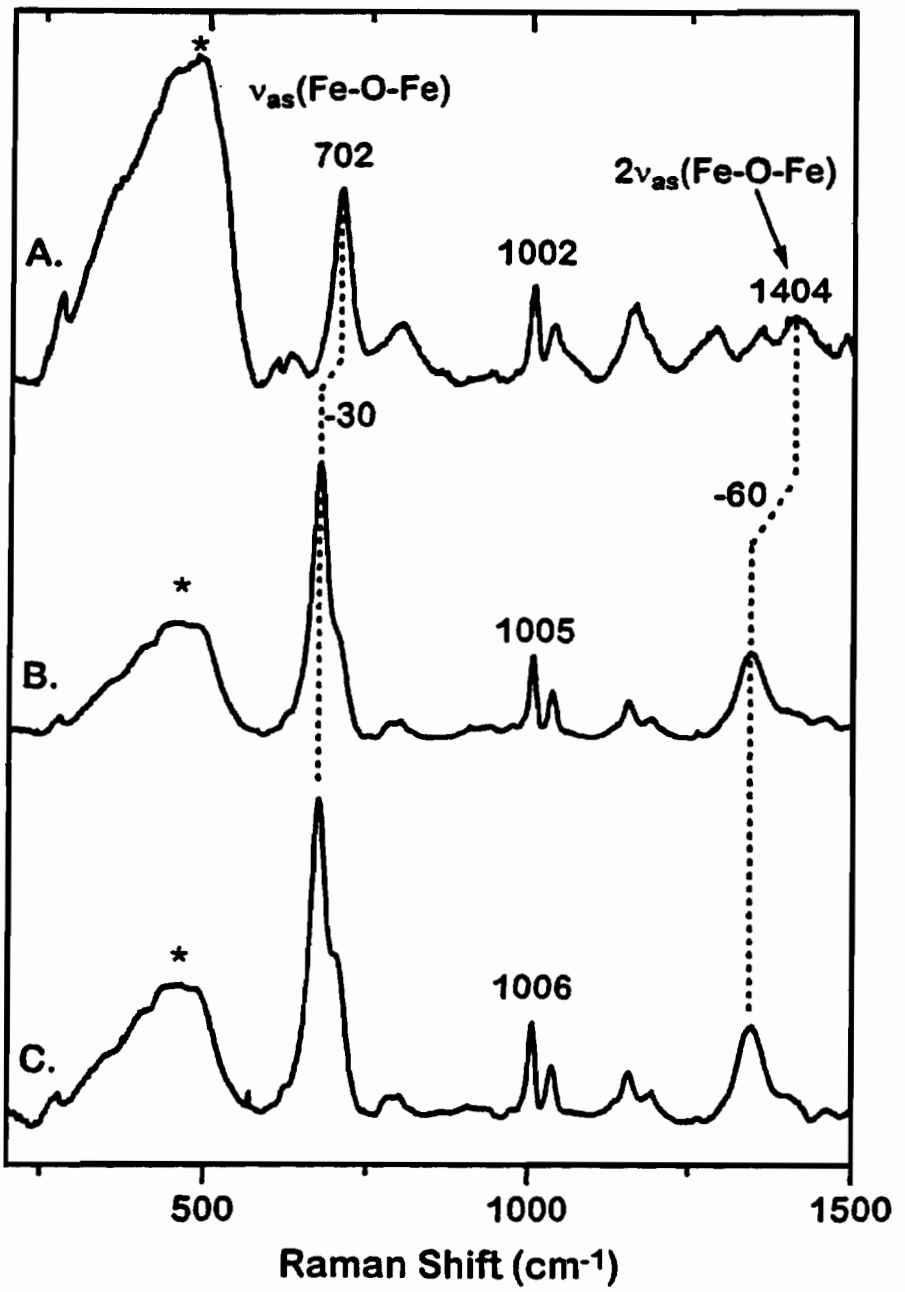

Figure 3-6. Resonance Raman spectra of compound **2** ($CF_3SO_3^-$ salt, powder). (A) μ-^{16}O isotopomer prepared from the oxidation of μ-^{16}OH-labeled **1** by $^{16}O_2$. (B) μ-^{18}O isotopomer prepared from the oxidation of μ-^{18}OH-labeled **1** by $^{16}O_2$. (C) μ-^{18}O isotopomer prepared from the oxidation of μ-^{18}OH labeled **1** by 4-methylmorpholine *N*-oxide. RR scanning conditions are the same as those used in Figure 3-4. *Indicates glass artefact.

Table 3-2: Frequencies and intensities of Fe-O-Fe vibrational modes for selected diiron proteins and model compounds.

Sample	ν_{as}(Fe-O-Fe)[a]	ν_s(Fe-O-Fe)[a]	I_{as}/I_s	Δ(Fe-O)[b]	∠Fe-O-Fe[c]
Compound 2 ($CF_3SO_3^-$)[d]	702 (-30)	*n.d.*	»10	0.05	118
Compound 2 (BPh_4^-)[d]	711 (-36)	*n.d.*	»10		
$[Fe_2O(OAc)_2(tacn)_2]^{2+}$,[e]	749 (-33)	540 (-17)	<0.04	<0.01	119
$[Fe_2O(OAc)_2(HBpz_3)_2]^{2+}$,[e]	751 (-30)	528 (-17)	<0.04	0.01	124
Δ^9 Desaturase[f]	747 (-34)	519 (-18)	0.29		123[g]
oxyHemerythrin[h]	753 (-37)	486 (-14)	0.18	<0.01	125
Ribonucleotide Reductase[h]	756 (-25)	493 (-13)	0.20		130
$[Fe_2O(N5)Cl_3]^+$,[i]	850 (-44)	425	4.2	0.03	150
$[Fe_2O(N5)Br_3]^+$,[i]	846	422	2.4	0.07	151

[a]Units of cm^{-1}, numbers in parentheses are ^{18}O shifts. [b]Units of Å. [c]Units of degrees. [d]This work. [e]Reference 24. [f]Reference 3. [g]Calculated from ν_s(Fe-O-Fe) using the equations in reference 15. [h]Reference 14. [i]Reference 25.

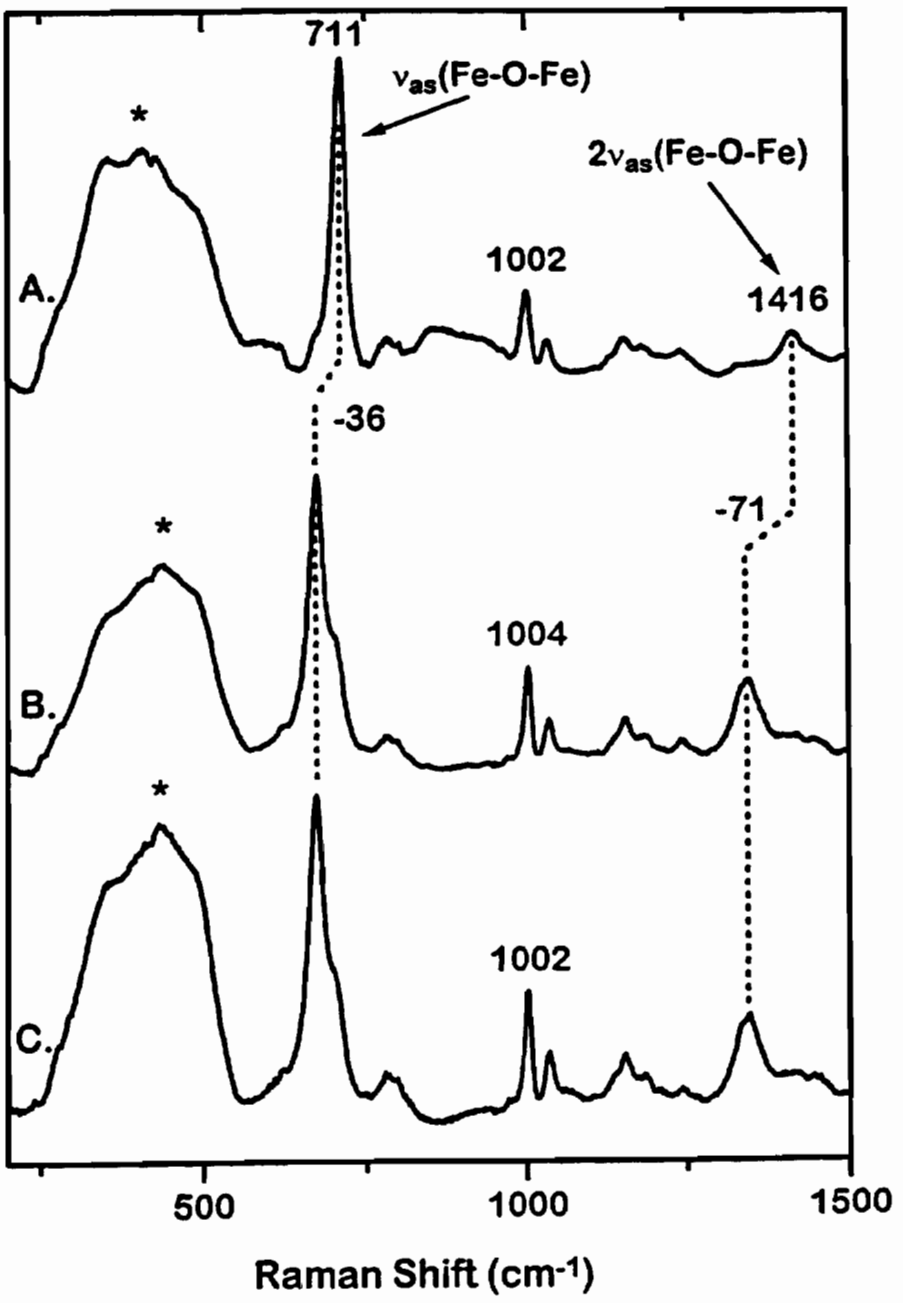

Figure 3-7. Resonance Raman spectra of compound 2 (BPh_4^- salt, powder). (A) μ-^{16}O isotopomer prepared from the oxidation of μ-^{16}OH-labeled 1 by $^{16}O_2$. (B) μ-^{18}O isotopomer prepared from the oxidation of μ-^{18}OH-labeled 1 by $^{16}O_2$. (C) μ-^{18}O isotopomer prepared from the oxidation of μ-^{18}OH labeled 1 by 4-methylmorpholine *N*-oxide. RR scanning conditions are the same as those used in Fig. 3-4.

Another sample of **2** that was crystallized after preparation from a μ-^{18}O precursor reveals RR peaks at 708 and 1414 cm^{-1}, in addition to the peaks at 673 and 1346 cm^{-1}, which indicate that 50% of the bridge has been displaced by ^{16}O (Fig. 3-8). These crystalline samples were exposed to ambient H_2O in the anaerobic chamber used for loading the capillaries. In contrast, the capillaries containing the powdered samples (Figs. 3-6 and 3-7) were filled and sealed in a dry anaerobic chamber. We found that the μ-oxo bridge in **2** is readily exchanged by water. Addition of 6% H_2O to a concentrated solution (~5 mg/30 μL) of this same μ-^{18}O sample in dry, anaerobic CH_3CN resulted in immediate and complete bridge exchange, so that only the 705-cm^{-1} peak due to the μ-^{16}O species was observed in the RR spectrum within 1 min as well as a significant amount of diferric product due to a small amount of dissolved O_2 in the water (Fig. 3-9). Since μ-oxo exchange with water is very rapid in **2**, the presence of a 708-cm^{-1} peak in the μ-^{18}O sample was probably due to rapid exchange of oxygen between the Fe-O-Fe moiety and water vapor in the anaerobic chamber. Oxo bridge exchange with solvent has also been observed previously in other μ-oxo diferric complexes.[24]

Intensity Ratios. A diferric complex with an Fe-O-Fe angle of 118° is predicted to exhibit a ν_s(Fe-O-Fe) stretching mode at ~540 cm^{-1} that shifts ~18 cm^{-1} to lower energy with μ-^{18}O substitution.[14] In agreement with this prediction, compound **3** exhibits an intense ν_s(Fe-O-Fe) stretch at 519 cm^{-1} that shifts -20 cm^{-1} with μ-^{18}O (Fig. 3-10). A search for a comparable symmetric Fe-O-Fe mode in the mixed valence compound **2** yielded no other ^{18}O-sensitive modes between 400 and 600 cm^{-1} in the RR spectrum (Fig. 3-8). Consequently, **2** represents the first example of a symmetric, μ-oxo bridged diiron compound with an intense asymmetric but no detectable symmetric Fe-O-Fe stretch.

The intensity ratio of ν_{as}(Fe-O-Fe) relative to ν_s(Fe-O-Fe), I_{as}/I_s, is generally less than 0.1 for symmetric Fe-O-Fe model complexes and less than 0.3 for the slightly less symmetric environments in proteins.[14] The only two published examples of compounds displaying an I_{as}/I_s ratio greater than 1 are the $[N5FeOFeX_3]^+$ clusters, where X = Cl or Br and N5 = *N*-(2-hydroxyethyl)-*N*,*N*',*N*'-tris-(2-benzimidazolylmethyl)-1,2-diaminoethane.[25] The ligand asymmetry in these clusters results in unequal Fe-oxo bond lengths [Δ(Fe-oxo)

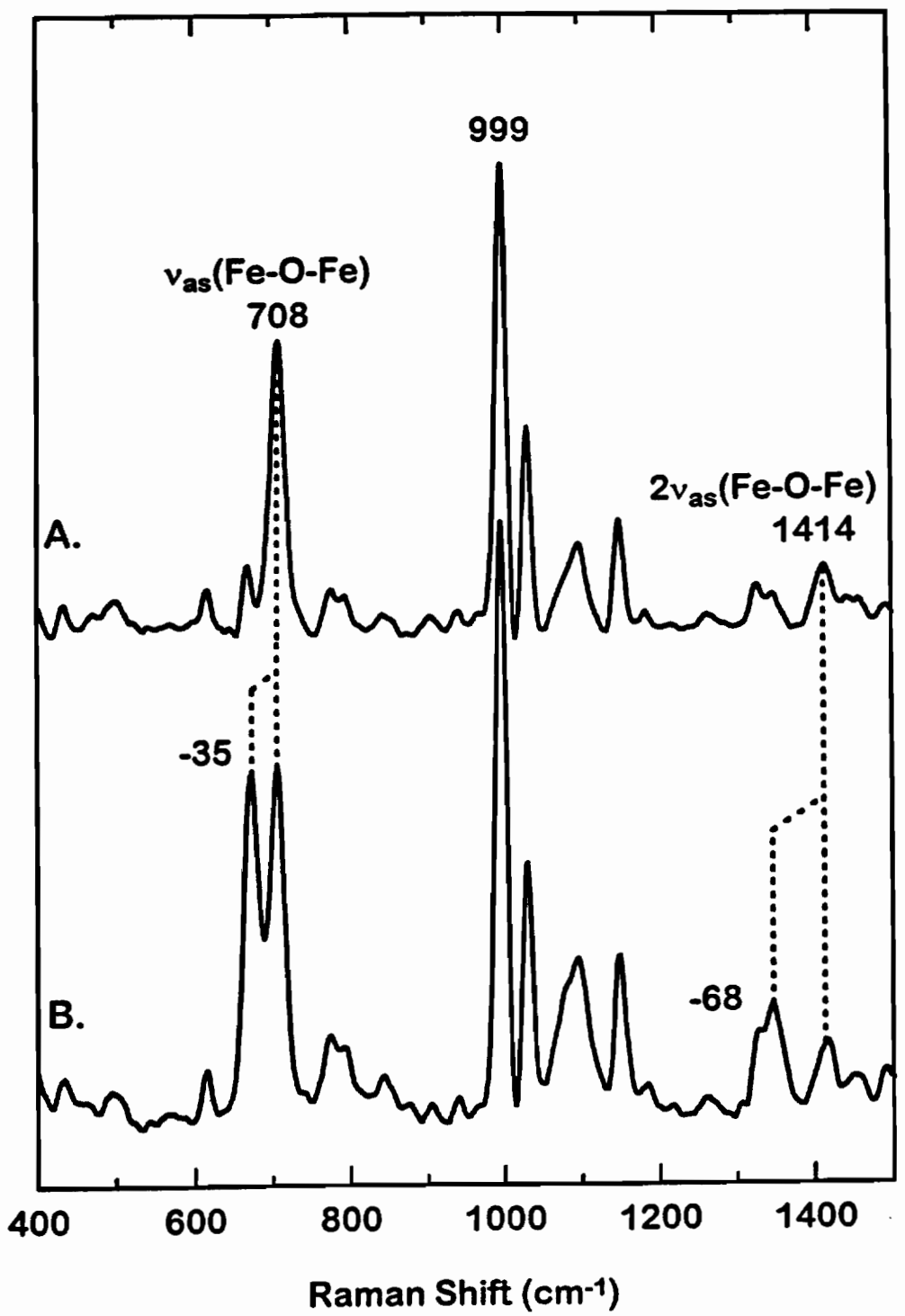

Figure 3-8. Resonance Raman spectra of the μ-^{16}O (A) and μ-^{18}O (B) isotopomers of **2** (BPh_4^- salt, crystals) after exposure of the crystals to ambient H_2O in an anaerobic chamber. RR scanning conditions are the same as those used in Fig. 3-4.

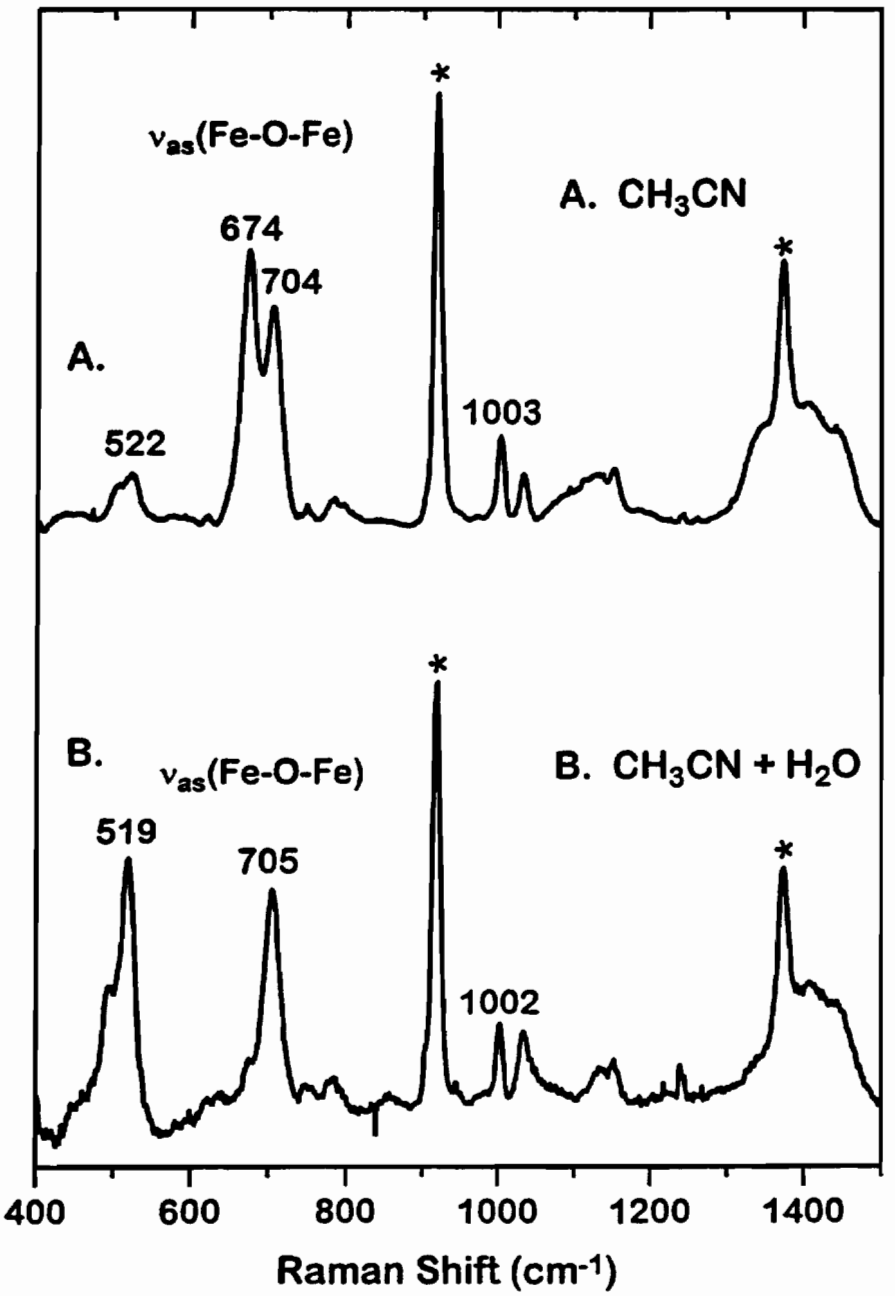

Figure 3-9. Resonance Raman spectra of compound **2** ($CF_3SO_3^-$ salt) in CH_3CN. (A) 5 mg compound **2** in 30 µl CH_3CN. (B) 5 mg compound **2** + 2 µl H_2O in 30 µl CH_3CN. These spectra were obtained as in Fig. 4 except that the power was decreased to 10 mW and the exposure time was 30 min in (A) and limited to 1 min after H_2O addition in (B). *Indicates solvent peaks.

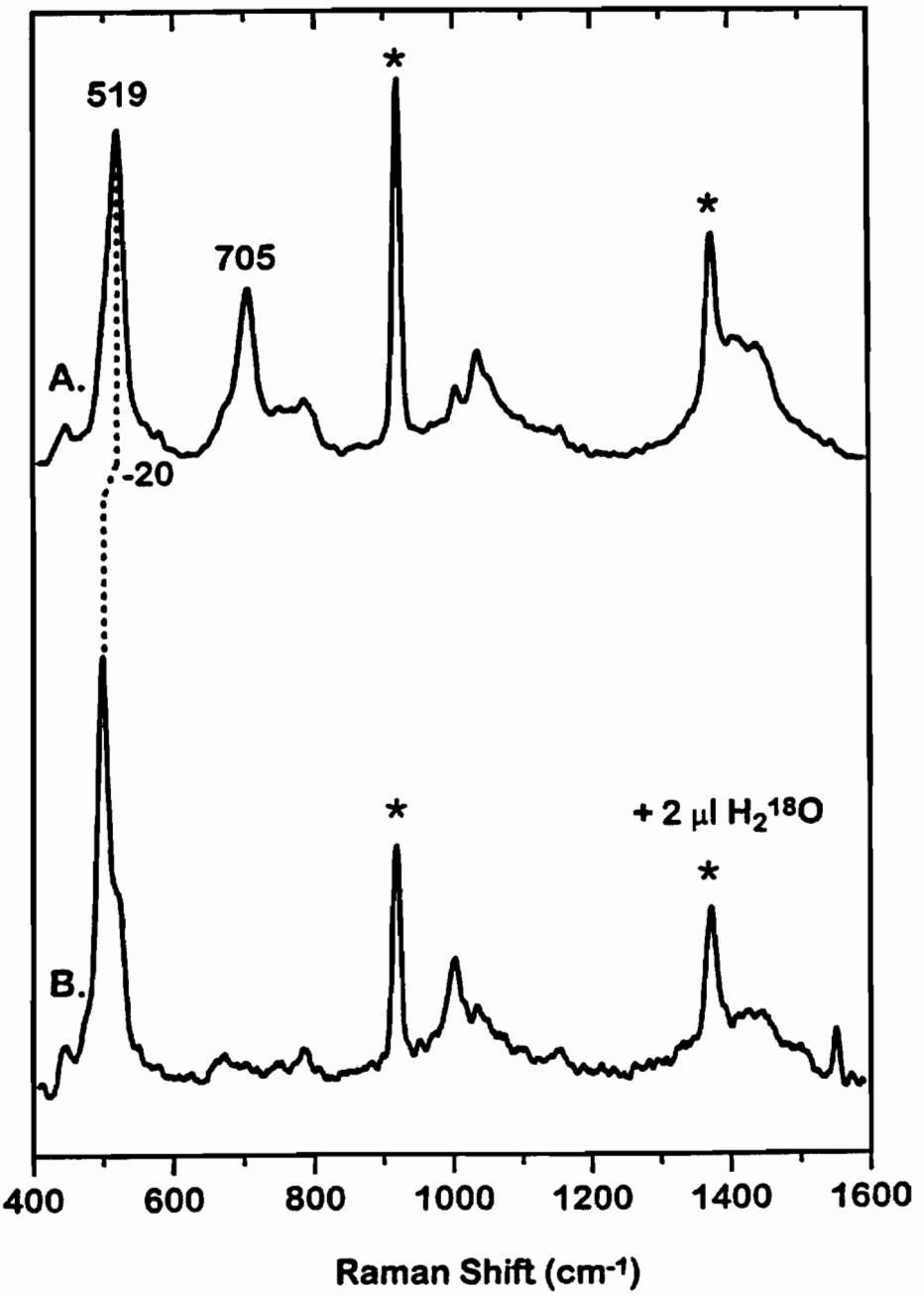

Figure 3-10. Resonance Raman spectra of compound **3** ($CF_3SO_3^-$ salt) in CH_3CN (~2 mg/20 µl) prepared from the exposure of compound **2** to air for 4 hrs. (A) µ-^{16}O-isotopomer. (B) µ-^{16}O isotopomer + 2 µl $H_2{}^{18}O$. The spectra were obtained with 413.1 nm excitation (15 mW), 298 K, 60 s exposure time, 4 cm^{-1} resolution. *Indicates solvent peaks.

= 0.031 Å and 0.071 Å, respectively, for the Cl_3 and Br_3 complexes] and I_{as}/I_s ratios of 4.2 and 2.4, respectively (Table 3-2). For compound **2**, the 0.047 Å difference in Fe-oxo bond lengths and the presence of discrete, localized Fe(II) and Fe(III) centers apparently provide enough asymmetry to make ν_{as} the only detectable Fe-O-Fe vibration.

The trapped valence state of compound **2** is surprising, given that both iron atoms are 6-coordinate and possess identical bridging and capping ligands. Previously, ion pairing or solid-state effects have been used to explain the trapped valence state in other diiron clusters that lacked crystallographic symmetry.[21,26] However, compound **2** has a symmetrical distribution of counterions in the crystals and also appears to be trapped valence in CH_3CN solution, judging by the continued intensity of the ν_{as}(Fe-O-Fe) vibration (Fig. 3-9). It is likely that the mixed valence state is a favorable condition for compound **2** due to steric effects from the terminal and bridging ligands. Because the Me_3tacn and Ph_3CCOO ligands are so bulky, oxidation of compound **1** to compound **2** is facile but the second oxidation to compound **3** is hindered due to the large ligand reorganization energy required to change the metal-ligand bond lengths during the conversion from the mixed valence to the diferric state. A similar behavior has been observed for other bimetallic clusters with large ligand sets. Bosnich and coworkers report that oxidation of the first metal atom leads to deactivation of the second metal in diiridium(I), and dirhodium(I) clusters with PNNP ligands.[27] Second-metal deactivation has also been proposed for dicobalt(II) clusters with bulky macrocyclic ligands.[28] These reports are analogous to the observation of stable mixed valence states in multinuclear iron-sulfur proteins and model compounds.[29]

Selective resonance enhancement of ν_{as}(Fe-O-Fe). This selective enhancement of the ν_{as} mode in **2** can be justified by examining the changes in the Fe-O-Fe nuclear coordinates during RR excitation. In the ground state, the Fe^{2+}-O-Fe^{3+} moiety displays two distinct Fe-oxo bonds that differ in length by 0.047 Å. Upon Raman excitation, the molecule is promoted into an excited state via photoinduced electron transfer from the μ-oxo ligand onto the Fe^{3+} atom (when excited into the LMCT band) or from the Fe^{2+} ion to the Fe^{3+} atom (when excited into the IT band). The net difference in nuclear coordinates between the ground and excited states can be expressed as an increase in the length of one

Fe-oxo bond concomitant with either no change or a decrease in the second Fe-oxo bond. Assuming a 3-atom model of C_{2v} symmetry, the nuclear coordinates that change most upon photoexcitation correspond to the symmetric and asymmetric normal stretching modes ($a_1 \sim \nu_s$ and $b_2 \sim \nu_{as}$). Both of these modes are Raman active in strict C_{2v} symmetry.[12] In the resonance Raman effect, coordinates in the molecule that most closely resemble the changes from the ground state to the excited state receive the greatest resonance enhancement. Clearly, if LMCT or IT transitions result in asymmetric changes in the Fe-oxo bonds, that change in nuclear coordinates most closely resembles the ν_{as} vibrational mode. The changes in nuclear coordinates corresponding to the ν_s mode will also contribute to the Raman intensity, but the resonance enhancement due to the larger net changes along the asymmetric coordinate will dominate over the normal Raman contribution along the symmetric coordinate. Consequently, the ν_{as} mode is the only Fe-O-Fe vibration observed in the RR spectra of **2**.

Resonance enhancement profile. A resonance enhancement profile of the normalized intensity of the asymmetric stretch (I_{708}/I_{1001}) obtained with crystalline samples of **2** (BPh_4^- salt) is shown in Figure 3-5. Data were collected at 413.1, 441.6, 457.9, 488.0, 514.5, 574.1, 618.5, 647.9, and 676.4 nm on the same sample under similar instrumental conditions. This profile shows that the asymmetric stretch obtains it greatest enhancement near the 385-nm absorption maximum and closely tracks with the recorded absorption spectrum. Almost no resonance enhancement is observed beyond 514.5 nm until one reaches the absorption envelope of the IT band at 685 nm. Resonance enhancement of metal-ligand vibrations using excitation within an IT band has been observed in other mixed valence compounds.[22,30] This excitation profile and the isotope shift data confirm the assignments of the 385- and 685-nm absorption bands as LMCT and IT transitions, respectively.

Conclusions

Evidence for a trapped valence state. The mixed valence character of compound **2** is strongly supported by the magnetic susceptibility measurements and the

charge balance of the synthetic reaction.[8] Furthermore, the asymmetry of the Fe-O-Fe moiety due to the trapped valence state is demonstrated by the strong resonance enhancement of the asymmetric stretching mode over the corresponding symmetric stretching mode. In addition, the properties of the 685-nm IT band provide a quantitative basis for the assignment of compound **2** as a localized trapped valence system.

A qualitative diagram describing the potential energy of the system versus nuclear configuration can be constructed for class I and class II mixed complexes (Fig. 3-11). The ground state potential well has two local minima denoting the energy minima of states *a* and *b*, respectively. Intervalence transfer (E_{OP}) is depicted as a vertical arrow from a global minimum of the ground state to the photoinduced excited state described by a single minimum. In class II molecules, the extra electron density in the excited state is delocalized across the two Fe atoms, whereas in class I, the electron density is transferred to the other metal. The energy separation between the transition state for thermal electron transfer and the energy minimum of the excited state is twice the resonance energy of states *a* and *b*, expressed as $2H_{ab}$. ΔG^* is expressed as the height of the thermal activation barrier between states *a* and *b*.

The degree of electron delocalization (α^2) can be estimated from the properties of the IT band and the Fe-Fe interatomic distance[31]:

$$(1)\quad \alpha^2 = (C\varepsilon\Delta\nu_{1/2})/(E_{OP}\, d^2)$$

where ε is the molar extinction coefficient of the IT band (435 $M^{-1}\,cm^{-1}$), $\Delta\nu_{1/2}$ is the full width at half maximum (3480 cm^{-1}), E_{OP} is the energy maximum (14,600 cm^{-1}), *d* is the Fe^{2+}-Fe^{3+} interatomic distance (3.123 Å) and *C* is a constant (4.2×10^{-4} $Å^2\cdot M\cdot cm$). Generally, α^2 can take values from ~0 to ~1 where the degree of delocalization increases with increasing α^2. The calculated value of α^2 for **2** of 4.5×10^{-3} (Table 3-3) is within 1 order of magnitude of other class II trapped valence complexes[21] but is ~28-fold smaller than the α^2 value for the μ-hydroxo-tribridged, diferric analogue, $[Fe_2(OH)_3(Me_3tacn)_2]^{2+}$, categorized as a class III delocalized complex.[20,32]

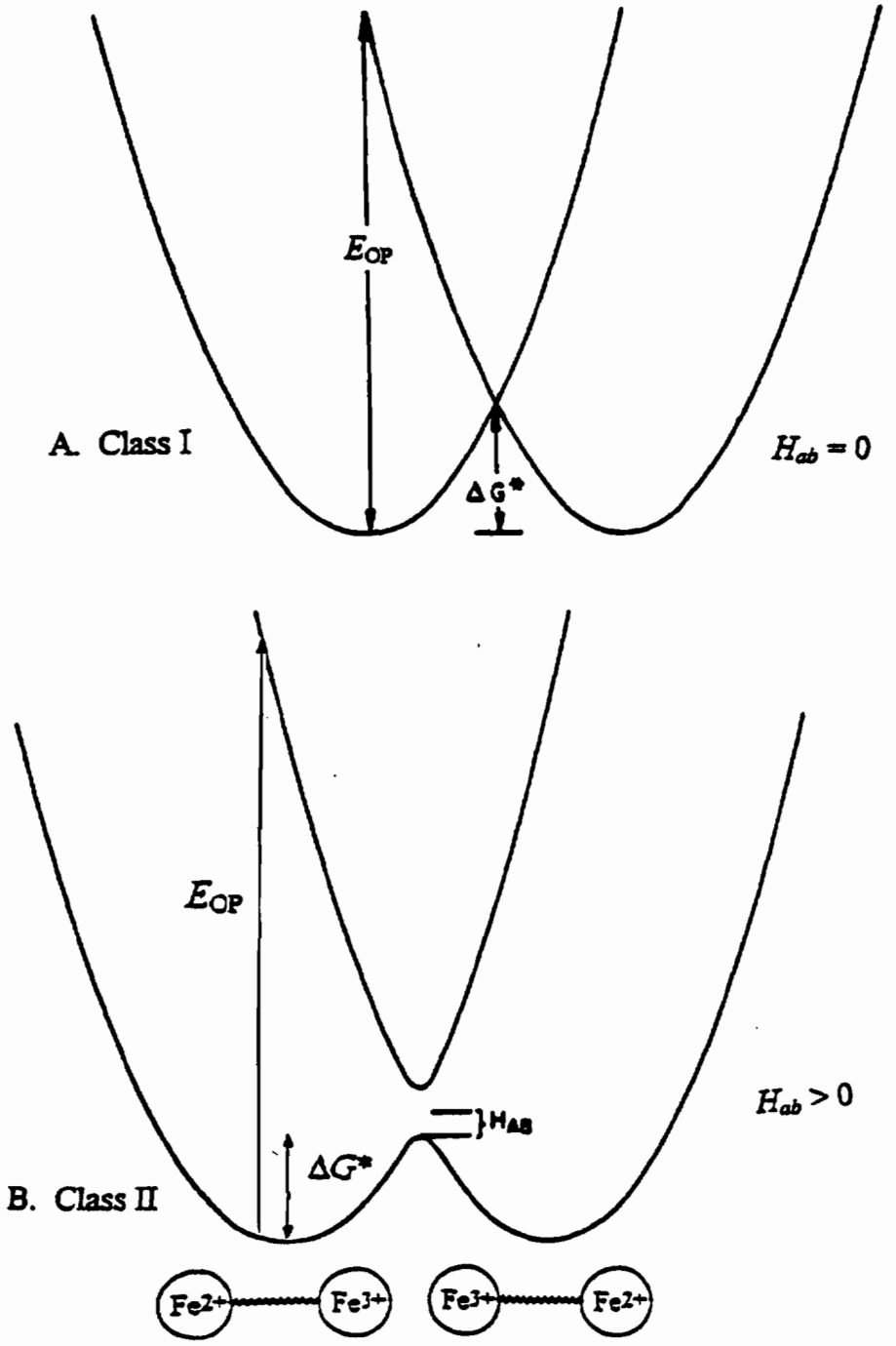

Figure 3-11. Potential energy versus nuclear configuration for an asymmetric mixed-valent complex designated as (A) class I and (B) class II, adapted from reference 31. Calculations of $2H_{ab}$, and ΔG^* are described in the text and are presented in Table 3-3.

Table 3-3: Intervalence transfer properties of selected mixed-valence diiron compounds.[a]

Sample	E_{op}[b]	ε[c]	$\Delta\nu_{1/2}$[b]	d[d]	α^2	H_{ab}[b]	ΔG^{*}[e]	Class[f]
Compound 2[g]	14,600	435	3480	3.123	4.5×10^{-3}	980	32	II
$[Fe_2(OH)_3(tmtacn)_2]^{2+}$[h]	13,200	5700	4411	2.509	1.3×10^{-1}	4700	-17.1	III
$[Fe_2BPMP(O_2CC_2H_5)_2]^{2+}$[i]	7420	310	5290	3.365	8.2×10^{-3}	670	14.2	II

[a]Terms are defined in equations 1-3. [b]Units of cm^{-1}. [c]Units of $M^{-1}\,cm^{-1}$. [d]Units of Å. [e]Units of kJ/mol. [f]Classification scheme according to reference 9. [g]This work. [h]Ref. 20. [i]Ref. 21.

The resonance energy between the two trapped valence states (H_{ab}) can be calculated from the square root of the degree of delocalization and the energy (in cm^{-1}) of the IT transition:[21]

$$(2)\ H_{ab} = \alpha E_{OP}$$

As H_{ab} approaches zero, the compound approaches the definition of a strict class I delocalized system with no electronic coupling of the two states (Fig. 3-11A). The calculated value of H_{ab} for compound **2** equal to 980 cm^{-1} is similar to values calculated for other class II systems (Fig. 3-11B), [21] suggesting that the two states are only weakly to moderately coupled in solution at room temperature, but is more than 4-fold smaller than H_{ab} for fully delocalized class III systems.[20,32]

The free energy of thermal electron transfer (ΔG^*) can be estimated from:[21]

$$(3)\ \Delta G^* = (\lambda \backslash 4) - H_{ab}$$

where $\lambda \approx E_{OP}$ for mixed valence systems with symmetric or nearly symmetric metal sites. Clearly, as H_{ab} increases, the free energy for thermal electron transfer decreases and the system approaches the strict class III definition for a fully delocalized system. The calculated value of ΔG^* for **2** equal to 2.7×10^3 cm^{-1} (~32 kJ/mol) is more than 12-fold larger than the thermal contribution to the kinetic energy of the system (k_BT = 207 cm^{-1} at 298 K, where k_B is Boltzmann's constant = 0.694 cm^{-1}/K). Therefore, the height of the free-energy barrier between the two states is too great for spontaneous thermal electron transfer to occur. On the other hand, ΔG^* in class III systems is ≤ 0, implying that thermal electron transfer between the two states is spontaneous and the system is fully delocalized. This analysis confirms the spectroscopic finding that compound **2** is in a trapped valence state with only weak electronic coupling in solution.

Outer-sphere reaction with dioxygen. The preservation of the μ-oxo ligand during the oxidation of **1** to **2** indicates that the electron transfer during the conversion of

1 to **2** proceeds via an outer-sphere mechanism. Anhydrous samples of ^{18}O-bridged **2** prepared from the oxidation of ^{18}OH-bridged **1** showed only a small shoulder at ~701 cm^{-1} due to the presence of approximately 10-20% μ-^{16}O ligand (Figs. 6B, and 7B). If oxidation proceeded via an inner-sphere mechanism, the products should have contained predominantly μ-^{16}O. Further support for an outer-sphere mechanism comes from the fact that 4-methylmorpholine *N*-oxide, which is not expected to be Fe-coordinated, gives quantitative oxidation of **1** to **2** with no incorporation of ^{16}O from the NO moiety into **2**. The small amounts of μ-^{16}O in these supposedly anhydrous samples is presumably due to trace amounts of unlabeled H_2O with which these samples came into contact with during synthesis and/or transfer. It is of interest that similar trace amounts of μ-^{16}O are present using two different salts of **1** (Figs. 6B and 7B) and using two different oxidants (Figs. 6B vs. 6C and 7B vs. 7C).

One can propose a mechanism for the oxidation of **1** to **2** via outer-sphere electron-transfer (Fig. 3-12). The X-ray crystal structure of **1** reveals that the Me_3tacn capping ligands and the Ph_3CCOO bridging ligands probably produce too much steric hindrance around the Fe atoms for molecules such as O_2 to react directly with the metals. Consequently, O_2 can only react with **1** directly above the μ-hydroxo ligand. Electron transfer from **1** to O_2 results in the formation of **2** and a hydrogen bonded superoxide. The superoxide formed during the first step can react with a second molecule of **1**, rapidly forming H_2O_2 and a second equivalent of **2**, consistent with the reaction stoichiometry. In this mechanism, O_2 is reduced to H_2O_2 without the need to cleave the O-O bond or to substitute an oxygen atom into the cluster, consistent with the results from the RR experiments.

The outer-sphere oxidation of **1** is in sharp contrast to the behavior of ribonucleotide reductase [33] and the $Fe_2(O_2CH)_4$(BIPhMe)$_2$ model compound,[34] both of which quantitatively incorporate an atom from O_2 into the μ-oxo group during the conversion from the diferrous to diferric state. These results require an inner-sphere reaction and suggest a bridging O_2 intermediate. The diferrous center in ribonucleotide reductase has 4-coordinate irons that can readily accommodate a bridging peroxide. The diferrous center in the BIPhMe model compound has 5- and 6-coordinate irons, but also a

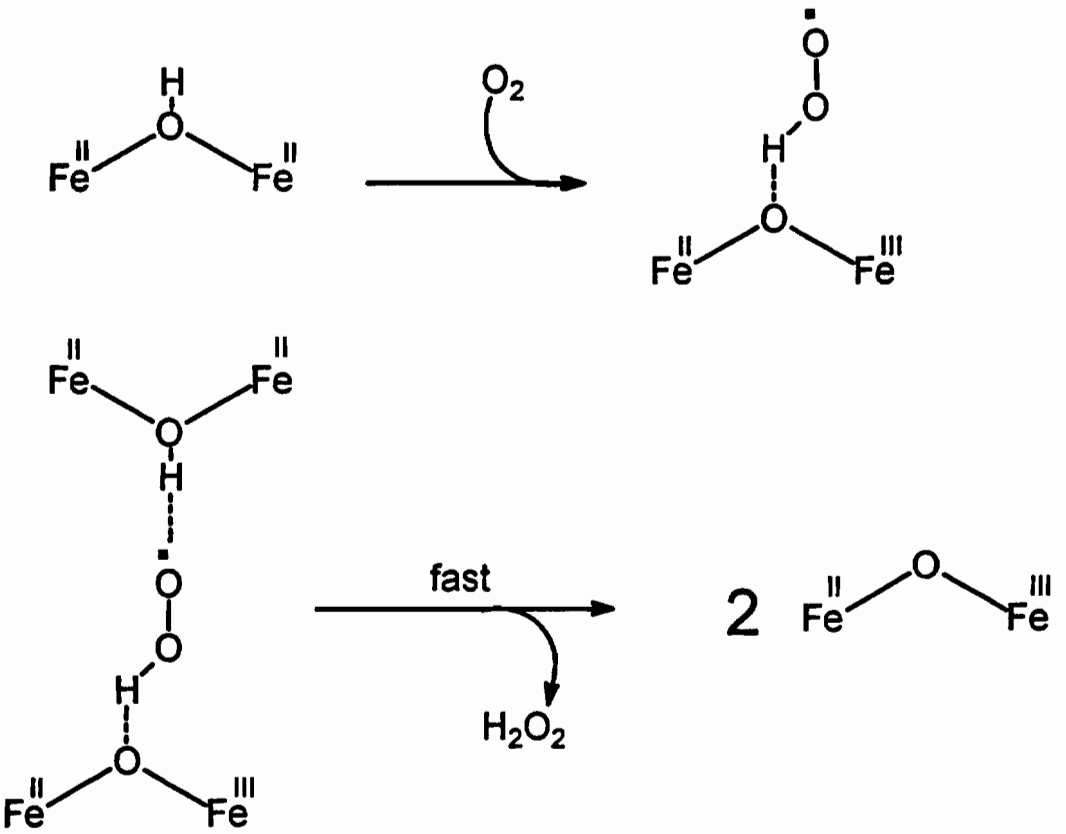

Figure 3-12. Proposed mechanism for the oxidation of **1** to **2** by O_2 via outer-sphere electron-transfer.

readily displaceable monodentate formate bridge. Compound **1** is coordinatively saturated with the bridging OH and carboxylates remaining intact in the presence of O_2. The outer-sphere reaction of **1** results in the reduction of O_2 to H_2O_2 and the stable mixed valence product, **2**. This differs significantly from the inner-sphere reactions of ribonucleotide reductase or the model compound where the bridging O_2 undergoes reduction to H_2O and produces fully oxidized diferric products.[33,34]

Mixed valence intermediates in biology. Studies of diiron enzymes have begun to discover reaction intermediates other than the diferrous and diferric states. In horse spleen ferritin, EPR experiments have identified a $g' = 1.87$ signal tentatively assigned to a oxo-bridged mixed valence $Fe^{2+/3+}$ dimer when apoprotein is allowed to react with O_2 and Fe^{2+}.[35] Purple acid phosphatase, another diiron protein, is actually in a mixed valence $Fe^{2+/3+}$ state in its active (pink) form.[36] Compound X, an intermediate in the reaction cycle of ribonucleotide reductase, appears to be in a high valence $Fe^{3+/4+}$ state, possibly as a bis-μ-oxo cluster.[37]Thus, mixed-valence iron clusters are not uncommon in enzymology.

The tendency of asymmetric diiron complexes to produce a strongly enhanced ν_s(Fe-O-Fe) mode[14] at 700-850 cm^{-1} has implications for the identification of enzymatic reaction intermediates by RR spectroscopy. A model for compound X of ribonucleotide reductase, $[Fe_2O_2(5\text{-}Me_3\text{-}TPA)_2]^{3+}$ (**4**), which contains a bis-μ-oxo core and a mixed valence Fe^{3+}/Fe^{4+} cluster.[38] The RR spectrum of **4** displays a strong band at 666 cm^{-1} that shifts -28 cm^{-1} when prepared with $^{18}O_2$, assigned to the symmetric $\nu_s(Fe_2O_2)$ core breathing mode. This frequency and isotope shift is close to the ~702 cm^{-1} frequency of ν_{as} in the spectrum of **2**. Distinguishing between mixed valence μ-oxo and di-μ-oxo clusters require careful analysis of the RR spectrum below 400 cm^{-1}. Compounds with a di-μ-oxo core display additional isotope sensitive bands in the low frequency RR spectrum assigned to $\nu(Fe_2O_2)$ modes coupled to ν(Fe-N) vibrations of the capping ligands.[39] Alternatively, if compound X proves to contain a single high valence Fe^{3+}-O-Fe^{4+} moiety with 2 additional bridging ligands, the frequency of ν_{as}(Fe-O-Fe) should be much higher in energy (750-800 cm^{-1}); closer to those displayed by ferryl (Fe^{4+}=O) species[40] and well-beyond the range reported for the bis-μ-oxo model compounds. In another case, a novel protein isolated from sulfate-reducing bacteria was shown to contain 7 non-heme iron

atoms per monomeric protein, 6 as a redox active [6Fe-6S] prismane-like cluster and 1 that is proposed to be coupled to the [6Fe-6S] cluster through an oxo bridge to form an asymmetric Fe-O-Fe cluster.[41] This latter assignment is based on the observation of an $H_2{}^{18}O$-sensitive vibration at 801 cm^{-1}, most logically assigned as ν_{as}(Fe-O-Fe), with a Fe^{4+}=O assignment being a chemically less likely alternative. Thus, careful analyses and isotopic substitutions are required to achieve conclusive vibrational assignments for multinuclear iron complexes.

References and Notes

(1) This work was performed in collaboration with Sonha S. Payne and Prof. Karl S. Hagen in the Department of Chemistry, Emory University, Atlanta, GA.

(2) Lipscomb, J. D. "Biochemistry of Soluble Methane Monooxygenase." *Ann. Rev. Miocrobiol.* **1994**, *48*, 371-399.

(3) Fox, B. G.; Shanklin, J.; Ai, J.; Loehr, T. M.; Sanders-Loehr, J. "Resonance Raman Evidence for an Fe-O-Fe Center in Stearoyl-ACP Desaturase. Primary Sequence Identity with Other Diiron-Oxo Proteins." *Biochemistry* **1994**, *33*, 12776-12786.

(4) Stubbe, J. "Ribonucleotide Reductases." *Adv. Enzymol.* **1989**, *63*, 349-419.

(5) Nordlund, P.; Eklund, H. "Di-Iron-Carboxylate Proteins." *Curr. Op. Struct. Biol.* **1995**, *5*, 758-766.

(6) Kurtz Jr., D. M. "Oxo-and Hydroxo-Bridged Diiron Complexes: A Chemical Perpective on a Biological Unit." *Chem. Rev.* **1990**, *90*, 585-606.

(7) Murray, K. S. "Synthetic Mono-, Di-, and Trinuclear Iron Clusters." *Coord. Chem. Rev.* **1974**, *12*, 1-22.

(8) Payne, S.; Hagen, K. S. "Synthesis and Spectroscopy of a Mixed-Valence μ-Oxo Tribridged Dinuclear Iron Complex." *personal communication*, Emory University, Atlanta, GA.

(9) Robin, M. B.; Day, P. "Mixed Valence Chemistry--A Survey and Classification." *Adv. Inorg. Chem. Radiochem.* **1967**, *10*, 248-422.

(10) Arena, F.; Floriani, C.; Chiesi-Villa, A.; Guastini, C. "A Mixed Valence μ-Oxo Iron(III)-Iron(II) Complex. A Polynuclear Iron-Sodium-Oxo Aggregate from the Chemical Reduction of a μ-Oxo Di-iron(III) Complex." *J. Chem. Soc. Chem. Commun.* **1986**, 1369-1371.

(11) Drüeke, S.; Chaudhuri, P.; Wieghardt, K.; Pohl, K.; Ding, X.-Q.; Bill, E.; Sawaryn, A.; Trautwein, A. X.; Winkler, H.; Gurman, S. J. "The Novel Mixed-Valence, Exchange-Coupled, Class III dimer $[L_2Fe_2(\mu\text{-}OH)_3]^{2+}$ (L = N, N', N''-trimethyl-1,4,7-triazacyclononane)." *J. Chem. Soc. Chem. Commun.* **1989**, *1989*, 59-62.

(12) Harris, D. C.; Bertolucci, M. D. *Symmetry and Spectroscopy*; Oxford Press: London, 1978.

(13) This analysis assumes strict C_{2v} symmetry.

(14) Sanders-Loehr, J.; Wheeler, W. D.; Shiemke, A. K.; Averill, B. A.; Loehr, T. M. "Electronic and Raman Spectroscopic Properties of Oxo-Bridged Dinuclear Iron Centers in Proteins and Model Compounds." *J. Am. Chem. Soc.* **1989**, *111*, 8084-8093.

(15) Wing, R. M.; Callahan, K. P. "The Characterization of Metal-Oxygen Bridge Systems." *Inorg. Chem.* **1969**, *4*, 871-874.

(16) Dollish, F. R.; Fateley, W. G.; Bentley, F. F. *Characteristic Raman Frequencies of Organic Compounds*; Dollish, F. R.; Fateley, W. G.; Bentley, F. F., Ed.; John Wiley & Sons: New York, 1974.

(17) Sanders-Loehr, J. "Binuclear Iron Proteins;" in *Iron Carriers and Iron Proteins*; Loehr, T. M. Ed.; VCH Publishers: New York, 1989, pp. 385-392.

(18) McCormick, J. M.; Reem, R. C.; Solomon, E. I. "Chemical and Spectroscopic Studies of the Mixed-Valent Derivatives of the Non-Heme Iron Protein Hemerythrin." *J. Am. Chem. Soc.* **1991**, *113*, 9066-9079.

(19) Sanders-Loehr, J.; Loehr, T. M.; Mauk, A. G.; Gray, H. B. "An Electronic Spectroscopic Study of Iron Coordination in Hemerythrin." *J. Am. Chem. Soc.* **1980**, *102*, 6992-6996.

(20) Gamelin, D. R.; Bominaar, E. L.; Mathoniere, C.; Kirk, M. L.; Wieghardt, K.; Girerd, J.-J.; Solomon, E. I. "Excited-State Distortions and Electron Delocalization in Mixed-Valence Dimers: Vibronic Analysis of the Near-IR Absorption and Resonance Raman Profiles of $[Fe_2(OH)_3(tmtacn)_2]^{2+}$." *Inorg. Chem.* **1996**, *35*, 4323-4335.

(21) Borovik, A. S.; Papefthymiou, V.; Taylor, L. F.; Anderson, O. P.; Que Jr., L. "Models for Iron-Oxo Proteins. Structures and Properties of $Fe^{II}Fe^{III}$, $Zn^{II}Fe^{III}$, and $Fe^{II}Ga^{III}$ Complexes with (μ-Phenoxo)bis(μ-carboxylato)dimetal Cores." *J. Am. Chem. Soc.* **1989**, *111*, 6183-6195.

(22) Clark, R. J.; Turtle, P. C. "Electronic and Resonance Raman Spectra of One-Dimensional Mixed-Valence Platinum-Ethylamine Complexes at ca. 80 K." *Inorg. Chem.* **1978**, *17*, 2526-2531.

(23) Reem, R. C.; McCormick, J. M.; Richardson, D. E.; Devlin, F. J.; Stephens, P. J.; Musselman, R. L.; Solomon, E. I. "Spectroscopic Studies of the Coupled Binuclear Ferric Active Site in Methemerythrins and Oxymemerythrin" *J. Am. Chem. Soc.* **1989**, *111*, 4688-4704.

(24) Spool, A.; Williams, I. D.; Lippard, S. J. "Elecronic and Vibrational Spectroscopic Analysis of the (μ-Oxo)bis(μ-carboxylato)diiron(III) Core: A Study of $[Fe_2O(O_2CCH_3)_2(TACN)_2]^{2+}$." *Inorg. Chem.* **1985**, *24*, 2156-2162.

(25) Gòmez-Romero, P.; Witten, E. H.; Reiff, W. M.; Backes, G.; Sanders-Loehr, J.; Jameson, G. B. "Dissymmetry Effects in μ-Oxo Diiron(III) Species: Structures and Spectroscopic Properties of $[N5FeOFeX_3]^+$ (X = Cl, Br) and Implications for Oxo-Bridged Dinuclear Iron Proteins." *J. Am. Chem. Soc.* **1989**, *111*, 9039-9047.

(26) Dong, T.-Y.; Hendrickson, D. N.; Pierpont, C. G.; Moore, M. F. "Mixed-Valence 1',6'-Dihalobiferricinium Salts." *J. Am. Chem. Soc.* **1986**, *108*, 963-971.

(27) Schenck, T. G.; Milne, C. R.; Sawyer, J. J.; Bosnich, B. "Bimetallic Reactivity. Oxidative-Addition and Reductive-Elimination Reactions of Rhodium and Iridium Bimetallic Complexes." *Inorg. Chem.* **1985**, *24*, 2338-2344.

(28) Bosnich, B. "Cooperative Bimetallic Reactivity." *Inorg. Chim. Acta* **1996**, *in press*.

(29) Berg, J. M.; Holm, R. M. ; Berg, J. M.; Holm, R. M., Ed. "Electronic Properties of Iron-Sulfur Clusters in Protein and Enzymes;" in *Iron Sulfur Proteins*, Que Jr., L., Ed.; John Wiley & Sons: New York, 1982, pp. 3-66.

(30) Wong, K. Y.; Schatz, P. N.; Piepho, S. B. "Vibronic Coupling Model for Mixed Valence Compounds. Comparisons and Predictions." *J. Am. Chem. Soc.* **1979**, *101*, 2793-2803.

(31) Hush, N. S. "Intervalence Transfer Absorption. Part 2. Theoretical Considerations and Spectroscopic Data." *Prog. Inorg. Chem.* **1967**, *8*, 391-444.

(32) Gamelin, D. R.; Bominaar, E. L.; Kirk, M. L.; Wieghardt, K.; Solomon, E. I. "Excited-State Contributions to Ground-State Properties of Mixed-Valence Dimers." *J. Am. Chem. Soc.* **1996**, *118*, 8085-8097.

(33) Ling, J.; Sahlin, M.; Sjoberg, B.-M.; Loehr, T. M.; Sanders-Loehr, J. "Dioxygen is the Source of the Oxo Bridge in Ribonucleotide Reductase." *J. Biol. Chem.* **1994**, *269*, 5595-5601.

(34) Tolman, W. B.; Liu, S.; Bentsen, J. G.; Lippard, S. J. "Models of the Reduced Forms of Polyiron-Oxo Proteins: An Asymmetric, Triply Carboxylate Bridged Diiron(II) Complex and Its Reaction with Dioxygen." *J. Am. Chem. Soc.* **1991**, *113*, 152-164.

(35) Chasteen, N. D.; Theil, E. C. "Fe Binding by Horse Spleen Apoferritin." *J. Biol. Chem.* **1992**, *257*, 7672-7677.

(36) Debrunner, P. G.; Hendrich, M. P.; de Jersey, J.; Keough, D. T.; Sage, J. T.; Zerner, B. "Mössbauer and EPR Study of the Binuclear Iron Center of Purple Acid Phosphatase." *Biochim. Biophys. Acta* **1983**, *745*, 103-106.

(37) Burdi, D.; Sturgeon, B. E.; Hang-Tong, W.; Edmondson, D. E.; Chen, S.; Huynh, B.-H.; Stubbe, J.; Hoffman, B. M. "Rapid Freeze Quench ENDOR Studies of X, the Diiron Intermediate Formed during Cofactor Self-Assembly of the R2 Subunit of *Escherichia coli* Ribonucleotide Reductase." *J. Am. Chem. Soc.* **1996**, *118*, 7551-7557.

(38) Que Jr., L.; Dong, Y. "Modeling the Oxygen Activation Chemistry of Methane Monooxygenase and Ribonucleotide Reductase." *Acc. Chem. Res.* **1996**, *29*, 190-196.

(39) Dong, Y.; Fujii, H.; Hendrich, M. P.; Leising, R. A.; Pan, G.; Randall, C. R.; Wilkinson, E. C.; Zang, Y.; Que Jr., L.; Fox, B. G.; Kauffmann, K.; Münck, E. "A High-Valent Nonheme Iron Intermediate. Structure and Properties of $[Fe_2(\mu\text{-}O)_2(5[Me\text{-}TPA)_2](ClO_4)_3$." *J. Am. Chem. Soc.* **1995**, *117*, 2778-2792.

(40) Kahlow, M. A.; Zuberi, T. M.; Gennis, R. B.; Loehr, T. M. "Identification of a Ferryl Intermediate of *E. coli* Cytochrome *d* Terminal Oxidase by Resonance Raman Spectroscopy." *Biochemistry* **1991**, *30*, 11485-11489.

(41) De Vocht, M. L.; Kooter, I. M.; Bulsink, Y. B.; Hagen, W. R.; Johnson, M. K. "Resonance Raman Evidence for Non-Heme Fe-O Species in the [6Fe-6S]-Containing Iron-Sulfur Proteins from Sulfate-Reducing Bacteria." *J. Am. Chem. Soc.* **1996**, *118*, 2766-2767.

Chapter 4

Resonance Raman Spectroscopic Studies of Cellobiose Dehydrogenase from *Phanerochaete chrysosporium*[1]

Jonathan D. Cohen, Wenjun Bao, V. Renganathan, S. Sai Subramaniam, and Thomas M. Loehr

(Manuscript submitted to *Archives of Biochemistry and Biophysics*, Nov. 14, 1996.)

Abstract

Cellobiose dehydrogenase (CDH), an extracellular hemoflavoenzyme produced by cellulose-degrading cultures of *Phanerochaete chrysosporium*, oxidizes cellobiose to cellobionolactone. The enzyme contains one 6-coordinate, *b*-type heme and one FAD cofactor per monomeric protein. In this work, resonance Raman (RR) spectra are reported for the oxidized, reduced, and deflavo forms of CDH as well as the individual flavin and heme domains of the enzyme obtained by peptide proteolysis. The RR spectra of the flavin and heme groups of CDH were assigned by comparison to the spectra of other hemoflavoenzymes and model compounds. Proteolytic cleavage of the CDH domains had only a minimal spectroscopic effect on the vibrational modes of the heme and FAD cofactors. Excitation of the oxidized CDH holoenzyme at 413 or 442 nm resulted in photoreduction of the heme. However, the same excitation wavelength used on the deflavo form of the enzyme or on the heme domain alone did not cause photoreduction, indicating that photo-initiated electron transfer requires the FAD cofactor. These

observations suggest an enzymatic mechanism whereby reducing equivalents obtained from the oxidation of cellobiose are transferred from the FAD to the heme. A similar mechanism has been proposed for flavocytochrome b_2 of *Saccharomyces cerevisiae* that oxidizes lactate to pyruvate (Desbois, A., Tegoni, M., Gervais, M., and Lutz, M. (1989) *Biochemistry* **28**, 8011-8022).

Introduction

Cellobiose dehydrogenase (CDH) is an extracellular hemoflavoenzyme produced by cellulolytic cultures of fungi such as *Phanerochaete chrysosporium*, *Sporotrichum thermophile*, and *Coniophora puteana*.[1-4] This enzyme catalyzes the oxidation of cellobiose to cellobionolactone (Scheme 1) in the presence of electron acceptors such as cytochrome *c*,

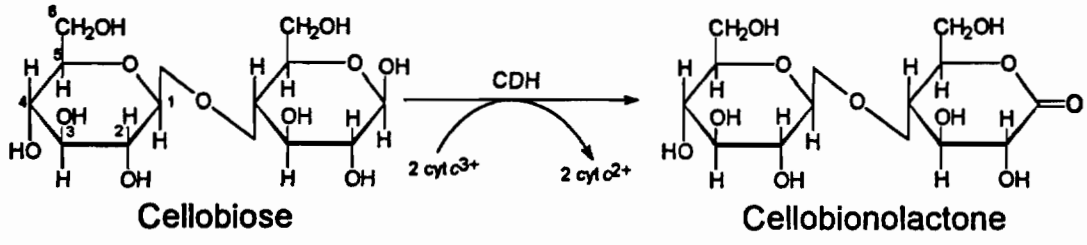

Scheme 1

quinones, Fe^{3+}, and Mn^{3+} complexes.[1,3,5] CDH from *P. chrysosporium* has a molecular mass of 90 kD as determined from SDS-PAGE,[2,3] whereas a cDNA clone encoding CDH with 755 amino acids has a mass of 80.115 kD.[6] The difference in molecular weights is due to the fact that CDH from *P. chrysosporium* is a glycoprotein and has a carbohydrate content of ~9.4%.[7] The enzyme contains one *b*-type heme and one flavin adenine dinucleotide (FAD) cofactor bound to separate domains of the monomeric protein.[6,8]

On treatment with a protease such as papain, CDH is hydrolyzed into two polypeptide fragments: a larger *C*-terminal polypeptide (M_r ~55 kD) containing the flavin, and a smaller *N*-terminal polypeptide (M_r ~35 kD) containing the heme.[9] The flavin domain shows ~50% sequence similarity to several other FAD-containing enzymes.[6,8] Furthermore, the *N*-terminal sequence analysis of the flavin domain suggests a β1-αA-β2

motif for FAD binding. In contrast, the heme domain exhibits no known sequence similarity with any other heme protein or hemoflavoenzyme.

Oxidized CDH does not bind cyanide or azide, and the reduced form does not bind CO.[3] These observations are consistent with the presence of a 6-coordinate heme with strong axial ligands. In fact, ^{1}H-NMR and nearIR-magnetic circular dichroism (MCD) studies of CDH indicate that the axial ligands to the heme are a histidine and a methionine, axial ligation equivalent to that of cytochrome *c*.[10] Such an axial ligand set is plausible in CDH from its cDNA sequence, which indicates the presence of one methionine and four histidines in the CDH heme binding domain.[6,8]

Only a few dehydrogenases are known to contain a heme and a flavin on a monomeric protein. Apart from CDH, the following dehydrogenases are classified as hemoflavoenzymes: lactate dehydrogenase (or flavocytochrome b_2 (flavocyt b_2)) from *Saccharomyces cerevisiae*,[11] spermidine dehydrogenase from *Serratia marcescens*,[12] and fumarate reductase from *Shewanella putrifaciens*.[13] Among these, flavocyt b_2, which oxidizes lactate to pyruvate, is best characterized.[11,14] This enzyme contains a flavin mononucleotide (FMN) and a 6-coordinate, low-spin, *b*-type heme with spectral characteristics consistent with two axial histidine ligands.

Resonance Raman (RR) spectroscopy is a powerful technique for the study of the structural properties of heme and flavin cofactors. Heme and flavin proteins as well as metalloporphyrins and a variety of free flavins serving as model systems have been the subject of intense study for over two decades.[15,16] Resonance Raman spectra of flavocyt b_2 have been reported by Desbois and coworkers, together with a comparison of its heme and flavin RR frequencies with other enzymes and model compounds.[14] Although CDH shows no protein sequence similarity with flavocyt b_2, its heme and flavin domain organization and its spectral and biochemical properties are similar.[3]

In this study, the RR spectral characteristics of CDH are examined to further understand the molecular and electronic structural properties of the cofactors. In addition, the frequencies of specific vibrations associated with the chromophores can provide information on the local protein environment around the cofactors. Several forms of the enzyme were investigated in this study, including the fully oxidized protein (CDH_{ox}), the

protein reduced anaerobically with substrate (CDH_{red}), a flavin-free form of the enzyme (deflavo CDH), and the two isolated heme and flavin domains of CDH obtained by papain digestion of the holoenzyme. The data reported in this study reveal that the high-frequency regions of the RR spectra of CDH share many similarities with the spectra of flavocyt b_2 and other low-spin hemoproteins despite the differences in primary structure, and are typical for proteins containing heme and flavin cofactors. Also, RR studies using 413-nm excitation revealed that whereas the heme of CDH holoenzyme is highly susceptible to photoreduction, deflavo-CDH and the isolated heme domain are resistant to such photoreduction. This suggests that the FAD of CDH mediates electron transfer to the heme.

Materials and Methods

Preparation of CDH_{ox}, CDH_{red}, and flavin and heme domains. CDH was purified from cellulose-degrading cultures of *P. chrysosporium* by previously published methods.[3,17] Reduced CDH was prepared by adding 10 μL of 100 mM cellobiose to a 10 μL solution of 0.25 to 0.5 mM CDH_{ox} under argon. The flavin and heme domains were prepared by incubating homogeneous CDH_{ox} (3 mg) with papain (75 μg) in 0.1 M phosphate buffer (pH 7, 1 mL) containing 2 mM EDTA and 2 mM dithiothreitol for 3 h at room temperature.[9] Heme and flavin domains were separated from non-hydrolyzed CDH using a Sephacryl S-200 column (58 × 2.8 cm) equilibrated with 50 mM phosphate (pH 6). The heme and flavin domains were separated by fast protein liquid chromatography (FPLC) using a Mono-Q 5/5 column (Pharmacia). FPLC separations were performed in 10 mM Tris-HCl (pH 8) and proteins were eluted with a 1 M linear NaCl gradient. Fractions containing heme and flavin domains were analyzed by SDS-polyacrylamide gel electrophoresis (SDS-PAGE).

Preparation of deflavo CDH. CDH was incubated in 20 mM KCl-HCl (pH 2) for 2 h, at which time all the enzymatic activity was lost owing to the loss of FAD from the active site, as described previously.[3] The inactive CDH containing only the heme cofactor was separated from free FAD by ultrafiltration using a Centricon 30 microconcentrator

(Amicon Corp., Beverly, MA). The sample was dialyzed once against 20 mM KCl-HCl and twice against 20 mM succinate, pH 4.5. Finally, the dialyzed deflavo CDH was concentrated and used in spectroscopic experiments.

Spectroscopy. Electronic absorption spectra were measured on a Perkin-Elmer Lambda-9 spectrophotometer on ~10 μL of each sample sealed in a glass melting-point capillary tube (o.d. ≈ 1.8 mm).[18] Resonance Raman spectra of the same samples were collected on a modified Jarrell-Ash model 25-300 Raman spectrophotometer equipped with a cooled (-40 °C) Hamamatsu 943-02 photomultiplier tube and photon-counting electronics controlled by an Intel 310 computer. Typical scans were acquired at 1 cm^{-1}/s at 5 cm^{-1} resolution. Resonance Raman spectra of the isolated domains were obtained on a custom McPherson 2061/207 spectrograph equipped with a Princeton Instruments LN1100PB liquid-N_2-cooled CCD detector, Kaiser Optical Systems holographic notch filters, and interfaced to a Gateway 486 PC. Excitation light was provided by a Liconix He-Cd (442 nm), a Spectra Physics 302 Kr^+ (413 nm), or a Spectra Physics 164 Ar^+ (514.5 nm) laser. Typical power levels at the sample in these experiments were 10-35 mW. Plasma emission lines were removed by an Applied Photophysics prism monochromator. Data were collected in a 90°-scattering geometry with the sample capillaries at ~277 K placed in a copper cold finger that was chilled in a metal Dewar filled with an ice/water mixture.[18] Spectral data were processed using GRAMS/386 (Galactic Industries) and Origin (MicroCal) data analysis programs. Spectra were calibrated against indene and/or CCl_4 as external standards. Frequencies are estimated to be accurate to ±2 cm^{-1}.

Results and Discussion

Electronic spectra of CDH holoprotein and isolated domains. In the fully oxidized state, the heme and flavin cofactors of CDH both absorb in the visible region. The electronic absorption spectrum of CDH_{ox} has ferric heme maxima at 420, 529, and 570 nm with absorptivities of 99.8, 10.1, and 7.0 $mM^{-1}cm^{-1}$, respectively.[3] Evidence of flavin absorbance is seen in the oxidized form by the tailing of the Soret band between 430 and

500 nm.[3] Reduction by substrate shifts the heme absorption maxima to 428, 534, and 564 nm with absorptivities of 139.5, 12.7, and 22.7 $mM^{-1}cm^{-1}$, respectively.[3] However, the visible absorption of the flavin group is eliminated in the reduced form when the FAD is converted to $FADH_2$.

The electronic absorption spectra of the isolated domains are shown in Figure 4-1. The spectrum of the oxidized heme domain has absorption maxima at 419, 531, and ~565 nm (Fig. 4-1C). These values are within 1-2 nm of the λ_{max} of CDH_{ox}, except that the weak shoulder of the α-band appears to be ~5 nm blue shifted. When reduced with cellobiose, the absorption maxima of the heme domain shift to 430, 531, and 563 nm (Fig. 4-1A), values that are within 1 to 3 nm of the λ_{max} of CDH_{red}. Clearly, proteolysis of CDH does not affect its heme electronic transitions, suggesting that the heme and flavin domains are spectroscopically independent units. However, the absorption maxima of the oxidized flavin domain at ~384 and 458 nm (Fig. 4-1B) are significantly red-shifted from the reported values of 370 and 450 nm of the free flavin moiety,[3] indicating the influence of the protein on this chromophore.

Resonance Raman spectra of CDH. Both the heme and the oxidized flavin cofactors are resonance-Raman-active chromophores, and can undergo enhancement of vibrational modes with laser excitation in the 400-500 nm range.[15,16] The RR spectra of CDH_{ox}, deflavo CDH_{ox}, and CDH_{red} obtained with 442-nm excitation are shown in Figure 4-2. This wavelength simultaneously enhances vibrational modes of the oxidized forms of heme and FAD; hence, the observed spectra are complicated by the superposition of their rich and intense vibrational bands (Fig. 4-2A). However, either a change in the excitation wavelength or the elimination of the flavin chromophore from the protein by removal (deflavo-CDH; Figs. 4-2B and 4-3B) or by reduction to the non-chromophoric $FADH_2$ (Figs. 4-2C and 4-3C) allows one to obtain the heme RR spectrum unencumbered by that of the flavin. Moreover, the proteolytic cleavage of CDH into its separate heme and flavin domains also allows the study of one chromophore independent of the other (Figs. 4-4 and 4-5). The spectral properties of the individual components as well as evidence of interaction between them are presented below.

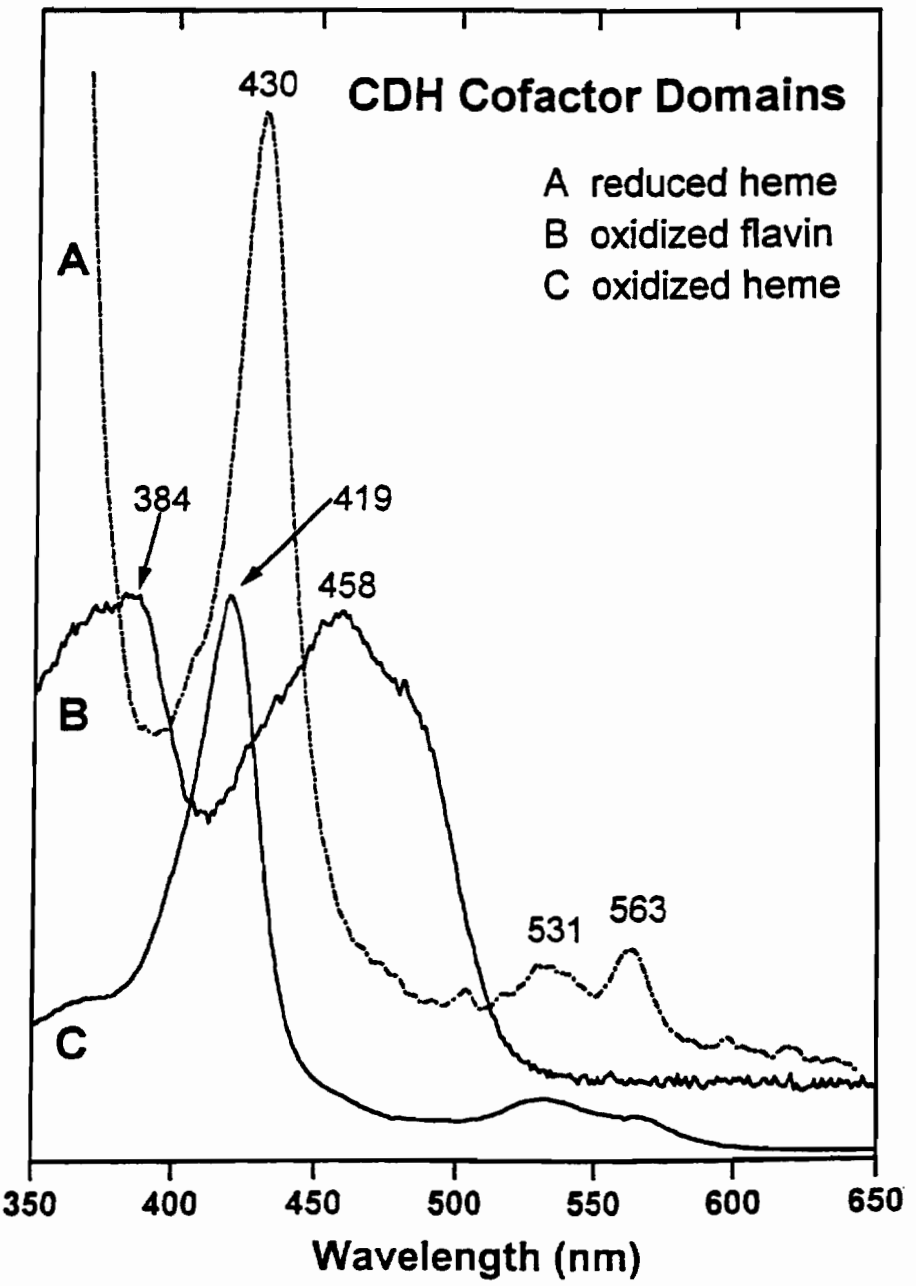

Figure 4-1. Electronic absorption spectra of isolated CDH domains. (A) Ferrous heme domain, $\varepsilon_{430} \approx 140\ mM^{-1}cm^{-1}$. (B) Oxidized FAD domain, $\varepsilon_{458} \approx 11.7\ mM^{-1}cm^{-1}$. (C) Ferric heme domain, $\varepsilon_{419} \approx 100\ mM^{-1}cm^{-1}$.

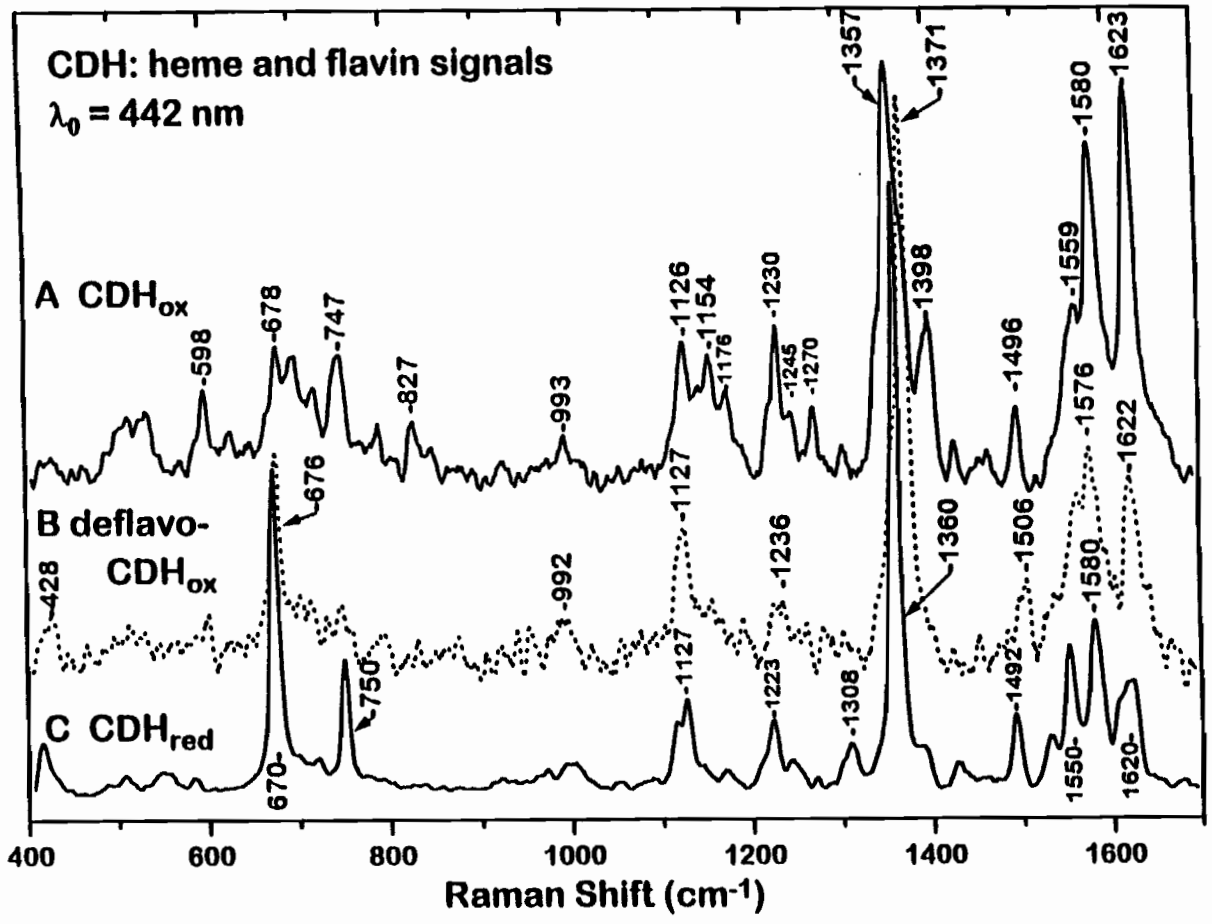

Figure 4-2. Resonance Raman spectra of CDH using 442-nm excitation. (A) CDH_{ox}, 0.25 mM, 35 mW laser power at the sample, 5 scans. (B) deflavo-CDH, 0.25 mM, 25 mW, 5 scans. (C) CDH_{red}, 0.25 mM, 30 mW, 6 scans.

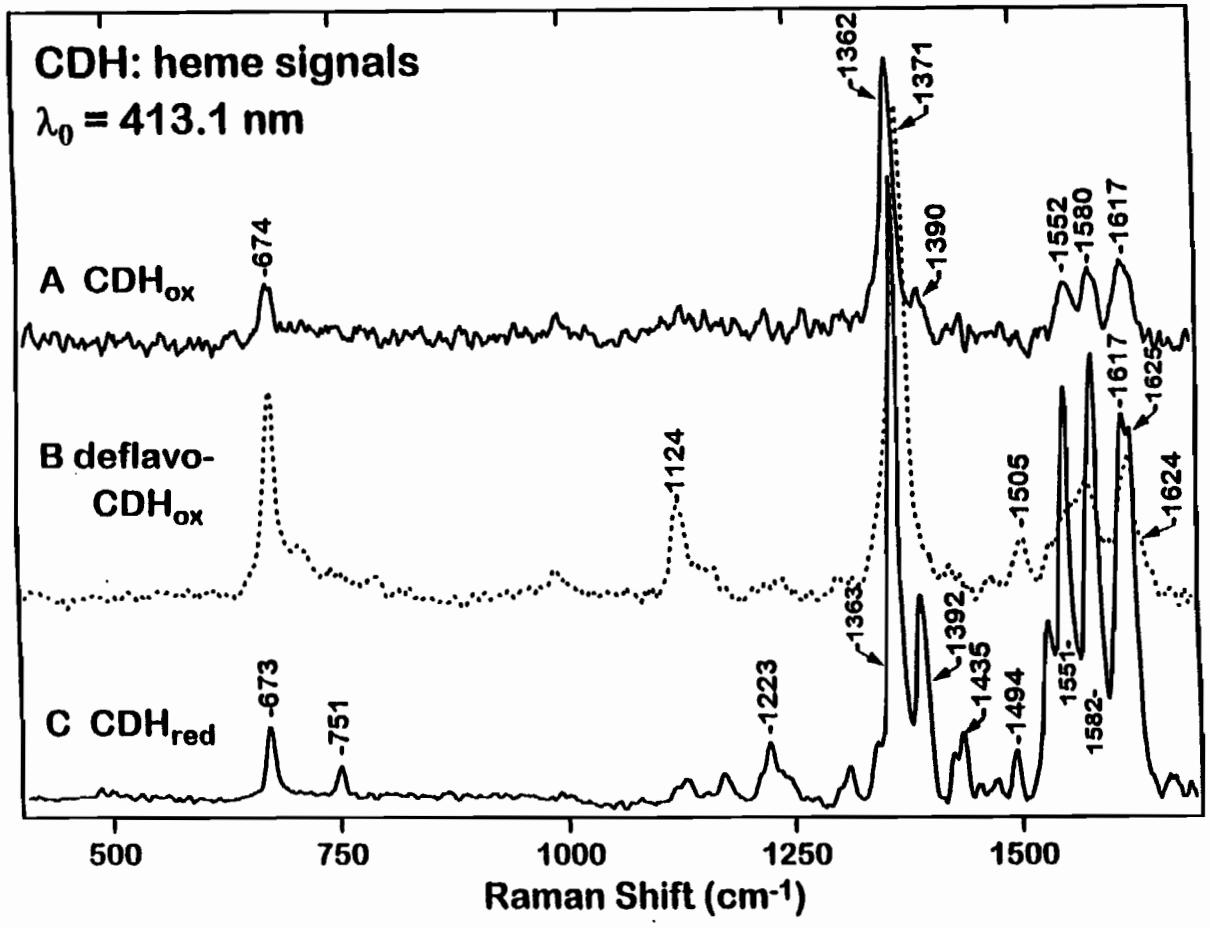

Figure 4-3. Resonance Raman spectra of CDH using 413-nm excitation. (A) CDH_{ox}, 0.25 mM, 25 mW at the sample, 5 scans. (B) deflavo-CDH, 0.25 mM, 25 mW, 5 scans. (C) CDH_{red}, 0.25 mM, 25 mW, 5 scans.

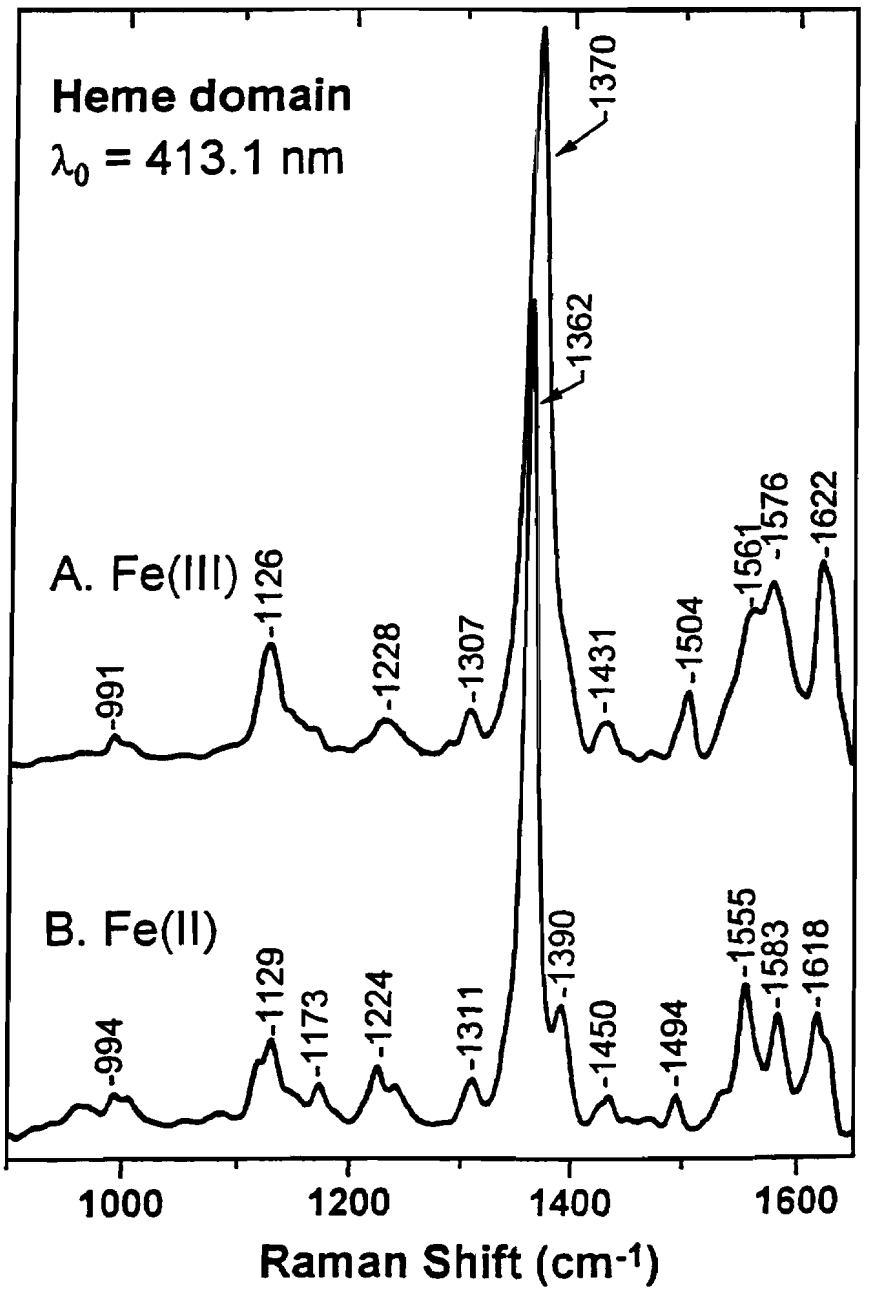

Figure 4-4. Resonance Raman spectra of CDH heme domain using 413-nm excitation. (A) Ferric CDH heme domain, 0.21 mM, 25 mW at the sample, 600 s exposure time. (B) Ferrous CDH heme domain (reduced with 100 mM cellobiose), 0.25 mM, 25 mW, 600 s exposure time.

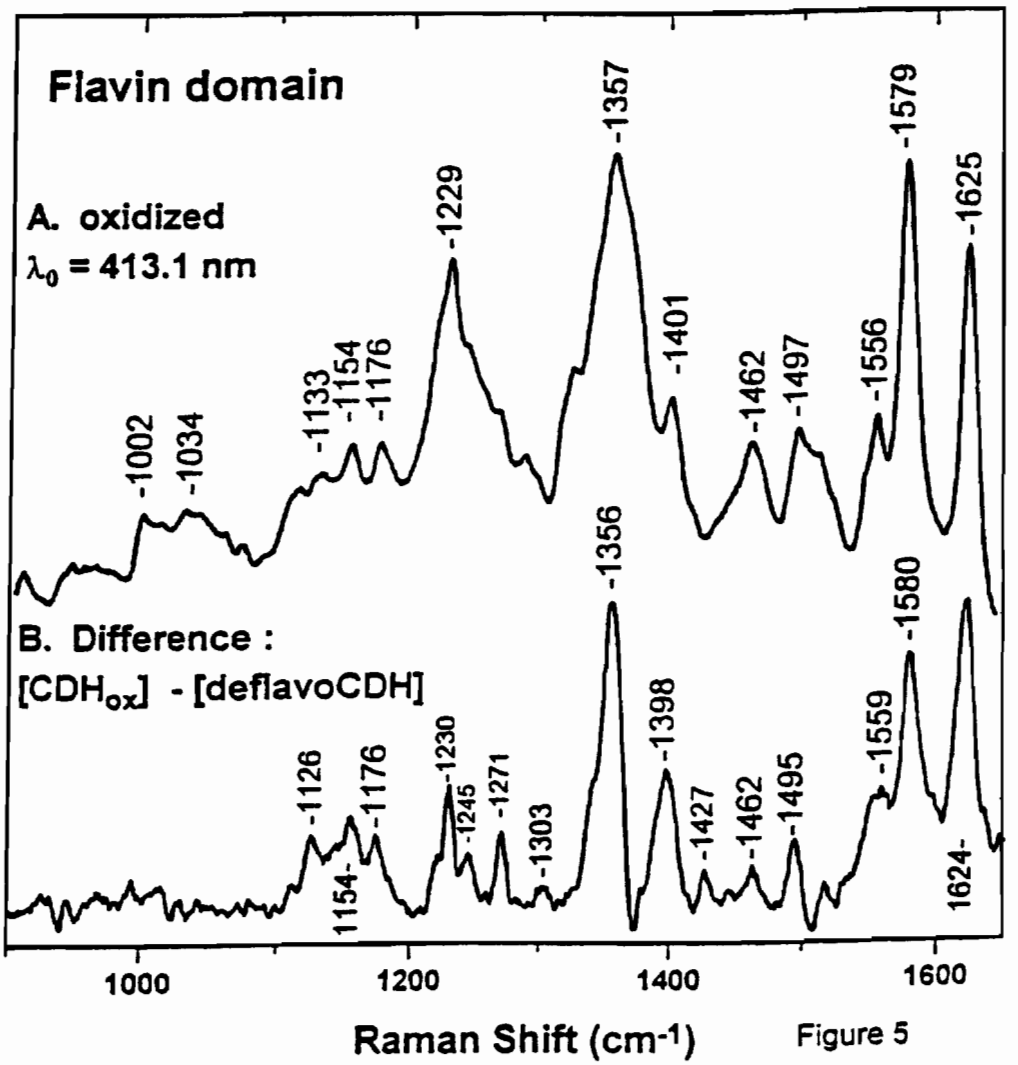

Figure 5

Figure 4-5. (A) Resonance Raman spectrum of the CDH flavin domain, 0.25 mM, 413 nm, 15 mW at the sample, 600 s exposure time. (B) Difference spectrum: [CDH_{ox}] – [deflavoCDH_{ox}], data from Figure 4-2, obtained with 442-nm excitation; this difference spectrum is equivalent to that for "pure" flavin.

Resonance Raman spectrum of the FAD Cofactor in CDH. The vibrational spectra of the flavin chromophore have received much attention from extensive studies of free and protein-bound flavins.[14,19-29] Their resonance Raman spectra are well understood as a result of normal mode analysis of the isoalloxazine ring system,[30-32] as well as isotopic[33] and site modifications[22,34] that have led to assignments of their spectra.

A large amount of flavin RR spectral data is summarized in Table 4-1. These data show that bands I - XIII lie within narrow ranges for a large variety of free flavins and many flavoproteins. Ten of the 13 bands are within 1 to 16 cm^{-1}; for only three the range spanned is between 18 and 25 cm^{-1}. Such variations in the vibrational frequencies of the flavin chromophores are generally interpreted in terms of specific interactions of the isoalloxazine ring system with the solvent and/or the protein[14,25,27] The spectrum of the flavin domain of CDH (recorded with 413-nm excitation; Fig. 4-5A) gives an excellent match in both frequencies and intensities to these representative values. A second example of the CDH flavin spectrum was obtained by difference spectroscopy. By subtracting the spectrum of the deflavo-CDH from that of CDH_{ox}, the RR spectrum of the FAD cofactor was obtained (Fig. 4-5B) from the component spectra of the intact protein using 442-nm excitation, as shown in Fig. 4-2A and 4-2B, respectively. This difference spectrum is a good match to the FAD spectrum obtained from the isolated domain; in fact, all of the characteristic high-frequency flavin modes are observed. The general correspondence of the resonance Raman spectrum of the FAD cofactor of CDH to previously studied flavin spectra reflects the structural similarities of the cofactor in these systems. Furthermore, despite the strong redshift of λ_{max} for the isolated flavin domain, the RR spectrum of this domain is quite similar to that of the FAD cofactor of the intact protein obtained by difference spectroscopy (Table 4-1).

Protein Effects on Flavin Modes. Redox active flavoproteins can be classified as either electron transferases, (e.g., flavodoxins) or oxidoreductases (e.g., CDH, flavocyt b_2, and NADPH:cytochrome P-450 reductase). The flavodoxin class can be further subdivided into type-A and type-B flavodoxins, based on their physical and chemical properties.[35,36]

Table 4-1: Resonance Raman Frequencies (cm^{-1}) and Assignments of the Flavin Modes of CDH_{ox}, Flavin Domain of CDH, Flavocytochrome b_2, and Observed Frequency Ranges of Flavins and Flavoproteins.

CDH_{ox} 442 nm[a]	[CDHox] (–) [deflavoCDH][a,b] difference	flavin domain 413 nm[a]	flavocyt b_2[3+,c]	observed range for flavins[d]	mode[e]	band label[f]	typical intensity[g]
1623	1624	1625	1629	1624-1635	ν_6	I	s to vs
1580	1580	1579	1581	1576-1585	ν_8	II	m to s
1559	1559	1556	1557	1531-1556	ν_9	III	w
1496	1495	1497	1501	1497-1508	ν_{10}	IV	m
1464	1462	1462	1463	1446-1467	ν_{11}	V	w to m
1426	1427						
1398	1398	1401		1403-1419	ν_{12}	VI	s
1357	1356	1357	1360	1348-1359	ν_{13}	VII	s to vs
1303	1304		1302	1302-1303	ν_{16}	VIII	w
1270	1271			1277-1295	ν_{17}	IX	m
1245	1245			1250-1257		X	m
1230	1230	1229	1231	1225-1233	ν_{19}	XI	m
1176	1176	1176	1180	1176-1192	ν_{20}	XII	w to m
1154	1154	1154		1158-1170	ν_{21}	XIII	m
1126	1126	1133	1131		ν_{22}		

[a]This work. [b]The difference spectrum corresponds to the contribution from the flavin moiety alone; see Figure 5B.

[c] Ref. 15. [d]The frequency ranges are for aqueous flavins and a variety of flavoproteins Ref.. 28, with data from Refs. 21,24,26-28,46,47. [e]Flavin mode numbering is from Ref. 33. [f]Band labels are from Ref. 32. [g]m, medium; s, strong; w, weak; v, very.

When flavins are protein-bound, the positions of a number of vibrational bands are shifted relative to those of free flavins in H_2O, and these shifts have been ascribed to hydrophobic interactions within the flavin binding pocket as well as hydrogen bonding to the isoalloxazine moiety of the cofactor.[22,25,26] Desbois et al.[14] reasoned that flavoproteins catalyzing similar reactions should have similar flavin binding pockets and, consequently, their RR spectra should display similar frequency shifts relative to free flavins. These authors searched for a correlation between biological function of flavoproteins and RR frequency deviations. Interestingly, they found that the pattern of frequency shifts of flavocyt b_2 was more similar to those of the A- and B-type flavodoxins than to those of oxidases and reductases. The latter exhibited no discernible pattern. We have now compared the flavin frequencies of CDH to those of other flavoproteins. While there is a superficial similarity in the RR behavior between CDH and flavocyt b_2, they differ in detail and show that frequency shifts of flavin cofactors do not appear to be compelling indicators of either enzyme function or local protein environments.

Resonance Raman spectrum of the Heme Cofactor in CDH. As mentioned above, excitation of CDH_{ox} at 442 nm enhances the vibrational modes of the oxidized forms of heme and FAD (Fig. 4-2A). However, the RR spectra of the deflavo-CDH (Fig. 4-2B) and the reduced enzyme, having a ferrous heme *b* and $FADH_2$ (Fig. 4-2C), show only bands arising from the heme chromophore. In deflavo-CDH, the most intense RR band is at 1371 cm^{-1}. This band is the so-called oxidation-state marker, ν_4, and this frequency is diagnostic of an oxidized (ferric) heme.[16,37,38] Reduction of the heme by substrate shifts ν_4 to ~1360 cm^{-1} (Fig. 4-2C). Nearly identical values of ν_4 are observed for the oxidized and reduced forms, respectively, when the excitation wavelength is shifted to 413 nm, closer to the Soret absorption (Fig. 4-3B and 4-3C).

The spin state of the heme iron is unambiguously low spin from the position of the core-size marker bands, ν_2 and ν_3. As seen in Figures 4-2 and 4-3, these values are ~1576 and 1506 in the oxidized heme and 1580 and 1493 cm^{-1} in the reduced heme. These values compare very favorably with ν_2 and ν_3, respectively, of *bis*-imidazole complexes of Fe(protoporphyrin). For $[Fe^{III}(PP)(Im)_2]Cl$, reported values are 1579 and 1502 cm^{-1} and

for the reduced complex, $Fe^{II}(PP)(Im)_2$, 1584 and 1493 cm^{-1}.[39] Similar values were observed for flavocyt b_2^{2+}.[14] Frequencies for the reduced forms of CDH and comparisons with some literature values are given in Table 4-2.

The low-spin *b*-type hemes in cytochrome b_5 and flavocyt b_2 have histidines as axial ligands.[11] In contrast, low-spin *c*-type hemes such as in cytochrome *c* have histidine and methionine as axial ligands. Although resonance Raman spectroscopy cannot distinguish between the nature of the axial ligands in these two classes of low-spin hemes,[40] MCD spectroscopy is ideally suited for this task.[41] In their study of CDH, Thomson and coworkers assigned a His/Met coordination environment to this low-spin *b*-type heme.[10] Thus, both spectral techniques confirm that the heme in CDH is a six-coordinate, low spin system.

Protein Effects on Heme Modes. The resonance Raman spectra of the oxidized and reduced forms of the isolated heme domain obtained with 413-nm excitation are shown in Figure 4-4. With ν_4 at 1370 cm^{-1}, and the spin-state markers ν_2 and ν_3 at 1576 and 1504 cm^{-1}, respectively, the isolated Fe(III) heme is clearly in a six-coordinate low-spin state. These values shift to 1362, 1583, and 1494 cm^{-1} in the reduced (ferrous) heme domain. As expected, the latter spectrum is essentially identical to those observed for CDH_{red} shown in Figures 4-2C and 4-3C, with only some intensity differences arising from the use of different samples and different spectrometers. However, an interesting fact emerges when the RR spectrum of the oxidized heme domain (Fig. 4-4A) is compared to those of CDH_{ox} and deflavo-CDH_{ox} (Figs. 2 and 3). In CDH_{ox}, the most intense feature at 1357 cm^{-1} is due to the superposition of ν_4 of the heme with ν_{15} (band VII) of the flavin. With Soret excitation, ν_4 is generally the most intense RR band. However, the fact that the most intense peak in CDH_{ox} is at ~1360 cm^{-1} with both 442- and 413-nm excitation (Figs. 2A and 3A) indicates that the heme is reduced. The RR spectra of CDH_{ox} show no significant intensity at ~1370 cm^{-1} expected for ν_4 of a ferric heme, thus, indicating the presence of a ferrous heme in these samples. Although photoreduction of hemes is frequently observed, the present data illustrate that photoreduction only occurs in the presence of FAD. To illustrate, the spectra of deflavo-CDH (Fig. 4-2B and 4-3B) and isolated heme domain (Fig. 4-4A) display ν_4 bands at 1371 cm^{-1} indicative of ferric heme.

Table 4-2: Resonance Raman Frequencies (cm^{-1}) and assignments of the Heme Modes of CDH, Heme Domain of CDH, Flavocytochrome b_2, and $Fe^{II}PP(Im)_2$.

CDH_{red} 442 nm[a]	CDH_{red} 413 nm[a]	CDH_{red} 514 nm[a]	heme domain[a]	flavocyt b_2^{2+},[b]	$Fe^{II}PP(Im)_2$[c]	assignmt[d]
1622	1617	1624	1618	1620	1617	v10
1581	1582	1586	1583	1580	1584	v2
1552	1551		1555	1556	1560	v38
1530	1531	1531		1536	1539	v11
1492	1493	1493	1494	1493	1493	v3
1427	1433					
1388	1391	1400	1390	1388	1392	v20
1360	1363	1362	1362	1361	1359	v4
1243						
1223	1223	1223	1224			
1169	1171	1173	1173			
1127	1129		1129	1131	1130	v6 + v8
1116		1117				
1051	1055	1054				
1003		1011	994			

[a]This work; the 514-nm spectrum is not shown. [b]Ref. 15. [c]Ref. 40. [d]Heme mode numbering is from Refs. 48,49.

This observation is consistent with a reaction mechanism where substrate is bound at or near the FAD and the reducing equivalents generated by the oxidation of cellobiose to cellobionolactone are transferred to the heme.

Flavin-mediated photoreduction in hemoflavoenzymes has been noted previously. Kitagawa and coworkers proposed inter-subunit electron transfer from flavin to heme in flavocytochrome c_{552} on the basis of RR evidence for reduced heme in the presence of the FAD.[24] Similarly, Desbois et al. showed that flavocyt b_2, a system closely related to CDH, is susceptible to photoreduction, whereas the heme domain obtained by trypsin digestion is more resistant.[14] Chapman and coworkers have identified key amino acids in flavocyt b_2 that form an interdomain hinge and are critical for both inter- and intramolecular electron transfer.[42-44] It is possible that a similar hinge mechanism is present in CDH. With the recent cloning and sequencing of CDH, efforts can now be made to identify the key amino acid residues involved in flavin binding, substrate reduction, and electron transfer between cofactors.

Acknowledgments

The authors are grateful for financial support through grants from the DOE and NIH. Purchase of instrumentation in the Raman spectroscopy laboratory was made possible, in part, by shared instrumentation grants from the National Institutes of Health (RR-02676) and the National Science Foundation (BIR-9216592). We thank Dr. Jie Sun and Dr. Joann Sanders-Loehr for helpful discussions.

References

(1) Renganathan, V.; Bao, W. "Cellobiose Dehydrogenase, A Hemoflavoenzyme from Phaerochaete chrysosporium—A Review;" in *Enzymatic Conversion of Biomass for Fuels Production*; Himmel, M. E.; Overend, R. P.; Baker, J. O.; Eds.; American Chemical Society: Washington, DC, 1994, pp. 179-185.

(2) Ayers, A. R.; Ayers, S. B.; Eriksson, K.-E. "Cellobiose Oxidase, Purification and Partial Characterization of a Hemoprotein from *Sporotrichum pulverulentum*." *Eur. J. Biochem.* **1978**, *90*, 171-181.

(3) Bao, W.; Usha, S. N.; Renganathan, V. "Purification and Characterization of Cellobiose Dehydrogenase, a Novel Extracellular Hemoflavoenzyme from the White-Rot Fungus *Phanerochaete chrysosporium*." *Arch. Biochem. Biophys.* **1993**, *300*, 705-713.

(4) Canevascini, G.; Borer, P.; Dreyer, J.-L. "Cellobiose Dehydrogenases of *Sporotrichum (Chrysosporium) thermophile*." *Eur. J. Biochem.* **1991**, *198*, 43-52.

(5) Kremer, S. M.; Wood, P. M. "Evidence that Cellobiose Oxidase from *Phanerochaete chrysosporium* is Primarily and Fe(III) Reductase--Kinetic Comparison with Neutrophil NADPH Oxidase and Yeast Flavocytochrome b_2." *Eur. J. Biochem.* **1992**, *205*, 133-138.

(6) Li, B.; Nagalla, S. R.; Renganathan, V. "Cloning of cDNA Encoding Cellobiose Dehydrogenase, a Hemoflavoenzyme from *Phanerochaete chrysosporium*." *Appl. Environ. Microbiol.* **1996**, *62*, 1329-1335.

(7) Bao, W. *Cellobiose Dehydrogenase--A Novel Hemoflovoenzyme from Phanerochaete chrysosporium*; Ph.D. Thesis; Oregon Graduate Institute: Portland, 1994.

(8) Raices, M.; Paifer, E.; Cremata, J.; Montesino, R.; Stahlberg, J.; Divne, C.; Szabo, I. J.; Henriksson, G.; Johansson, G.; Pettersson, G. "Cloning and Characterization of a cDNA Encoding a Cellobiose Dehydrogenase from the White Rot Fungus *Phanerochaete chrysosporium*." *FEBS Lett.* **1995**, *369*, 233-238.

(9) Henriksson, G.; Pettersson, G.; Johansson, G.; Ruiz, A.; Uzcategui, E. "Cellobiose Oxidase from *Phanerochaete chrysosporium* can be Cleaved by Papain into Two Domains." *Eur. J. Biochem.* **1991**, *196*, 101-106.

(10) Cox, M. C.; Rogers, M. S.; Cheesman, M.; Jones, G. D.; Thomson, A. J.; Wilson, M. T.; Moore, G. R. "Spectroscopic Identification of the Haem Ligands of Cellobiose Oxidase." *FEBS Lett.* **1992**, *307*, 233-236.

(11) Xia, Z. X.; Shamala, N.; Bethge, P. H.; Lim, L. W.; Bellamy, H. D.; Xuong, N. H.; Lederer, F.; Mathews, F. S. "Three-Dimensional Structure of Flavocytochrome b_2 from Baker's Yeast at 3.0-Å Resolution." *Proc. Natl. Acad. Sci. U.S.A.* **1987**, *84*, 2629-2633.

(12) Tabor, C. W.; Kellogg, P. D. "Identification of Flavin Adenine Dinucleotide and Heme in a Homogeneous Spermidine Dehydrogenase from *Serratia marcescens*." *J. Biol. Chem.* **1970**, *245*, 5424-5433.

(13) Pealing, S. L.; Black, A. C.; Manson, F. D.; Ward, F. B.; Chapman, S. K.; Reid, G. A. "Sequence of the Gene Encoding Flavocytochrome *c* from *Shewanella putrefaciens*: A Tetraheme Flavoenzyme that is a Soluble Fumarate Reductase Related to the Membrane-Bound Enzymes from Other Bacteria [published erratum appears in Biochemistry **1993**, *32*, 3829]." *Biochemistry* **1992**, *31*, 12132-12140.

(14) Desbois, A.; Tegoni, M.; Gervais, M.; Lutz, M. "Flavin and Heme Structures in Lactate:Cytochrome *c* Oxidoreductase: A Resonance Raman Study." *Biochemistry* **1989**, *28*, 8011-8022.

(15) McFarland, J. "Flavins;" in *Biological Applications of Resonance Raman Spectroscopy*; Spiro, T. G., Ed.; John Wiley & Sons: New York, 1987; Vol. 2, pp. 211-301.

(16) Spiro, T. G.; Li, X.-Y. "Resonance Raman Spectroscopy of Metalloporphyrins;" in *Biological Applications of Resonance Raman Spectroscopy*; Spiro, T. G., Ed.; John Wiley & Sons: New York, 1988; Vol. 3, pp. 1-39.

(17) Bao, W.; Lymar, E.; Renganathan, V. "Production of Cellobiose Dehydrogenase and β-Glucosidase by the Cellulose-Degrading Cultures of *Phanerochaete chrysosporium* in Shake Flasks." *Appl. Microbial Biotechnol.* **1994**, *42*, 642-646.

(18) Loehr, T. M.; Sanders-Loehr, J. "Technique for Obtaining Resonance Raman Spectra of Metalloproteins." *Methods Enzymol.* **1993**, *226*, 431-470.

(19) Dutta, P. K.; Nestor, J.; Spiro, T. G. "Resonance Coherent Anti-Stokes Raman Scattering (CARS) Spectra of Flavin Adenine Dinucleotide, Riboflavin Binding Protein and Glucose Oxidase." *Biochem. Biophys. Res. Commun.* **1978**, *83*, 209-216.

(20) Benecky, M.; Li, T. Y.; Schmidt, J.; Frerman, F.; Watters, K. L.; McFarland, J. "Resonance Raman study of Flavins and the Flavoprotein Fatty Acyl Coenzyme A Dehydrogenase." *Biochemistry* **1979**, *18*, 3471-3476.

(21) Ondrias, M. R.; Findsen, E. W.; Leroi, G. E.; Babcock, G. T. "Chromophore Interactions in Flavocytochrome c_{552}: A Resonance Raman Investigation." *Biochemistry* **1980**, *19*, 1723-1730.

(22) Nishina, Y.; Shiga, K.; Horiike, K.; Tojo, H.; Kasai, S.; Yanase, K.; Matsui, K.; Watari, H.; Yamano, T. "Vibrational Modes of Flavin Bound to Riboflavin Binding Protein from Egg White. Resonance Raman Spectra of Lumiflavin and 8-Substituted Riboflavin." *J. Biochem. (Japan)* **1980**, *88*, 403-409.

(23) Irwin, R. M.; Visser, A. J.; Lee, J.; Carreira, L. A. "Protein-Ligand Interactions in Lumazine Protein and in *Desulfovibrio* flavodoxins from Resonance Coherent Anti-Stokes Raman Spectra." *Biochemistry* **1980**, *19*, 4639-4646.

(24) Kitagawa, T.; Fukumori, Y.; Yamanaka, T. "Resonance Raman Evidence for Intramolecular Electron Transport from Flavin to Heme in Flavocytochrome *c*-552 and Nature of Chromophoric Interactions." *Biochemistry* **1980**, *19*, 5721-5729.

(25) Visser, A. J.; Vervoort, J.; O'Kane, D. J.; Lee, J.; Carreira, L. A. "Raman Spectra of Flavin Bound in Flavodoxins and in Other Flavoproteins. Evidence for Structural Variations in the Flavin-Binding Region." *Eur. J. Biochem.* **1983**, *131*, 639-645.

(26) Schmidt, J.; Coudron, P.; Thompson, A. W.; Watters, K. L.; McFarland, J. T. "Hydrogen Bonding Between Flavin and Protein: a Resonance Raman Study." *Biochemistry* **1983**, *22*, 76-84.

(27) Sugiyama, T.; Nisimoto, Y.; Mason, H. S.; Loehr, T. M. "Flavins of NADPH-Cytochrome P-450 Reductase: Evidence for Structural Alteration of Flavins in their One-Electron-Reduced Semiquinone States from Resonance Raman Spectroscopy." *Biochemistry* **1985**, *24*, 3012-3019.

(28) Willis, L. J.; Loehr, T. M. "Resonance Raman Studies of the Flavin and Iron-Sulfur Centers of Milk Xanthine Oxidase." *Biochemistry* **1985**, *24*, 2768-2772.

(29) Nishina, Y.; Miura, R.; Tojo, H.; Miyake, Y.; Watari, H.; Shiga, K. "A Resonance Raman Study on the Structures of Complexes of Flavoprotein D-Amino Acid Oxidase." *J. Biochem. (Japan)* **1986**, *99*, 329-337.

(30) Bowman, W. D.; Spiro, T. G. "MNDO-MOCIC Evaluation of the Uracil Force Field: Application to the Interpretation of Flavin Vibrational Spectra." *J. Chem. Phys.* **1980**, *73*, 5482-5492.

(31) Bowman, W. D.; Spiro, T. G. "Normal Mode Analysis of Lumiflavin and Interpretation of Resonance Raman Spectra of Flavoproteins." *Biochemistry* **1981**, *20*, 3313-3318.

(32) Abe, M.; Koyogoku, Y. "Vibrational Analysis of Flavin Derivatives: Normal Coordinate Treatments of Lumiflavin." *Spectrochim. Acta* **1987**, *43A*, 1027-1037.

(33) Kitagawa, T.; Nishina, Y.; Kyogoku, Y.; Yamano, T.; Ohishi, N.; Takai-Suzuki, A.; Yagi, K. "Resonance Raman Spectra of Carbon-13- and Nitrogen-15-Labeled Riboflavin Bound to Egg-White Flavoprotein." *Biochemistry* **1979**, *18*, 1804-1808.

(34) Schopfer, L. M.; Haushalter, J. P.; Smith, M.; Milad, M.; Morris, M. D. "Resonance Raman Spectra for Flavin Derivatives Modified in the 8 Position." *Biochemistry* **1981**, *20*, 6734-6739.

(35) King, T. E., Mason, H. S.; Morrison, M.; Eds. *Oxidases and Related Redox Systems*; Pergamon: Oxford, 1982, pp. 379-405.

(36) Tollin, G.; Edmondson, D. *Methods Enzymol.* **1980**, *69*, 392-406.

(37) Mino, Y.; Wariishi, H.; Blackburn, N. J.; Loehr, T. M.; Gold, M. H. "Spectral Characterization of Manganese Peroxidase, an Extracellular Heme Enzyme from the Lignin-Degrading Basidiomycete, *Phanerochaete chrysosporium*." *J. Biol. Chem.* **1988**, *263*, 7029-7036.

(38) Andersson, L. A.; Mylrajan, M.; Loehr, T. M.; Sullivan, E. P., Jr.; Strauss, S. H. "Modeling Biological Iron Hydroporphyrins: Comparative Resonance Raman Spectroscopy." *New J. Chem.* **1992**, *16*, 569-576.

(39) Choi, S.; Spiro, T. G.; Langry, K. C.; Smith, K. M.; Budd, D. L.; La Mar, G. N. "Structural Correlations and Vinyl Influences in Resonance Raman Spectra of Protoheme Complexes and Proteins." *J. Am. Chem. Soc.* **1982**, *104*, 4345-4351.

(40) Hu, S.; Morris, I. K.; Singh, J. P.; Smith, K. M.; Spiro, T. G. "Complete Assignment of Cytochrome *c* Resonance Raman Spectra via Enzymatic Reconstitution with Isotopically Labeled Hemes." *J. Am. Chem. Soc.* **1993**, *115*, 12446-12458.

(41) Gadsby, P. M. A.; Thomson, A. J. "Assignment of the Axial Ligands of Ferric Ion in Low-Spin Hemoproteins by Near-Infrared Magnetic Circular Dichroism and Electron Paramagnetic Resonance Spectroscopy." *J. Am. Chem. Soc.* **1990**, *112*, 5003-5011.

(42) Sharp, R. E.; White, P.; Chapman, S. K.; Reid, G. A. "Role of the Interdomain Hinge of Flavocytochrome b_2 in Intra- and Inter-Protein Electron Transfer." *Biochemistry* **1994**, *33*, 5115-5120.

(43) Sharp, R. E.; Chapman, S. K.; Reid, G. A. "Deletions in the Interdomain Hinge Region of Flavocytochrome b_2: Effects on Intraprotein Electron Transfer." *Biochemistry* **1996**, *35*, 891-899.

(44) Miles, C. S.; Rouviere, F.-N.; Lederer, F.; Mathews, F. S.; Reid, G. A.; Black, M. T.; Chapman, S. K. "Tyr-143 Facilitates Interdomain Electron Transfer in Flavocytochrome b_2." *Biochem. J.* **1992**, *285*, 187-192.

(45) Nishimura, Y.; Tsuboi, M. *Chem. Phys. Lett.* **1978**, *59*, 210-213.

(46) Copeland, R. A.; Spiro, T. G. "Ultraviolet Resonance Raman Spectroscopy of Flavin Mononucleotide and Flavin Adenine Dinucleotide." *J. Phys. Chem.* **1986**, *90*, 6648-6654.

(47) Abe, M.; Kitagawa, T.; Koyogoku, Y. "Resonance Raman Spectra of Octaethylporphyrinato-Ni(II) and *meso*-Deuterated and ^{15}N Substituted Derivatives. II. A Normal Coordinate Analysis." *J. Chem. Phys.* **1978**, *69*, 4526-4534.

(48) Kitagawa, T.; Abe, M.; Ogoshi, H. "Resonance Raman Spectra of Octaethylporphyrinato-Ni(II) and *meso*-Deuterated and ^{15}N Substituted Derivatives. I. Observation and Assignments of Nonfundamental Raman Lines." *J. Chem. Phys.* **1978**, *69*, 4516-4525.

Chapter 5

Kinetics of Rapid Iron Uptake by Wild-type and Mutant Ferritin. RR Detection of [Fe-Tyr] Intermediates[1]

Abstract

Ferritin is a ubiquitous protein that sequesters Fe^{2+} and oxidizes it for storage as a ferrihydrite-like mineral. Previous studies on wild-type frog H-chain homopolymers have identified an [Fe-Tyr] intermediate during initial Fe uptake with a characteristic electronic and resonance Raman spectrum. Resonance Raman spectra of samples of wild-type and mutant (Y25F, Y28F, and Y30F) FTN-H homopolymers demonstrated that these isoforms successfully formed the [Fe-Tyr] intermediate when incubated with 1 Fe^{2+}/subunit and exposed to air. Thus, the tyrosines at positions 25, 28, and 30 do not appear to be the sites of the [Fe-Tyr] intermediate. In addition, samples of wild-type and mutant apoFTN-H, -M, and -L were mixed with 1 Fe^{2+}/subunit and excess O_2 and the half-life of decay of the [Fe-Tyr] intermediate was measured. For wild-type FTN-H, the half-life measured by the decrease of absorbance at 550 nm (28 s) was within 1 s of that measured by the ratio of I_{1600}/I_{1650} from RR spectroscopy, demonstrating that the two analytes are the same. The decay half-life increased 3-4 fold in the Y25F, Y28F, and Y30F FTN-H mutants, indicating that protein structure does affect the rate of decay. Samples of H25Y FTN-L failed to form the [Fe-Tyr] intermediate. Wild-type FTN-M (lacking Y36 and Y147) has a 650-nm intermediate that can be observed by stopped-flow spectroscopy, but which forms and decays too rapidly to be observed by RR spectroscopy. A similar intermediate is detected

in wild-type human FTN-H. These results suggest that Y36, Y133, or Y147 is responsible for the 550-nm [Fe-Tyr] intermediate in frog FTN-H but that a different tyrosine residue (Y30 or Y34) may be responsible for the 650-nm intermediate in frog FTN-M and human FTN-H.

Introduction

As organisms evolved from primitive bacteria to the wide variety of animal and plant species thriving today, many life-sustaining chemical reactions would not be possible without a readily available supply of iron.[2] However, in the presence of O_2 or other oxidants, cellular Fe^{2+} levels must be carefully regulated in order to prevent adventitious reactions that could produce reactive oxygen species toxic to the cell.[3] To perform this iron housekeeping task, organisms from bacteria to humans produce ferritin (FTN), an iron storage protein whose role is to reversibly sequester iron in a mineralized form.[4,5]

The primary structure of several vertebrate FTN subunits have been reported (Table 5-1, the numbering scheme used in this table is according to the horse spleen FTN-L sequence).[6] All FTN isoforms are composed of ~175 amino acids per monomer with a mass of ~20 kD. Ferritin isoforms from frogs are denoted FTN-H, -M, or -L based on their relative electrophoretic mobilities in SDS gels.[7] The amino acid sequence of corresponding isoforms from different species are up to 93% homologous, implying a conserved three-dimensional structure for all ferritins.

In vivo, FTN forms 24-subunit heteropolymers of varying composition.[8] For instance, horse spleen ferritin (HoSF) contains ~15% FTN-H and the remainder FTN-L. To facilitate biochemical studies, the genes for human and frog FTN subunits have been cloned and overexpressed in *E. coli*, facilitating the production of FTN homopolymers composed of a single subunit type.[9,10]

FTN 24-mers self-assemble into spherical particles with 432 symmetry and an 8-nm-diameter hollow cavity (Fig. 5-1). The central cavity of FTN can hold up to 4500 Fe atoms as a polymerized mineral aggregate. EXAFS,[11] electron diffraction,[12] and synthetic model studies[13,14] show that ferritin cores have a highly polymorphous FeO(OH) structure

Table 5-1: Amino acid sequences of several vertebrate ferritins.[a]

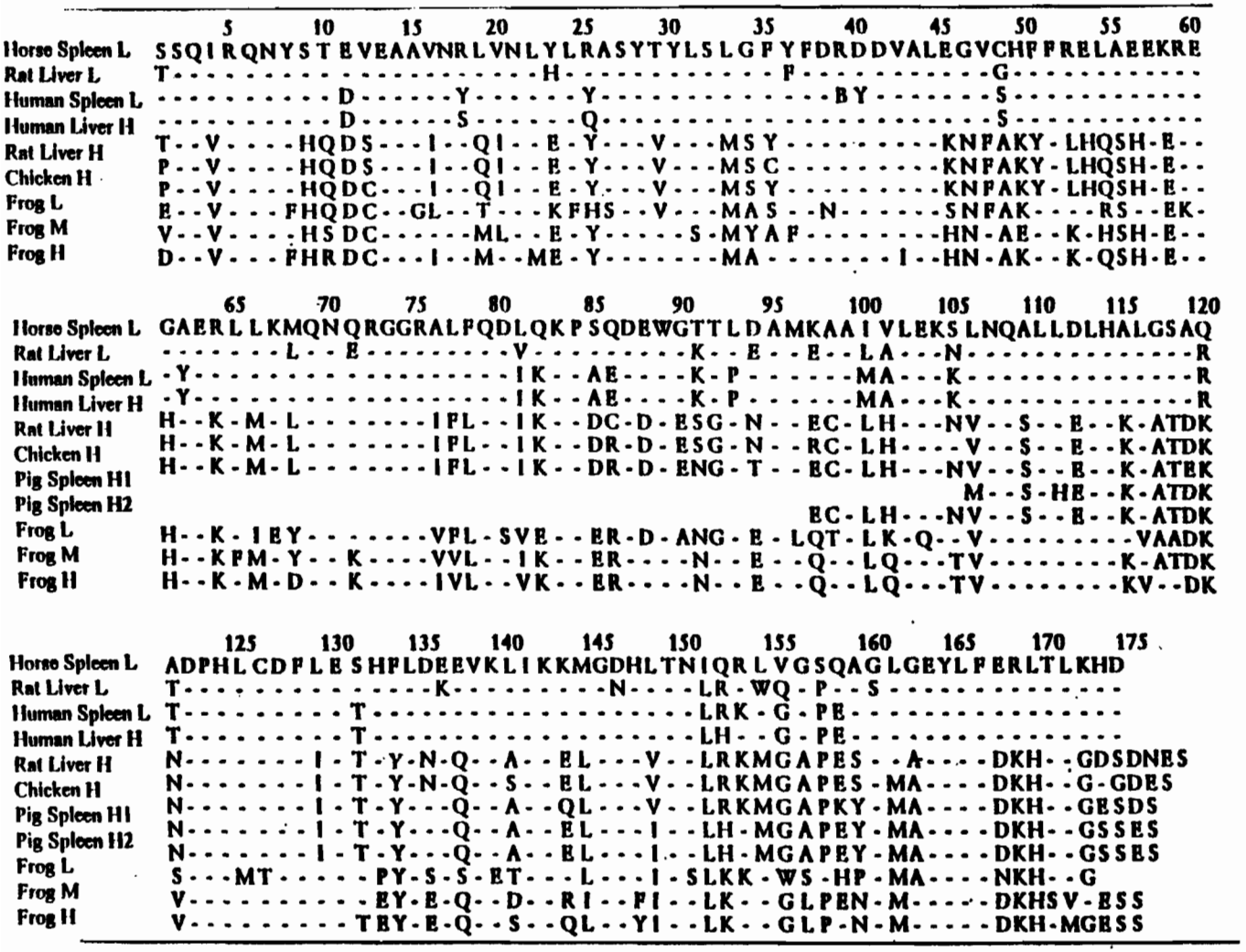

[a]Adapted from reference 6.

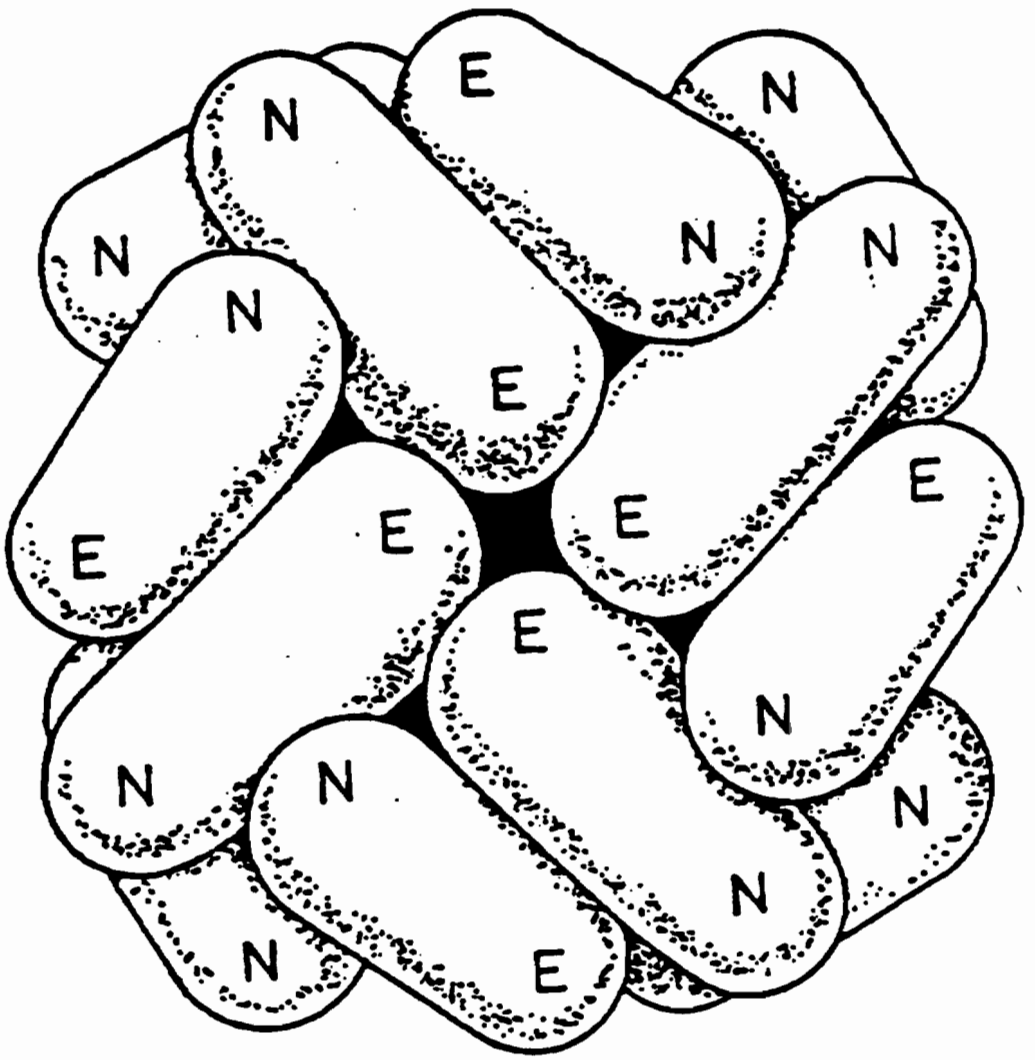

Figure 5-1. Schematic diagram of an idealized ferritin 24-subunit homopolymer viewed perpendicular to the 4-fold symmetry axis. Each subunit is represented by equivalent ellipsoids where N is the N-terminal end of the subunit and E is the E-helix (C-terminal) end. Adapted from reference 6.

similar to ferrihydrite, with a variable phosphate content of 1/8 to 1 per Fe. Xu and coworkers have proposed that core growth can proceed directly on the growing mineral surface and/or by active participation of the protein.[15] Both mechanisms utilize O_2 as the oxidant and release 2-4 protons per Fe^{3+} mineralized.[5,15]

X-ray crystal structures of FTN homopolymers have been reported by three groups.[16-20] The subunit secondary structure conserved in all ferritins is a modified 4-α-helix bundle approximately 25×25×50 $Å^3$ (Fig. 5-2). A β-strand spans the length of the bundle connecting helices B and C and a shorter C-terminal α-helical segment (helix E) runs roughly perpendicular to the bundle. The structure of the K86Q mutant of human FTN-H crystallized with $TbCl_3$ has been solved to 1.9-Å resolution, revealing a dinuclear metal site embedded near the center of the 4-α-helix.[16] The proposal that the Tb^{3+} sites are normally occupied by Fe^{3+} *in vivo* is supported by the structure of *E. coli* FTN crystals soaked in $(NH_4)_2Fe(SO_4)_2$ at 2.9-Å resolution, showing two Fe^{3+} ions bound to positions similar to those found in the human FTN-H structure plus a third Fe^{3+} site bound by ligands unique to the *E. coli* sequence.[18] The crystal structure of the heme-containing bacterioferritin (BFN) from *E. coli* at 2.9 Å resolution also reveals two metal ions (presumably Fe) at the dinucelar location. The ligand set to the dinuclear metal clusters in human FTN-H, *E. coli* FTN-H, and in *E. coli* BFN are very similar to the ligands to the diiron centers of ribonucleotide reductase, methane monooxygenase, and fatty acid desaturase,[21] suggesting that the metal sites of FTN-H may act as the redox center of the protein. Furthermore, the entire diiron domain of rubrerythrin (4-helix bundle and B-C loop) can be superimposed on the structures of human FTN-H and BFN, and 4 of the 8 totally conserved residues are iron ligands in rubrerythrin.[22] No such metal binding sites are observed in crystals of frog L-chain ferritin,[20] possibly correlating with its lack of ferroxidase activity (see below).

Ferrozine inhibition studies by Harrison and coworkers have shown that the rate of Fe^{2+} uptake by FTN-H homopolymers is much faster than FTN-L homopolymers or wild-type HoSF (85% L-chain),[23-25] implying that H-chain subunits sequester iron at a much faster rate than L-chains. It is believed that the slow mineralization in L-chains involves direct diffusion of Fe^{2+} through the protein shell where it is oxidized by O_2. The faster

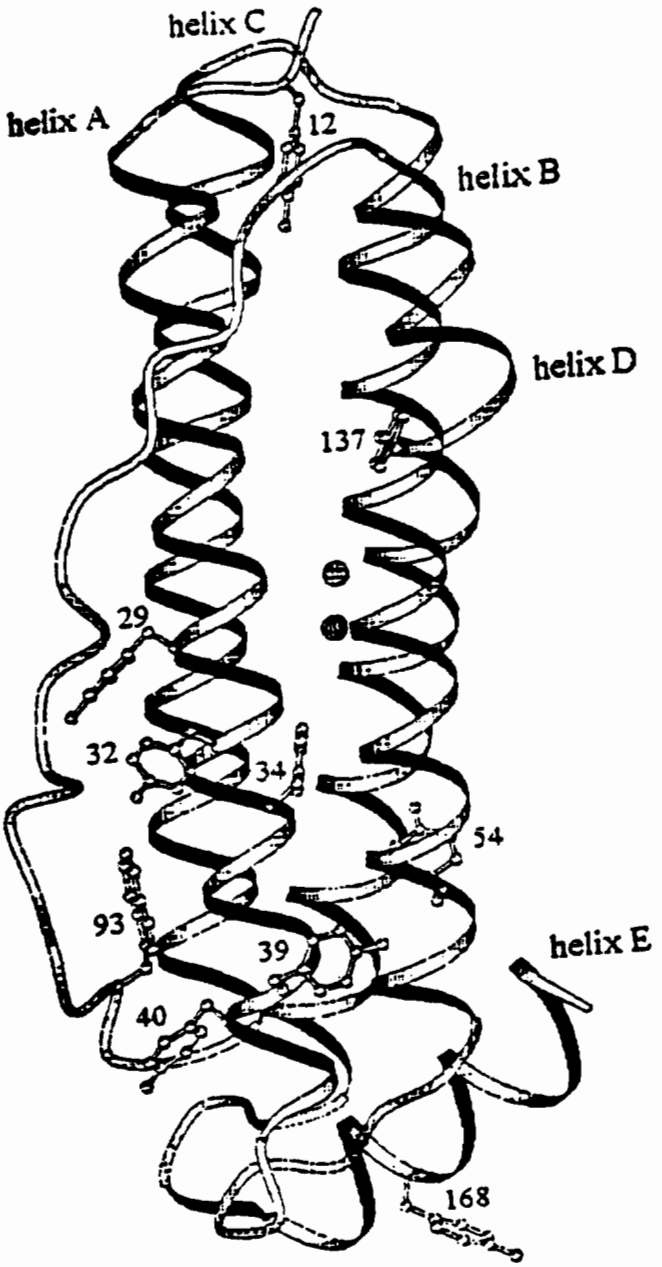

Figure 5-2. Schematic diagram of the human FTN-H subunit secondary structure taken from the crystal structure showing the side chains of the tyrosine residues and the location of the Tb^{3+} binding sites (probable diiron center). Adapted from reference 26. Tyrosines corresponding to positions 29, 32, 34, 40, 137, and 168 in human FTN-H are found at positions 25, 28, 30, 36, 133, and 164 in frog FTN-H.

mineralization of H-chains is believed to be due to catalysis of the O_2-dependent conversion of Fe^{2+} to Fe^{3+} (ferroxidation) at a site in the protein shell, followed by movement of Fe^{3+} into the core. It is possible that the dinuclear iron site in H-chains serves as the ferroxidase center, particularly by analogy to rubrerythrin which catalyzes ferroxidation at a similar rate.[22] Ferroxidase activity has typically been measured by O_2 consumption or by the appearance of absorbance at 420 nm, associated with formation of ferrihydrite in the core.[5,6,23]

More recently, new spectroscopic markers have been discovered which correspond to a ferroxidation intermediate in frog FTN-H homopolymers.[10] Theil and coworkers have shown that when concentrated samples of frog apoFTN-H are mixed anaerobically with 1 Fe^{2+} per subunit in buffer, followed by exposure to air, a transient visible absorbance (λ_{max} = 550 nm) is observed (Fig. 5-3). Raman spectra excited within the 550-nm absorption reveal features at 589, 1167, 1288, 1300, 1502, and 1602 cm^{-1}, characteristic of tyrosine-coordinated iron.[10] After 5 minutes at room temperature, this species begins to decay, replaced by an amber colored product (λ_{max} = 420 nm) characterized by Mössbauer and EPR spectroscopy as a polynuclear iron center,[24] presumably the initiator of core formation. The same experiment performed on frog apoFTN-L homopolymers proceeded directly to the amber colored intermediate without rapid development and decay of the transient [Fe-Tyr] species.

A somewhat different behavior has been observed with human FTN-H. Addition of 2 Fe^{2+}/subunit to human FTN-H homopolymers in the presence of excess O_2 results in the formation of a transient intermediate that absorbs at 650 nm instead of 550 nm.[26] Its rate of formation and decay is about 30-fold faster than the [Fe-Tyr] species in frog FTN-H. Incubation of Fe^{2+} with the Y34F mutant of human FTN-H (analogous to Y30F in frog FTN-H) yielded no detectable absorbance at 580 nm and at an Fe^{2+} uptake rate only ~50% as fast as wild-type.[24,26] Tyrosine 34 is very close to the metal centers observed in the crystal structure of human FTN-H and may serve as a transient binding site for Fe during rapid Fe uptake. Although a visible absorbance of 650 nm is somewhat lower in energy than expected for an (Tyr)O→Fe^{3+} LMCT band, these results imply that Tyr34 is critical for rapid Fe uptake by human FTN-H.

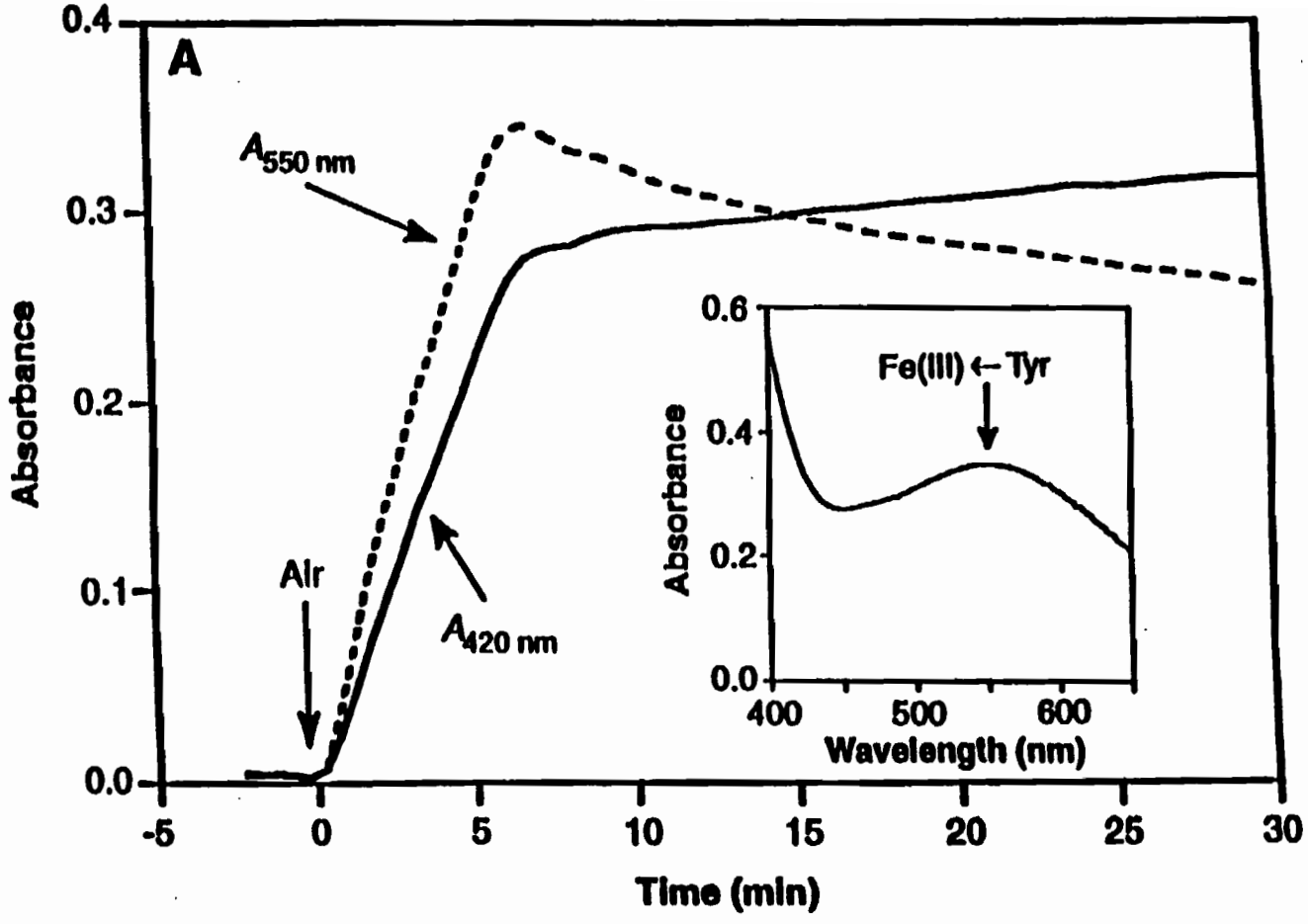

Figure 5-3. Kinetics of color formation for frog FTN-H homopolymers with one Fe atom per subunit. Inset: Electronic spectrum of the [Fe-Tyr] intermediate. Adapted from reference 10.

In order to identify the Tyr residues involved in rapid Fe^{2+} uptake by frog ferritins, several wild-type and mutant frog FTN-H homopolymers were prepared as concentrated apoprotein solutions. In each sample, one of three tyrosine residues (Tyr25, Tyr28, or Tyr30) was replaced by a phenylalanine by site directed mutagenesis. These tyrosine residues are in nearly the same position in the primary sequence as Tyr28, 32, and 34 of human FTN-H and are assumed to be close to the analogous Fe-binding sites on frog FTN-H. Preparation of each of these wild-type and mutant FTN-H samples resulted in a second spontaneous mutation, resulting in the substitution of leucine 134 for a proline residue (L134P) whose effects will be discussed later (see Discussion section). Resonance Raman spectroscopy was used to determine if the mutant frog FTN-H homopolymers were capable of forming the same [Fe-Tyr] intermediate observed with wild-type FTN-H homopolymers when mixed with Fe^{2+} in solution. The purpose of these experiments was to determine if one of these tyrosine mutations would "knock-out" [Fe-Tyr] formation. In addition, experiments were performed to measure the rate of [Fe-Tyr] decay in the RR spectrum of wild-type and mutant FTN-H, -M, and -L samples and compare these results to the decay rate obtained by time-resolved electronic absorption spectroscopy at 550 or 650 nm to determine if the two methods are observing the same species and how specific Tyr mutations affect the decay rates.

Our results strongly imply that rapid [Fe-Tyr] formation and Fe^{2+} uptake requires a specific Tyr residue in frog FTN-H that is not in the same vicinity as Tyr34 in the primary sequence. However, the close similarity between the kinetics and spectroscopy of frog FTN-M and human FTN-H suggests that these two ferritins form the same initial iron-tyrosinate intermediate, probably using Tyr34.

Experimental

Protein purification. The genes for bullfrog (*Rana catesbeiana*) wild-type (WT) and mutant FTN-H, -M, and -L homopolymers were cloned and overexpressed in *E. coli* using previously published methods.[10] Mature cells rich in FTN were sonicated at 70 °C

for 15 minutes and centrifuged. Ferritin was extracted from the supernatant by precipitation in 80% $(NH_4)_2SO_4$, followed by anion-exchange chromatography on a Mono Q column (Pharmacia). The average yield of FTN was 30 mg per 3g of cell pellet (1 liter of cell culture). The integrity of the 24-subunit homopolymers was verified by gel chromatography. Protein concentration was measured spectrophotometrically by the Bradford Assay.[27]

Preparation of Pre-mixed Samples. Samples of wild-type and mutant apoFTN-H pre-mixed with Fe^{2+} were prepared by Dana Danger and Prof. Elizabeth Theil at NCSU in 0.1 M bistris-propane + 0.25 M NaCl buffer (pH 7.5). Protein concentration was estimated to be 60 mg/ml (3 mM as subunits). The 550-nm intermediate was formed by adding 3 mM $FeSO_4$ to an anaerobic solution of apoprotein in buffer purged for 1 hour with argon. Subsequently, samples were exposed to air for 5 minutes, aliquots were transferred to glass capillary tubes, flame sealed, and stored at dry ice temperature. All samples arrived on dry ice and were analyzed immediately upon arrival.

Spectroscopy. Resonance Raman spectroscopy was performed on a custom-built McPherson 2061/207 Raman spectrograph equipped with an 1800-groove/mm holographic grating, a Princeton Instruments LN1100PB liquid N_2-cooled CCD detector, a Kaiser Optical Systems holographic super-notch filter, and interfaced to a Gateway 2000 personal computer. Laser excitation was provided by a Coherent Innova 90 Ar^+ ion laser operating at 514.5 nm or a Coherent Innova 302 Kr^+ laser operating at 647.1 nm. The incident laser power used was ~45 mW. Interfering plasma emissions were removed with an Applied Photophysics prism monochromator. Spectra were recorded using 90° scattering geometry with the samples at ~15 °C cooled in a copper cold finger placed in a dewar filled with cold water. The entrance slit of the spectrograph was set to 150 μm. All spectra were calibrated against indene or toluene as external standards for peak positions. Reported frequencies are estimated to be accurate to ±2 cm^{-1}. Spectra were smoothed and baseline-corrected using GRAMS/386 (Galactic Industries) software.

Electronic absorption spectra were recorded on a Perkin-Elmer Lambda-9 UV/Vis/NIR spectrophotometer interfaced to a Gateway 2000 personal computer.

Spectra were recorded in Kimax glass capillary tubes (1.5-1.8 mm path length) and were corrected against a background spectrum of water.

Protein Samples for Kinetic Measurements. Dilute samples of WT and mutant apoFTN-H and -L were prepared by Dana Danger at NCSU. Samples of WT apoFTN-M were prepared by Dr. John Fetter, also at NCSU. Unless otherwise stated, all kinetic experiments were performed in 0.1 M bistris-propane + 0.2 M NaCl (pH 7.5). Sample concentration was measured upon arrival by the Bradford Assay. Dilute apoprotein (2-4 mg/mL as 24mers) was concentrated using Centricon 30 (Amicon) microconcentrators in a refrigerated centrifuge and the protein concentration of the retentate was measured again. Kinetic measurements were performed by adding 25 μl of concentrated WT or mutant apoFTN (~2 mM as subunits) in buffer to a small glass vial fitted with a rubber septum and purged with oxygen for 10 minutes. After purging, the vial was opened and a 1 μl solution (1 Fe/subunit) of Fe^{2+} as $FeSO_4 \cdot 7H_2O$ in 10 mM HCl was added with rapid agitation by tapping the side of the vial (prior measurements revealed that the small addition of acid reduced the pH of the bistris-propane buffer solution by less than 0.05 units). The resulting mixture was transferred immediately to a capillary tube and examined spectrophotometrically.

Data Handling and Curve Fitting. The time-dependent absorption data at 550 nm was measured from 30 to 1200 s in 0.5-s time intervals using the Lambda-9 spectrophotometer. The first 30 s of data were not collected due to the time required for sample mixing and insertion into the spectrophotometer.

Resonance Raman data were collected in 30-s acquisition intervals for the first 400 s and in 200-s intervals thereafter for a total acquisition time of 1200 s. The first 5-10 s of data were not collected due to the time required for sample mixing and insertion into the sample holder. Sample mixing time for the RR experiments was much shorter because open capillary tubes could be filled by capillary action whereas the electronic absorption measurements required pipetting the Fe^{2+}-protein mixture into a closed-end capillary prior to insertion into the spectrophotometer.

I_{1600}/I_{1650} ratios were calculated by measuring quotient of the baseline-corrected RR peak height of the ν(C-C) mode at 1600 cm^{-1} with respect to the non-resonance-

enhanced Amide I protein band at 1650 cm^{-1}. The 1600-cm^{-1} peak was chosen for decay measurements because it is the sharpest of the iron-tyrosinate bands and usually displays the highest intensity relative to other resonance-enhanced modes.

Fits of the decay plots to first-order exponential functions were performed using the Levenberg-Marquardt nonlinear least squares fitting algorithm in the Origin v.3.5 (MicroCal) software package. Half lives of the decay rate were calculated from the time constants extrapolated from the slope of the decay curves.

Results

Identification of the [Fe-Tyr] Intermediate.

RR Spectrum of Wild-type FTN-H. The RR spectrum of frog WT FTN-H pre-mixed with Fe^{2+} and exposed to air reveals 5 features that can be assigned to resonance-enhanced iron-tyrosinate vibrations; two ν(C-O) stretching modes at 1287 and 1300 cm^{-1}, two ν(C-C) modes at 1501 and 1600 cm^{-1}, and a δ(C-H) bending mode at 1169 cm^{-1} (Fig. 5-4). Each of these peaks is within 3 cm^{-1} of the corresponding peaks in the spectrum of frog WT FTN-H previously reported by Theil and coworkers.[10] These assignments are based on the strong similarity between the RR spectra of FTN and model compounds of known structure containing iron-phenolate groups.[28, 40]

The pattern of bands in the RR spectrum of WT FTN-H is also very similar to the pattern observed in the spectra of other iron-tyrosinate proteins (Table 5-2). For example, the RR spectrum of catechol 1,2-dioxygenase (CTD) reveals 4 bands assigned to [Fe-Tyr] vibrations; two ν(C-C) ring stretching modes at 1604 and 1506 cm^{-1}, a broad ν(C-O) mode at 1289 cm^{-1}, and a δ(C-H) bending mode at 1175 cm^{-1}.[29] Similar iron-tyrosinate vibrations are observed in bacterial protocatechuate 3,4-dioxygenase (PCD),[30] and bovine purple acid phosphatase (PAP).[31] However, the RR spectrum of FTN-H is somewhat unusual in that the ν(C-O) stretching region contains two distinct peaks at 1287 and 1300 cm^{-1}. Similar splittings have been observed for the 4-hydroxybenzoate complex of protocatechuate 3,4-dioxygenase (PCD) and the benzoate complex of catechol 1,2-dioxygenase (CTD) (Table 5-2).

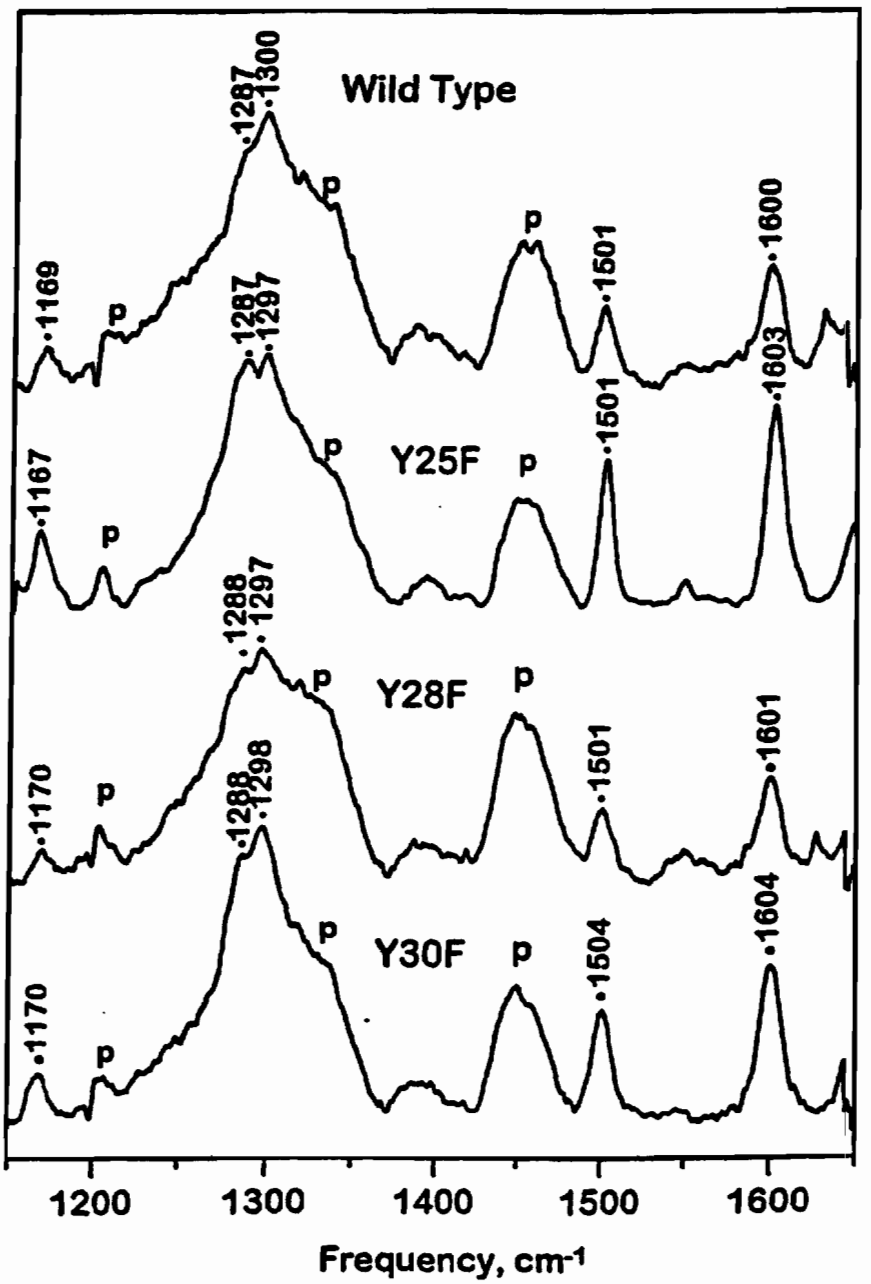

Figure 5-4. RR spectra of wild-type and mutant FTN-H homopolymers prepared by anaerobic addition of $FeSO_4$, followed by 5 min exposure to air. Raman spectra of samples (~ 2.5 mM as subunits) at ~290 K were obtained using 514.5-nm excitation (50 mW), 4.5 min exposure time. All spectra were 13-point smoothed and baseline corrected. Non-resonance-enhanced protein bands are denoted by **p**.

Table 5-2: Frequencies (cm^{-1}) of specific Fe-tyrosinate vibrations in the RR spectra of wild-type and mutant recombinant H-subunit ferritins and other iron-tyrosinate proteins.

Protein complex	δ(C-H)	ν(C-O)	ν(C-C)	ν(C-C)
WT FTN-H[a]	1169	1287/1300	1501	1600
Y25F FTN-H[a]	1167	1287/1297	1501	1603
Y28F FTN-H[a]	1170	1288/1297	1501	1601
Y30F FTN-H[a]	1170	1288/1297	1504	1604
CTD[b]	1175	1289	1506	1604
CTD + benzoate	1175	1258/1297	1506	1604
PCD[c]	1176	1254/1266	1505	1605
PCD + 4HB[d]	1174	1256/1288	1505	1606
PAP[e]	1164	1281	1497	1597

[a]This work. [b]Catechol 1,2-dioxygenase, reference 29. [c]Protocatechuate 3,4-dioxygenase, reference 30. [d]4-hydroxybenzoate, ν(C-O) at 1276 cm^{-1}. [e]Purple acid phosphatase, reference 31.

RR Spectra of Y25F, Y28F, and Y30F mutants of FTN-H. In these samples, one of the 3 tyrosine residues clustered on helix A was mutated to phenylalanine to see if these mutants were capable of generating the same [Fe-Tyr] intermediate. Each of these mutants pre-mixed with Fe^{2+} and exposed to air generated a very similar RR spectrum (Fig. 5-4) with two ν(C-O) vibrations at ~1288 and ~1297 cm^{-1}, two ν(C-C) modes at ~1502 and ~1602 cm^{-1} and a δ(C-H) mode at ~1170 cm^{-1} (Table 5-2). The spectra of these mutants reproduce the resonance-enhanced features found in the spectrum of wild-type FTN-H within 4 cm^{-1}, demonstrating that *neither Tyr25, Tyr28, nor Tyr30 are required for the formation of the [Fe-Tyr] intermediate in FTN-H.* These three tyrosines are highly conserved in most FTN-H chains and also in frog FTN-M, most of which do not form the 550-nm intermediate. This evidence strongly suggests that a different tyrosine residue is responsible for [Fe-Tyr] formation. Furthermore, the retention of the unusual ν(C-O) splitting pattern suggests that this [Fe-Tyr] intermediate is structurally unperturbed by the mutation of residue 25, 28, or 30.

Rate of Decay of the [Fe-Tyr] Intermediate.

Wild-type FTN-H. Concentrated samples of wild-type apoFTN-H (~2.5 mM as subunits) were saturated with O_2, then mixed with Fe^{2+} (1 Fe/subunit). Under these conditions, the formation of the [Fe-Tyr] intermediate as judged by absorbance at 550 nm is complete within 5 s. Although the formation reaction is too rapid for us to monitor due to the time required to mix the samples and place them in the spectrometer, we were able to follow the rapid phase of decay of the [Fe-Tyr] intermediate from the loss of its absorbance as well as its RR signal. The two types of measurements were performed using similar concentrated samples (~2.5 mM as subunits) in order to be able to directly compare the results from the two techniques. The plot of A_{550} versus time was fit to a single first-order exponential decay curve (Fig. 5-5). Despite the noise in the spectrum, the raw data fit very closely to the theoretical curve ($\chi^2 = 1.7\times10^{-5}$), demonstrating that [Fe-Tyr] decay displays first-order kinetics. After approximately 3 half lives, the A_{550} signal enters a slower phase of decay which does not return to baseline for several hours.

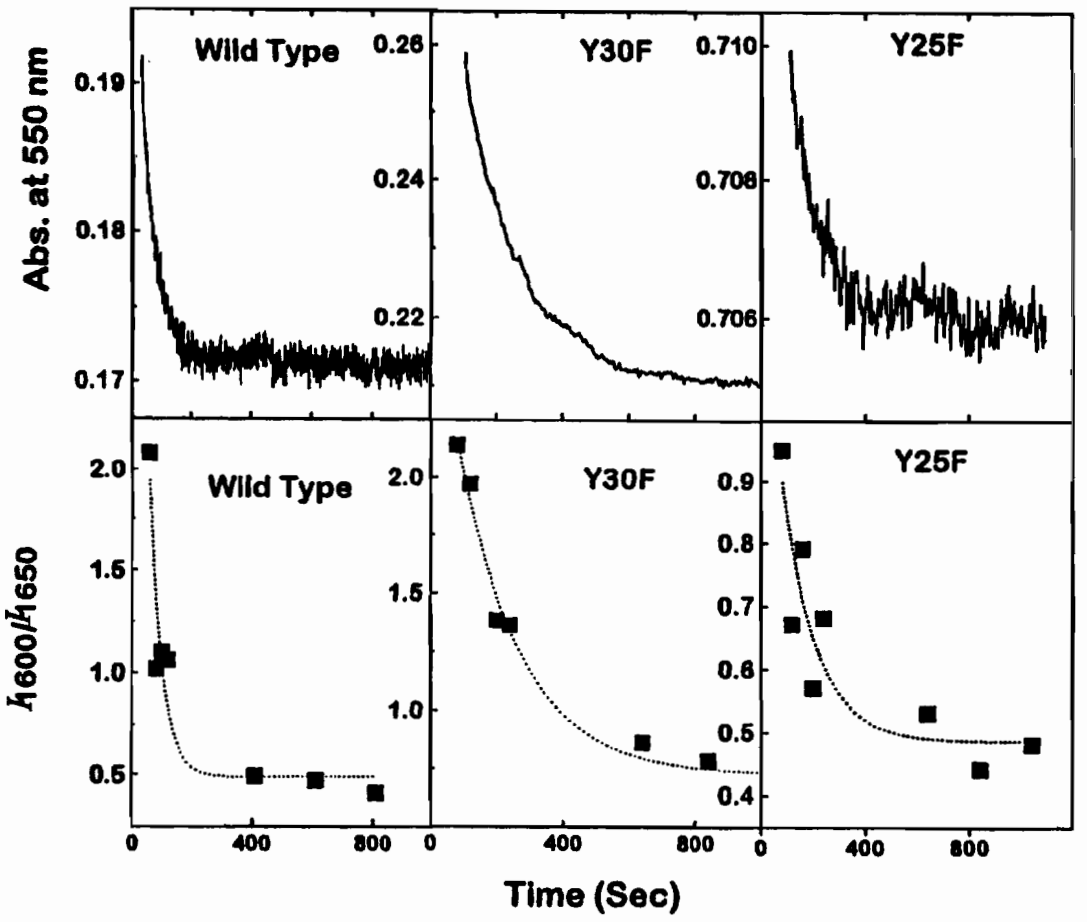

Figure 5-5. Kinetics of the decay of [Fe-Tyr] intermediate in wild-type and mutant FTN-H. Samples (~2.5 mM as subunits) were saturated with O_2 prior to mixing with 1 Fe^{2+}/subunit in 0.1 M bistris-propane + 0.2 M NaCl (pH 7.5). Decay was measured within 30 s of mixing by the loss of absorbance at 550 nm or the loss of Raman intensity at 1600 cm^{-1} relative to the protein band at 1650 cm^{-1}. Fits of the curves to single first-order exponential decay curves are shown as dotted lines.

The calculated half-life of decay ($t_{1/2}$) during the rapid phase was 27 s. This value is within 1 s of the 28 s half-life extrapolated from the decay curve of A_{550} vs. time for wild-type FTN-H, previously published by Theil and coworkers, when concentrated apoprotein was saturated with O_2 and subsequently mixed with Fe^{2+} (1 Fe/subunit).[32] Clearly, pre-saturation with O_2 accelerates the rate of [Fe-Tyr] decay by more than an order of magnitude relative to the same experiment when FTN-H and Fe^{2+} are mixed anaerobically followed by exposure to air.[32] This suggests that both the formation and decay of [Fe-Tyr] are strongly O_2-dependent.

In a parallel set of experiments using the same apoprotein concentrate, samples of WT apoFTN-H were mixed with Fe^{2+} as described above and RR spectra were collected at regular time intervals. The intensity of the sharp [Fe-Tyr] mode at 1600 cm^{-1} was measured using the intensity of a non-resonance-enhanced protein mode at 1650 cm^{-1} as an internal standard. The plot of I_{1600}/I_{1650} versus time was fit to a first-order decay with a calculated half-life of 28 s (Fig.5-5). This experiment demonstrates that there is excellent correlation between the time-resolved electronic absorption and RR data (Table 5-3). Therefore, the absorbance at 550 nm (A_{550}) in the electronic spectrum and the [Fe^{3+}-Tyr] vibrations in the RR spectrum are likely due to the same analyte. The same RR spectrum was observed at the earliest and latest time points, indicating that only a single [Fe-Tyr] species is involved. Furthermore, although the method of O_2 addition (prior to or after addition of Fe^{2+}) has a significant effect on the rate of [Fe-Tyr] formation, the appearance of an identical RR spectrum shows that the same intermediate is produced in both cases.

Y25F, Y28F, and Y30F Mutants of FTN-H. Samples of concentrated apoY25F and apoY30F FTN-H were incubated with Fe^{2+} under the same conditions used for wild-type and the plots of A_{550} and I_{1600}/I_{1650} versus time were fit to first-order exponential decay curves. The RR spectra displayed strong fluorescent backgrounds that came close to saturating the CCD detector. Data points where sudden increases in I_{1600}/I_{1650} were observed or where the poor signal-to-noise ratios prevented accurate measurements of I_{1600}/I_{1650} were not included in the fit. Although, many fewer data points were collected than in the A_{550} vs. time plots, the calculated half lives of the two parallel data sets differ by less than 20% which can be considered to be within experimental error. The results of

Table 5-3: Decay of the [Fe-Tyr] Intermediate in WT and Mutant Ferritins.[a]

Sample	Buffer (pH)	$t_{1/2}$ (A_{550})	$t_{1/2}$ (I_{1600}/I_{1650})
WT FTN-H	0.1 M BTP (7.5)	27	28
Y25F FTN-H	0.1 M BTP (7.5)	74	90
Y30F FTN-H	0.1 M BTP (7.5)	117	129
H25Y FTN-L	0.1 M MOPS (7.0)	none	none
WT FTN-M	0.1 M MOPS (7.0)	none	none

[a]Calculated half-lives (in seconds) determined from the decrease in absorbance at 550 nm or RR intensity at 1600 cm-1. Data collected as in Figure 5. None means no absorbance at 550 nm and no RR modes due to [Fe-Tyr] vibrations. BTP= bistris-propane.

Table 5-4: Correlation of Tyrosine Composition in Frog FTN with Formation of the [Fe-Tyr] Intermediate.

	Tyrosine Residues[a]						[Fe-Tyr][b]	
Sample	25	28	30	36	133	147	A_{550}	A_{650}
FTN-H (P134)[c]	+	+	+	+	+	+	+	(-)
Y25F FTN-H (P134)	(-)	+	+	+	+	+	+	(-)
Y28F FTN-H (P134)	+	(-)	+	+	+	+	+	(-)
Y30F FTN-H (P134)	+	+	(-)	+	+	+	+	(-)
WT FTN-H (L134)	+	+	+	+	+	+	(-)	+
WT FTN-M (L134)	+	+	+	(-)	+	(-)	(-)	+
WT FTN-L (L134)	(-)	+	+	+	+	(-)	(-)	(-)
H25Y FTN-L (L134)	+	+	+	+	+	(-)	(-)	(-)

[a]Numbering scheme according to frog H-chain ferritin as in Table 1. [b]Observation of iron-tyrosinate intermediate, by absorbance at 550 or 650 nm. [c]Referred to as wild-type FTN-H in the Results section.

these calculations show an approximately 3-4-fold increase in the calculated half lives of [Fe-Tyr] decay for each of the mutants with respect to wild-type (Fig. 5-5, Table 5-3). Consequently, even though the Y25F and Y30F samples generated a nearly identical [Fe-Tyr] species to wild-type (Fig. 5-4), its rate of decay was decreased by these mutations.

Although the Raman spectrum of Y28F identifies the same [Fe-Tyr] intermediate (Fig. 5-4) we were unable to obtain good enough data for kinetic analysis. Theses samples had a high fluorescence background and a poor signal-to-noise ratio, making it impossible to calculate accurate ratios of I_{1600}/I_{1650}. The calculated half lives obtained from A_{550} vs. time for three separate trials were 85, 150 and 39 s. This variance, which is probably due to the greater viscosity of this sample and poorer mixing, is too large to be considered reliable (although the average half-life of 91 s is close to the values obtained for Y25F). Nevertheless, the fact that the half-life of [Fe-Tyr] decay on each of the trials increased relative to wild-type indicates that the Y28F mutation also hinders [Fe-Tyr] decay.

H25Y Mutant of FTN-L. Previous experiments by several groups have demonstrated that Fe uptake by FTN-L homopolymers is much slower than the rate for wild-type FTN-H homopolymers or HoSF. Examination of the amino acid sequence of frog FTN-L reveals that there is a histidine residue at position 25 that is normally occupied by a tyrosine in frog FTN-H.[7] Theil and coworkers theorized that mutation of this residue to a tyrosine (H25Y) might result in the proper formation of the [Fe-Tyr] intermediate because such a mutant would now have Tyr25, Tyr28 and Tyr30; three of the five tyrosine residues in WT frog FTN-H including the two (Tyr28 and Tyr30) that are totally conserved in all vertebrate ferritins (Tables 5-1 and 5-4).

The RR spectrum of concentrated apoH25Y FTN-L mixed with 1 Fe^{2+}/subunit and excess O_2 did not reveal any absorbance at 550 nm indicative of the presence of the [Fe-Tyr] intermediate in the electronic absorption spectrum. Furthermore, although Raman bands were observed at 1452 and 1646 cm^{-1} assigned to protein CH_2 and Amide I vibrations, respectively,[33] no resonance-enhanced peaks associated with iron-tyrosinate vibrations were observed in the RR spectra (data not shown). These results prove that the H25Y FTN-L mutant is incapable of forming the [Fe-Tyr] intermediate.

Wild-type FTN-M. In addition to H- and L-chain ferritins, a third FTN isoform has been isolated from frog cDNA clones, denoted FTN-M, with the same number of amino acids and displaying 84% homology with FTN-H.[7] The primary structure of FTN-M contains Tyr25, Tyr28, Tyr30, and Tyr133 but Tyr 36 and Tyr147 have been replaced by phenylalanine residues (Tables 5-1 and 5-4). Fetter and coworkers report that the reaction of apoFTN-M with Fe^{2+} results in the rapid formation and decay of a 650-nm intermediate within 0.3 s,[34] very similar to the transient 650-nm intermediate observed for human FTN-H.

Despite the rapid rate of decay of the 650-nm intermediate, it was hoped that there might be a some residual Fe-tyrosinate that could still be detected by RR spectroscopy. However, samples of apoFTN-M (1.71 mM as subunits) failed to reveal any iron-tyrosinate vibrations in RR spectra collected within 30 s of Fe^{2+} addition and using either 647.1- or 514.5-nm excitation (data not shown). As a result, one cannot confirm the presence of an iron-tyrosinate species in this sample by RR spectroscopy alone. However, the strong similarity in spectroscopic and kinetic behavior of this ferritin with human FTN-H strongly implies that the transient 650-nm absorbance is very similar to that observed for WT human FTN-H homopolymers. The loss of this absorbance in the Y34F mutant of human FTN-H (analogous to Tyr30 in frog FTN-M) suggests that the 650-nm intermediate involves the tyrosine at position 34.

Discussion

Number of Fe-coordinated Tyrosines.

The appearance of two ν(C-O) peaks in the RR spectra of iron-tyrosinate proteins has previously been ascribed to the contribution of two iron-tyrosinate species.[30] In the case of PCD, the X-ray crystal structure revealed the presence of two tyrosinate ligands in axial and equatorial positions bound to a 5-coordinate high spin Fe^{3+}.[35] These have been associated with ν(C-O) modes at 1266 and 1254 cm^{-1}, respectively.[30] Furthermore, only the peak at 1266 cm^{-1} underwent a frequency shift of +6 cm^{-1} in D_2O, indicative of H-bonding of a single tyrosinate ligand. Addition of 4-hydroxybenzoate caused a large shift

in one of the ν(C-O) vibrations, yielding features at 1256 and 1289 cm^{-1} (Table 5-2).[30] These results were interpreted as evidence for the continued presence of two tyrosinate ligands coordinated to the active site iron.[36] Recent crystallographic studies confirm that monohydroxy inhibitors such as 4-hydroxybenzoate bind to PCD in the equatorial plane of the Fe^{3+} cluster but do not displace either of the tyrosinate ligands.[37] A similar mechanism may be operating in CTD which reveals a pair of bands at 1258 and 1297 cm^{-1} upon addition of benzoate (Table 5-2).

The two ν(C-O) peaks in the spectra of PCD-inhibitor adducts show different resonance enhancement profiles. While the intensity of the 1288-cm^{-1} peak is fairly constant using excitation wavelengths between 458 and 588 nm, the intensity of the 1256-cm^{-1} peak shows a steep decrease as the excitation wavelength is increased over the same interval.[30] In contrast, the intensities of the two ν(C-O) peaks in the spectrum of WT FTN-H remain approximately equal regardless of the excitation wavelength used.[38] Consequently, it is likely that the splitting of the ν(C-O) modes in the spectrum of frog FTN-H is due to a single Fe-tyrosinate.

The question arises as to how a single tyrosinate ligand can give rise to two Fe-tyrosinate modes. One possibility is the existence of multiple protein conformations. However, a more likely explanation is Fermi resonance, whereby a single ν(C-O) mode couples with another tyrosine ring vibration of the same energy to produce a doublet of peaks at higher and lower energy. Tyrosine has long been known to exhibit another Fermi doublet at 830 and 850 cm^{-1} and these peaks are observed in the Raman spectra of all tyrosine-containing proteins.[39] The appearance of a Fermi doublet in the ν(C-O) region is more variable, presumably because the ν(C-O) mode itself varies from 1265-1310 cm^{-1}, depending on the nature of the protein environment.[40] Thus, the occurrence of Fermi splitting would vary depending on the degree of overlap of vibrational frequencies in the 1270-1290 cm^{-1} region. The shift in vibrational frequency in D_2O appears to destroy this resonance, such that only a singel intense feature is observed at 1287 cm^{-1}.[41] Further support for a Fermi doublet assignment in FTN-H comes from the fact that the relative intensities of the two ν(C-O) modes are unaffected by varying the protein preparation, temperature, or reaction time.

Identification of [Fe-Tyr] Intermediates.

A_{650} Intermediate. Human FTN-H exhibits a 650-nm intermediate that is fully formed within 0.3 s and fully decayed within 5 s of O_2 addition.[26] A similar behavior is observed for frog FTN-M. Furthermore, Y34F mutants of human FTN-H demonstrate a 50% decrease in Fe uptake and no 650-nm absorbance, implying that this residue is associated with rapid Fe uptake in human FTN-H.[26] The requirement of Tyr34 for color formation implies that the 650-nm absorbance is a Tyr $\rightarrow Fe^{3+}$ CT band. The alternative proposal of peroxo $\rightarrow Fe^{3+}$ CT appears to be ruled out because a relatively high rate of O_2 consumption and peroxide formation persists in the Phe34 mutant, despite the disappearance of A_{650}. Although iron binding to Tyr34 appears to be part of the rapid iron uptake pathway, the ferroxidase reaction can continue without it. The corresponding residue in frog FTN-M and frog FTN-H is Tyr30 (Table 5-1). The Y30F mutation in frog FTN-H causes a similar decrease in ferroxidase activity, implying that this tyrosine plays a similar role in the rapid iron uptake pathway.[34]

Neither WT nor H25Y FTN-L are capable of forming the 650-nm [Fe-Tyr] intermediate, despite the presence of Tyr30 (Table 5-4). This suggests that the absence of an [Fe-Tyr] intermediate in FTN-L is not due to the absence of a particular tyrosine residue. Rather, the absence of the [Fe-Tyr] intermediate is probably due to the lack of a diiron binding site in L-chain ferritins which is required for ferroxidase activity.

A Redefinition of Frog FTN-H. In each mutant FTN-H sample, one of three tyrosine residues (Tyr25, Tyr28, or Tyr30) was replaced by a phenylalanine by site directed mutagenesis. These tyrosine residues are in nearly the same position in the primary sequence as Tyr28, 32, and 34 of human FTN-H and are assumed to be close to the analogous Fe-binding sites on frog FTN-H. The frog FTN-H used in these studies was prepared from a frog gene expressed in *E. coli*. Subsequent DNA sequencing has revealed a spontaneous mutation of the totally conserved leucine at position 134 to a proline. [34] All of the samples of frog FTN-H (WT as well as Y25F, Y28F, and Y30F) described in the results section actually harbored this L134P substitution. A true WT FTN-H has now been generated by converting Pro134 back to Leu.[34] This frog FTN-H now forms a 650-

nm intermediate similar to human FTN-H and frog FTN-M, presumably due to an [Fe-Tyr] at Tyr30 (Table 5-4). Surprisingly, the 550-nm intermediate is no longer formed in true WT frog FTN-H.

A_{550} Intermediate. The above studies suggest that the absorbance at 550 nm only appears in FTN-H that has the L134P mutation. It is likely that the Pro134 alteration of the D-helix activates a nearby tyrosine for Fe binding. The most probable candidates are Tyr133 and Tyr147 which are both on the D-helix and are located on either side of the proposed diiron site (Fig. 5-2). The 550-nm intermediate in frog FTN-H (L134P), previously referred to as wild-type, displays biphasic kinetics in its formation as well as its decay.[32] Although the two-phase behavior could signify the participation of two different [Fe-Tyr] intermediates, the identical RR spectra obtained during the fast (30-100s) and slow (>500 s) phases of the decay are indicative of a single [Fe-Tyr] intermediate. The Y25F, Y28F, and Y30F mutants of frog FTN-H used in these studies also contain the L134P mutation. Their RR spectra show that they have formed the same [Fe-Tyr] intermediate, presumably located on the D-helix. While the structure of the 550-nm intermediate is unaffected by the removal of tyrosine 25, 28, or 30, the rates of formation and decay of this intermediate are significantly decreased. Thus, the association of Fe^{3+} with D-helix tyrosines is definitely influenced by the overall ferroxidase activity of the frog FTN-H. However, the rate of iron uptake and core formation is the same in FTN-H (L134P), which has a 550-nm intermediate, and true WT FTN-H which lacks it. This suggests that the 550-nm [Fe-Tyr] intermediate is not a significant contributor to iron oxidation. Nevertheless, this intermediate serves as a detectable marker for the ferroxidase reaction and proves that the reaction occurs within the four-α-helix bundle rather than solely on the growing core surface.

Relationship of [Fe-Tyr] Intermediates to the Diiron Site.

The X-ray crystal structures of human and *E. coli* FTN-H subunits reveal that both bacterial and vertebrate H-chain ferritins possess dinuclear metal clusters within the 4-α-helix bundle.[18,19] These dinuclear clusters may serve as the redox centers for conversion of Fe^{2+} to Fe^{3+} during ferroxidation, similar to the behavior of such sites in other diiron

proteins.[21] The overall stoichiometry of the ferroxidase reaction at low iron levels can be written as:[15]

$$2Fe^{2+} + O_2 + 4H_2O \longrightarrow 2FeOOH_{core} + H_2O_2 + 4H^+$$

A proposed electron-transfer mechanism for this reaction is shown in Figure 6. By analogy to the diiron-oxo enzymes such as methane monooxygenase[21] and rubrerythrin,[22] FTN-H would bind two Fe^{2+} as a hydroxo-bridged cluster which could then reduce O_2 to peroxide. The peroxide would be released at this stage generating an oxo-bridged diferric site. The diiron site would then oxidize the Fe^{2+} substrate and become reduced by one electron, forming a mixed-valence intermediate. Mixed-valence Fe^{2+}/Fe^{3+} intermediates have been detected in HoSF.[42]

The role of the [Fe-Tyr] intermediate may be to bring the sequestered Fe^{2+} in close proximity to the proposed ferroxidase site so that efficient and rapid electron transfer can take place. This theory is supported by the *E. coli* and human crystal structures revealing a third metal binding site very near the proposed diiron sites.[18] This third site may be using Tyr30 as a ligand in frog FTN-H and FTN-M (Tyr34 in human FTN-H). The next Fe^{2+} substrate could bind to a nearby site (X in Fig. 5-6) and also become oxidized by donating an electron to the diiron site. The close proximity of Tyr30 could facilitate the formation of polymerized hydrated Fe^{3+} clusters that then move into the core. This would explain the observation of the 650-nm intermediate associated with Tyr30. The 550-nm [Fe-Tyr] intermediate is more likely associated with a tyrosine on the D-helix of FTN-H (L134P) such as Tyr133 or Tyr147. The longer lifetime of this intermediate could be due to Fe^{3+} remaining bound at this site instead of undergoing polymerization.

The strong conservation of the secondary structures of human and *E. coli* FTN-H has already been demonstrated.[4] Assuming that the secondary structure near the proposed ferroxidase sites on human and frog FTN-H are very similar, Tyr133 would be positioned on helix D, oriented with its side chain approximately toward helix B in an opposite

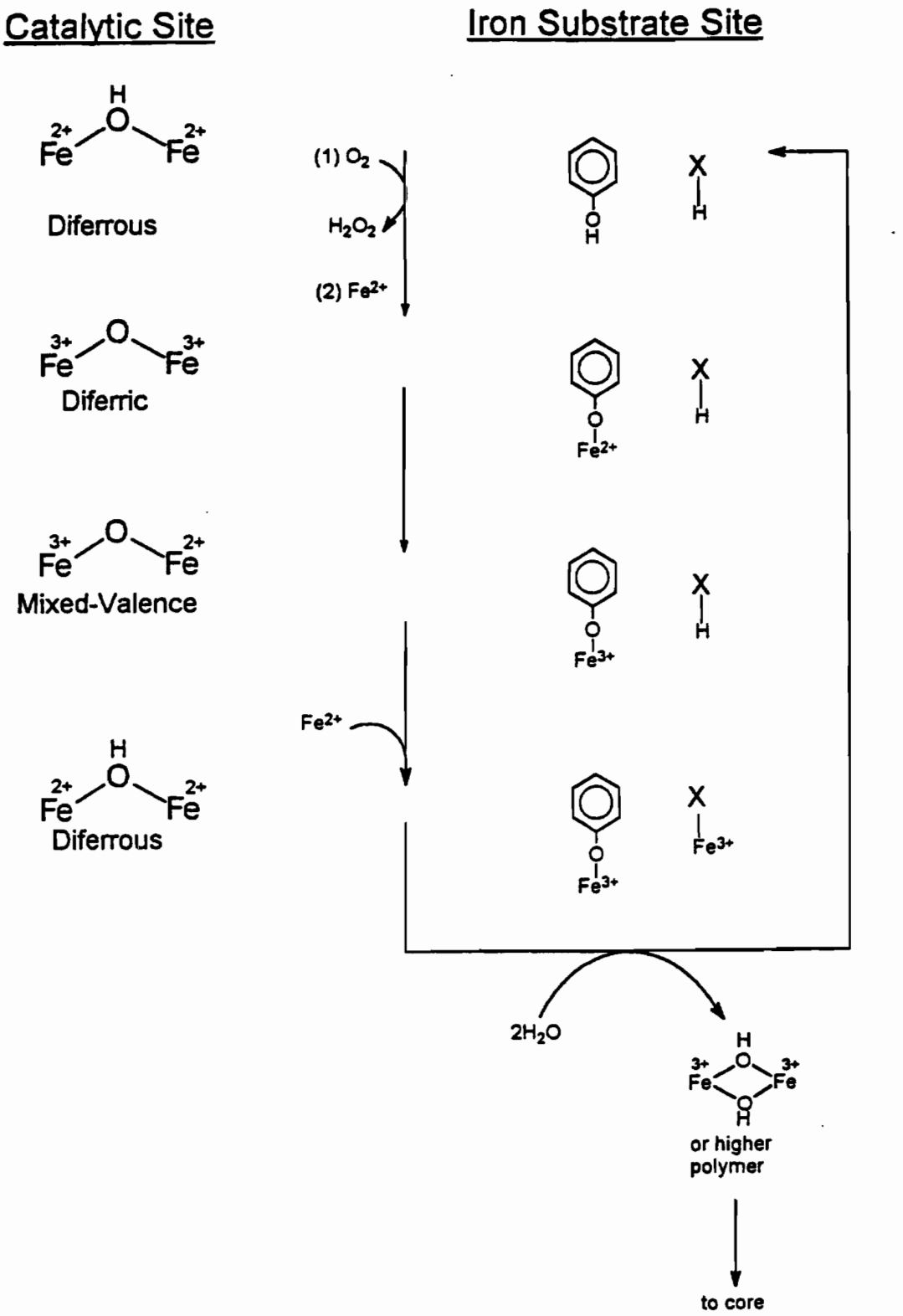

Figure 5-6. Proposed electron-transfer mechanism for the ferroxidase reaction of FTN-H.

position to Tyr30 through an imaginary center of symmetry in the 4-α-helix bundle (Fig. 5-2). Using the human FTN-H secondary structure for comparison, the phenolate oxygen atom of Tyr137 (analogous to Tyr133) is ~7.1 Å from Fe_a and ~3.3 Å from Fe_b of the proposed ferroxidase site in FTN-H (compared to the respective distances of ~7.5 Å and ~3.7 Å for Tyr34). In the x-ray structure of frog FTN-L, Tyr133 is oriented with its side chain approximately perpendicular to the 4-α-helical axis toward helix B, very similar to the position and orientation observed in human FTN-H.[20]

An alternative ferroxidase mechanism is shown in Figure 5-7. This mechanism involves a similar formation of a diferrous site which reduces O_2 to H_2O_2. It differs from the previous mechanism in that the resultant diferric product is itself labile and diffuses into the core. In this case the reaction would be autocatalytic with the diiron site serving as its own substrate. This is different from the previous mechanism (Fig. 5-6) which invoked a stable diiron site catalyzing electron transfer from more mobile iron substrate species. In the autocatalytic mechanism the observed [Fe-Tyr] intermediates could be ligands to the dinuclear site, as shown in Figure 5-7, or they could be separate conduits for diffusion of ferric products to the core. Although the electron transfer mechanism agrees better with the known function of diiron sites in other enzymes, the autocatalytic mechanism agrees better with the observed saturation of 2.1 Fe per FTN-H subunit.[32]

Role of FTN Isoforms in Fe Homeostasis.

Phylogenetic evidence suggests that H-chain ferritins can be considered the progenitor of L-chain ferritins.[43] As organisms evolved specialized iron storage tissues, the need for rapid ferroxidation was offset by the additional need for a stable Fe reservoir supplied by FTN-L. Ferritins composed predominantly of L-chains are found in high concentrations within tissues, such as the liver, where the primary role of ferritin is long-term iron storage. Ferritins rich in the H-chain isoform are found predominantly in tissues where $[O_2]$ is high, such as in the heart and muscles, where reactions of free Fe^{2+} with O_2 could produce reactive oxygen species such as $O_2^{\cdot-}$ and $OH^{\cdot}$ implicated in lipid peroxidation and other free-radical reactions.[3]

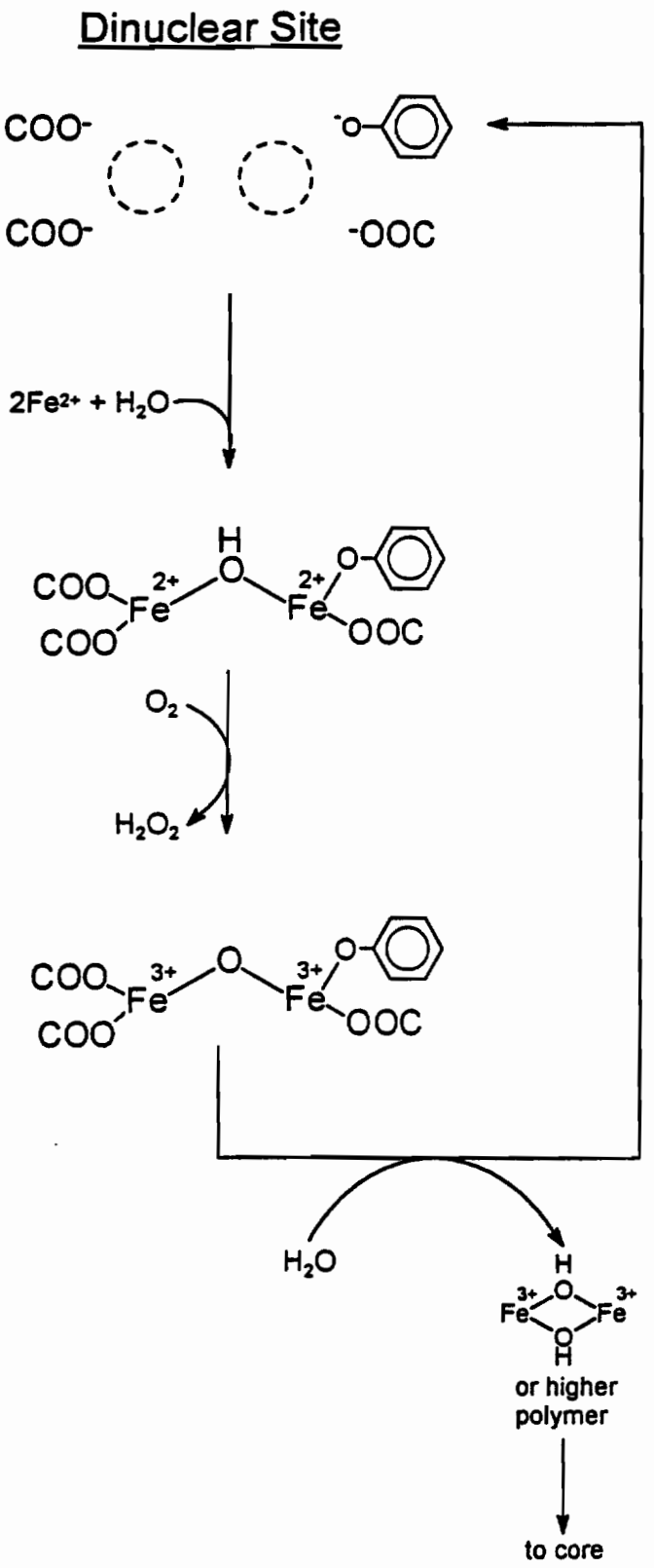

Figure 5-7. Proposed autocatalytic mechanism for the ferroxidase reaction of FTN-H.

Suggested directions for future studies.

Future work on frog ferritins should include the characterization additional mutants. A Y133F or Y147F mutation in FTN-H is expected to remove the 550-nm [Fe-Tyr] signal without causing a significant reduction in Fe uptake rates. A Y30F mutation in FTN-H or FTN-M is expected to result in a loss of the 650-nm absorbance and a large reduction (at least 2-fold) in Fe-uptake rates. This would constitute additional evidence that Tyr30 is an important Fe binding site in frog FTN-M homopolymers. Efforts are already underway to isolate, purify and characterize a frog Y(25,28,30)F FTN-M triple mutant. If this mutant displays similar RR spectrum to the spectrum of WT FTN-H shown in Figure 5-4, then this would certainly eliminate these residues as initial Fe binding sites (and also disprove the hypothesis that when one tyrosine residue in this cluster is eliminated by site-directed mutagenesis, a nearby tyrosine residue "volunteers" as a replacement ligand). However, given the strong similarities between the RR spectra of WT and mutant FTN-H displayed in this work, a Y133F or Y147F mutant would be more conclusive.

References and Notes

(1) This work was performed in collaboration with Dana Danger, D. J. F., and Prof. Elizabeth Theil in the Department of Chemistry, North Carolina State University, Raleigh, NC.

(2) Mason, S. F. *Chemical Evolution*; Clarendon Press, Oxford: Oxford, 1990.

(3) Halliwell, B.; Gutteridge, J. M. *Free Radicals in Biology and Medicine*; Clarendon Press: Oxford, 1984.

(4) Harrison, P. M.; Arosio, P. "The Ferritins: Molecular Properties, Iron Storage Function and Cellular Regulation." *Biochim. Biophys. Acta* **1996**, *1275*, 161-203.

(5) Waldo, G. S.; Theil, E. C. "Ferritin and Iron Biomineralization." *Comp. Supramol. Struct.* **1996**, *5*, 65-89.

(6) Harrison, P. M.; Lilley, T. H. "Ferritin;" in *Iron Carriers and Iron Proteins*; Loehr, T. M.; Ed.; VCH Publishers: N. Y., 1989, pp. 123-238.

(7) Dickey, L. F.; Sreedharan, S.; Theil, E. C.; Didsbury, J. R.; Wang, Y.-H.; Kaufman, R. E. "Differences in the Regulation of Messenger RNA for Housekeeping and Specialized-Cell Ferritin." *J. Biol. Chem.* **1987**, *262*, 7901-7907.

(8) Heusterspreute, M.; Chrichton, R. R. "Amino Acid Sequence of Horse Spleen Apoferritin." *FEBS Lett.* **1981**, *129*, 322-327.

(9) Levi, S.; Cesareni, G.; Arosio, P.; Lorenzetti, R.; Soria, M.; Sollazzo, M.; Albertini, A.; Cortese, R. "Characterization of Human Ferritin H Chain Synthetized in *E. coli*." *Gene* **1987**, *51*, 269-274.

(10) Waldo, G. S.; Ling, J.; Sanders-Loehr, J.; Theil, E. C. "Formation of an Fe(III)-Tyrosinate Complex During Biomineralization of H-Subunit Ferritin." *Science* **1993**, *259*, 796-798.

(11) Heald, S. M.; Stern, E. A.; Bunker, B.; Holt, E. M.; Holt, S. L. "Structure of the Iron-Containing Core in Ferritin by the Extended X-ray Absorption Fine Structure Technique." *J. Am. Chem. Soc.* **1979**, *101*, 67-73.

(12) Brady, G. W.; Kurkjian, C. R.; Lyden, E. F.; Robin, M. B.; Saltman, P.; Spiro, T. G.; Terzis, A. "The Structure of an Iron Core Analog of Ferritin." *Biochemistry* **1968**, *7*, 2185-2192.

(13) Gorun, S. M.; Papaefthymiou, G. C.; Frankel, R. B.; Lippard, S. J. "Synthesis, Structure, and Properties of an Undecairon(III) Oxo-Hydroxo Aggregate: An Approach to the Polyiron Core in Ferritin." *J. Am. Chem. Soc.* **1987**, *109*, 3337-3348.

(14) Taft, K. L.; Papaefthymiou, G. C.; Lippard, S. J. "A Mixed-Valent Polyiron Oxo Complex that Models the Biomineralization of the Ferritin Core." *Science* **1993**, *259*, 1302-1305.

(15) Xu, B.; Chasteen, D. "Iron Oxidation Chemistry in Ferritin." *J. Biol. Chem.* **1991**, *266*, 19965-19970.

(16) Lawson, D. M.; Artymiuk, P. J.; Yewdall, S. J.; Smith, J. M.; Livingstone, J. C.; Treffry, A.; Luzzago, A.; Levi, S.; Arosio, P.; Cesareni, G.; Thomas, C. D.; Shaw, W. V.; Harrison, P. M. "Solving the Structure of Human H Ferritin by Genetically Engineering Intermolecular Crystal Contacts." *Nature* **1991**, *349*, 541-544.

(17) Frolow, F.; Kalb (Gilboa), A. J.; Yariv, J. "Structure of a Unique Twofold Symmetric Haem-Binding Site." *Nat. Struct. Biol.* **1994**, *1*, 453-460.

(18) Hempstead, P. D.; Hudson, A. J.; Artymiuk, P. J.; Andrews, S. C.; Banfield, M. J.; Guest, J. R.; Harrison, P. M. "Direct Observation of the Iron Binding Sites of a Ferritin." *FEBS Lett.* **1994**, *350*, 258-262.

(19) Lawson, D. M.; Treffry, A.; Artymiuk, P. J.; Harrison, P. M.; Yewdall, S. J.; Luzzago, A.; Cesareni, G.; Levi, S.; Arosio, P. "Identification of the Ferroxidase Center in Ferritin." *FEBS Lett.* **1989**, *254*, 207-210.

(20) Trikha, J.; Theil, E. C.; Allewell, N. M. "High Resolution Crystal Structures of Amphibian Red Cell L Ferritin: Potential Roles for Structural Plasticity and Solvation in Function." *J. Mol. Biol.* **1995**, *248*, 949-967.

(21) Nordlund, P.; Eklund, H. "Di-Iron-Carboxylate Proteins." *Curr. Op. Struct. Biol.* **1995**, *5*, 758-766.

(22) deMare, F.; Kurtz Jr., D. M.; Nordlund, P. "The Structure of *Desulfovibrio vulgaris* Ruberythrin Reveals a Unique Combination of Rubredoxin-Like FeS_4 and Ferritin-Like Diiron Domains." *Nat. Struct. Biol.* **1996**, *3*, 539-546.

(23) Harrison, P. M.; Bauminger, E. R.; Hechel, D.; Hodson, N. W.; Nowik, I.; Treffry, A.; Yewdall, S. J. "Mechanism of Fe(II) Oxidation and Core Formation in Ferritin;" in *Progress in Iron Research*; Hershko, C.; Ed.; Clarendon Press: Oxford; 1994, pp. 1-12.

(24) Bauminger, E. R.; Harrison, P. M.; Hechel, D.; Hodson, N. W.; Nowik, I.; Treffry, A. "Iron (II) Oxidation and Early Intermediates of Iron-Core Formation in Recombinant Human H-chain Ferritin." *Biochem. J.* **1993**, *296*, 709-719.

(25) Treffry, A.; Bauminger, E. R.; Hechel, D.; Hodson, N. W.; Nowik, I.; Yewdall, S. J.; Harrison, P. M. "Defining the Roles of the Threefold Channels in Iron Uptake, Iron Oxidation and Iron-core Formation in Ferritin: A Study Aided by Site-directed Mutagenesis." *Biochem. J.* **1993**, *296*, 721-728.

(26) Treffry, A.; Zhao, Z.; Quail, M. A.; Guest, J. R.; Harrison, P. M. "Iron(II) Oxidation by H Chain Ferritin: Evidence from Site-Directed Mutagenesis That a Transient Blue Species is Formed at the Dinuclear Iron Center." *Biochemistry* **1995**, *34*, 15204-15213.

(27) Bollag, D. M.; Edelstein, S. J. *Protein Methods*; Wiley-Liss: New York, 1991.

(28) Gaber, B. P.; Miskowski, V.; Spiro, T. G. "Resonance Raman Scattering from Iron(III)- and Copper(II)-Transferrin and an Iron(III) Model Compound. A Spectroscopic Interpretation of the Transferrin Binding Site." *J. Am. Chem. Soc.* **1974**, *96*, 6868-6873.

(29) Que Jr., L.; Heistand II, R. H.; Mayer, R.; Roe, A. L. "Resonance Raman Studies of Pyrocatechase-Inhibitor Complexes." *Biochemistry* **1980**, *19*, 2588-2593.

(30) Siu, D. C.; Orville, A. M.; Lipscomb, J. D.; Ohlendorf, D. H.; Que Jr., L. "Resonance Raman Studies of the Protocatechuate 3,4-Dioxygenase from *Brevibacterium fuscum*." *Biochemistry* **1992**, *31*, 10443-10448.

(31) Averill, B. A.; Davis, J. C.; Burman, S.; Zirino, T.; Sanders-Loehr, J.; Loehr, T. M.; Sage, J. T.; Debrunner, P. G. "Spectroscopic and Magnetic Studies of the Purple Acid Phospahtase from Bovine Spleen." *J. Am. Chem. Soc.* **1987**, *109*, 3760-3767.

(32) Waldo, G. S.; Theil, E. C. "Formation of Iron (III)-Tyrosinate is the Fastest Reaction Observed in Ferritin." *Biochemistry* **1993**, *32*, 13262-13269.

(33) Carey, P. R. *Biochemical Applications of Raman and Resonance Raman Spectroscopies*; Academic Press: New York, 1982.

(34) Fetter, J. D.; Theil, E. C., *private communication*, North Carolina State University, Raleigh, NC.

(35) Ohlendorf, D. H.; Orville, A. M.; Lipscomb, J. D. "Structure of Protocatechuate 3,4-Dioxygenase from *Pseudomonas aeruginosa*." *J. Mol. Biol.* **1994**, *244*, 586-608.

(36) Que Jr., L.; Epstein, R. M. "Resonance Raman Studies on Protocatechuate 3,4-Dioxygenase-Inhibitor." *Biochemsitry* **1981**, *20*, 2545-2549.

(37) Ohlendorf, D. H.; Orville, A. M.; Elango, N.; Lipscomb, J. D., *unpublished results*, University of Minnesota, Minneapolis, MN.

(38) Ling, J.; Sanders-Loehr, J. "Resonance Raman Studies of Fe-Ferritin Intermediate. Evidence for Tyrosinate Coordination of Fe(III)." *unpublished results*, Oregon Graduate Institute of Science and Technology, Portland, OR.

(39) Siamwiza, M. N.; Lord, R. C.; Chen, M. C.; Takamatsu, T.; Harada, I.; Matsuura, H.; Shimanouchi, T. "Interpretation of the Doublet at 850 and 830 cm^{-1} in the Raman Spectra of Tyrosyl Residues in Proteins and Certain Model Compounds." *Biochemistry* **1975**, *14*, 4870-4876.

(40) Que Jr., L. "Metal-Tyrosinate Proteins;" in *Biological Applications of Resonance Raman Spectroscopy*; Spiro, T. G., Ed.; Wiley & Sons: New York, 1988; Vol. 3, pp. 491-521.

(41) Ling, J.; Sanders-Loehr, J. S. "Resonance Raman Studies of Fe-Ferritin Intermediate. Report II." *unpublished results*, Oregon Graduate Institute of Science and Technology, Portland, OR.

(42) Sun, S.; Chasteen, N. D. "Rapid Kinetics of the EPR-Active Species Formed During Initial Iron Uptake in Horse Spleen Apoferritin." *Biochemistry* **1994**, *33*, 15095-15102.

(43) Andrews, S. C.; Arosio, P.; Bottke, W.; Briat, J.-F.; von Darl, M.; Harrison, P. M.; Laulhere, J.-P.; Levi, S.; Lobreaux, S.; Yewdall, S. J. "Structure, Function, and Evolution of Ferritins." *J. Inorg. Biochem.* **1992**, *47*, 161-174.

Biographical Note

Jonathan D. Cohen was born in Los Angeles, California on Nov. 11, 1967. He attended Venice High School in Venice, California from 1983 to 1985 where he graduated with High Honors. He received his undergraduate education in the College of Letters and Sciences at the University of California at Santa Barbara where he received his B.A. in Chemistry in 1989 with an emphasis on Instrumental Analysis. After graduation, he worked for one year for E.G.&G. Special Technologies in Santa Barbara, California as a technician and two years for Coast to Coast Analytical Services in Goleta, California as a wet lab chemist. He began his graduate studies in the Department of Chemistry, Biochemistry, and Molecular Biology at the Oregon Graduate Institute of Science and Technology in Fall of 1991.